NESTED HIGH RESOLUTION SIMULATION AND LIDAR VALIDATION OF A LAND BREEZE CIRCULATION

by

GIJS DE BOER

A dissertation submitted in partial fulfillment of
the requirements for the degree of

MASTER OF SCIENCE
(ATMOSPHERIC AND OCEANIC SCIENCES)

at the

UNIVERSITY OF WISCONSIN – MADISON

2004

APPROVED

Date:

Gregory J. Tripoli
Professor, Atmospheric and Oceanic Sciences

Abstract

Explicit numerical simulation of the atmospheric boundary layer was, until recently, impossible due to constraints on attainable resolutions given the computing resources available. In this study, a dynamical downscaling technique is utilized in order to numerically simulate a micro-α scale land breeze circulation observed off of Sheboygan (WI) Point. It is argued that certain circulations can be replicated with accuracy due to the fact that they are a result of the interaction between the predictable large (meso-α and larger) scale and the well resolved local forcing. A wide range of scales is simulated using the nesting capability of the University of Wisconsin Non-Hydrostatic Modeling System.

The problem of validation is addressed through the use of lidar data taken with the University of Wisconsin Volume Imaging Lidar (UW-VIL) on the shores of Sheboygan, Wisconsin during the Lake Induced Convection Experiments (Lake-ICE) in the winter of 1997 and 1998. The lidar data presents a huge advantage in the model validation because it is able to capture four-dimensional (three spatial and time) representations of atmospheric motion at high temporal and spatial resolution, unlike more traditional methods which are point measurements taken at larger time intervals. This data can then be compared with the flow structure of the simulation for validation purposes.

Comparison between the model output and the lidar data shows promising agreement between the two. Items compared include boundary layer depth, land breeze depth, wind speeds and direction, cellular size of the structures in the convective boundary layer flow outside of the land breeze, land breeze front movement and position, and several meteorological variables recorded near the lidar site on the date of the land breeze. This agreement, coupled with the significantly improved simulation results over those obtained with a traditional mesoscale simulation illustrates the merit of using the dynamical downscaling technique in this and similar situations.

Acknowledgements

Thanks go to my academic advisor, Dr. Gregory J. Tripoli, for his support, assistance and motivation throughout this research, as well as for his advice in the use of the UW-NMS. Special thanks also go to Dr. Edwin Eloranta, my unofficial advisor in the area of lidar research for his ideas on using the VIL data for validation, and for his patience in teaching me about the lidar system and world. Also thanks to Ed for providing computing resources to run these simulations on. Additional thanks go to readers Dr. Ralf Bennartz and Dr. Michael Morgan and Ms. Amanda Adams for their time and insight into the matters addressed in this work.

The Lake-Ice data from the 21st of December, 1997, is available thanks to the crew working onsite during that time. Members of that group include Mr. James Hedrick, Mr. Ralph Keuhn and Dr. Shane Mayor, without whose hard work this project would not have been completed. Thanks to Mr. Pete Pokerandt for his assistance in configuration of software and the NMS code, and also to Mr. Joseph Garcia for his assistance and answers to my endless questions on computer related issues, as well as his help in solving countless programming and software dilemmas.

Finally, thanks go to my family for their support in everything I do, and especially to Rebecca Flood for her patience, support and love over my first two years here in Madison. Our adventures and diversions keep life interesting and keep me motivated to enjoy all aspects of life.

Contents

List of Figures

Chapter 1

Introduction

1.1 Motivation

Since the majority of life on this planet is connected closely to the surface of the earth, the planetary boundary layer is in the unique position of surrounding and influencing everyday life on earth. Therefore, a thorough understanding of the processes occurring in this thin layer becomes a vital part of forecasting the meteorological events taking place around us. One common example that comes to mind is a windy day in a city. Although prevailing surface winds may come from one direction, it is very unlikely that winds will be coming from that direction in every alleyway, street corridor, or tree filled park. What one individual experiences may be totally different from what someone else experiences a hundred meters or less down the road. It is very important to realize, however, that these small-scale effects are, in many cases, simply localized versions of the large-scale flow. Whether it is the extra friction on the wind from buildings, or localized thermal gradients forcing atmospheric phenomena, without proper large-scale conditions, commonly witnessed events may never take place. For example, without large-scale pressure gradients, there is no wind to funnel down an alleyway, and with too large of a prevailing wind, a land or sea breeze may never become established.

This work will investigate the ability of a mesoscale model to replicate flow structures at the local and micro-α scale from meso-α and larger events through the use

of a dynamical downscaling technique. Contrary to many previous attempts at replication of structures at the microscale, this study will utilize grid nesting in order to attain the high resolutions needed for production of structures of this nature. All information used by the simulation to initiate motions on the fine scale is derived through interpolation from the large-scale circulation (meso-α) of the atmosphere and its interaction with local, resolvable topographical forcing. An example of one of these local forcings is the small-scale temperature gradients between different surfaces. **It is hypothesized that under certain situations, correct simulation of the meso-α scale, together with sufficient resolution to accurately represent the local topographical influence will allow accurate representation of structures at the fine scale (micro-α) and their evolution.** To test the validity of the produced results, the output from simulations will be compared to aerosol-backscatter lidar observations of the microscale event. **The primary objective of this work, therefore, will be to investigate through comparison with scanning lidar data, the ability of the modeling system used to simulate these small scale type events through utilization of the dynamical downscaling method, and to attempt to determine what information is gained from these high resolution results**.

The majority of this work discusses simulations and observations of a land breeze situation observed in Sheboygan, Wisconsin on December 21, 1997. With weak synoptic flow, and a moderate temperature gradient between the lake and land surfaces, this particular land breeze is a great example of a microscale, localized event that is greatly influenced by the synoptic and mesoscale conditions. Additionally, the fact that lidar observations are available for this particular event adds to the attractiveness of this

specific case. The observations presented were taken as a part of a large field campaign during the winter of 1997-1998. These experiments, known as the Lake Induced Convection Experiment (Lake-ICE, Kristovich et al. 2000) were proposed to study the convective boundary layer (CBL) over Lake Michigan during early winter cold air outbreaks. The University of Wisconsin Volume Imaging Lidar (UW-VIL), with which all of the lidar observations included in this study were taken, was one of the instruments deployed during this campaign, along with several research aircraft, surface based observing systems, and several radar systems. In addition to data from some of these observing platforms, observations from a National Data Buoy Center observing station a few hundred meters from the lidar are available for comparison with model output.

Now that the primary objectives of this work have been presented, the remainder of this introduction will provide a brief overview of some of the methods and tools utilized in this study. Integrated along this is a background of some previous work done in similar areas and an outline of the rest of the thesis.

1.2 Dynamical Downscaling in Numerical Weather Prediction

The idea of increasing the complexity of the numerical simulation along with advances in computing technology has become a prevalent one in science and technology fields over time. Today, many numerical models include grid-nesting capabilities, in order to increase resolution in a particular area, along with more complex parameterizations and microphysical schemes. Numerical weather prediction is now at a stage where the motion of meso-α scale and larger meteorological systems can be predicted with respectable accuracy in the 24-60 hour time span. This fact makes the ability to downscale from the large scale atmospheric state, as measured by global

observation networks, to disturbances and events spanning much smaller distances than resolvable by these networks a very useful one. Whether micro-α scaled events can be derived directly from the predictable scales discussed above is yet to be determined. Since the lifespan of the large scale systems is typically on the order of days to a couple of weeks, attempting to determine the dynamics of that system for a few hours into the future may be possible.

As outlined in Mayor (2001), numerical simulation of the atmosphere generally falls into one of two categories. The first of these is pattern predictability, while the second is statistical results from pattern forecasts. Most numerical weather simulations fall under the first category, since they are initialized with several basic atmospheric variables such as winds and temperature from a network of atmospheric observation sites. Because of the relatively high resolution of the observations to the size of the systems being reproduced, the initial position and qualities of these synoptic features are introduced quite accurately. The simulation then produces a deterministic forecast by carrying this initial state forward in time using the governing equations of atmospheric motion.

The second category involves simulations that are initialized without prior knowledge of the state of the atmosphere, including the size, position, and shape of disturbances. Many climate models, and all large eddy simulations (LES) fall into this category. In this case, the model is intended to simulate the statistics of an atmospheric state it knows very little about, given some initial and boundary conditions. Here, disturbances form due to a continuous external forcing upon the system, which are then carried forward through the equations governing atmospheric motion.

The nesting technique utilized in this work straddles the line between these two types of simulations. The large-scale is initialized using observations taken at high resolution relative to the domain size. The deterministic prediction of these meso-α and larger features is carried out, and can be verified through analysis of future observations taken by the same network. The nested portion of the simulation, however, begins to resemble more closely the second category of simulation discussed above with increases in resolution. In these domains, the initial state is determined by the boundary conditions, interpolated down from the next coarser domain. The high resolution is utilized in order to increase the accuracy of the land-surface forcing. In the inner domains, there may not be any data points present from the initial analysis, and the domain may be initialized entirely from the domain above it. These portions of the simulation therefore cannot be verified using the large-scale observing network, and alternate means must be employed. Both the large-scale and microscale disturbances evolve simultaneously.

Simulations at high resolutions are more commonly run in the form of large eddy simulations (LES). Studies of the atmospheric boundary layer utilizing this technique are numerous (e.g. Wyngaard, Peltier and Khanna, 1998; Moeng and Sullivan, 1994). However, the majority of these studies have been idealized cases with well-established boundary conditions, and little or no change in the synoptic forcing involved. Because of the lack of synoptic and mesoscale influence, these simulations can not readily predict the evolution and decay of boundary layer structures that are directly resultant from that larger scale, since the evolution of the larger scale would be necessary for a change in the state of the small scale event. Additionally, these studies are often carried out in order to gain statistics for comparison with the statistics of the observed atmosphere. In a non-

idealized case, such as the land breeze, this becomes much more difficult to do because of the large gradients involved in many of the parameters. These gradients and undulations could easily be lost in the statistics, if not actively sought after.

Some studies of interest on the LES technique have been carried out by Agee and Gluhovsky (1999), Wyngaard et al. (1998), and others. Agee and Gluhovsky addressed model sensitivities to the domain and grid size employed, as well as the size of the time step used. They noted that LES are required to have grid scales that are capable of reaching the inertial subrange. Additionally, they add that field observations and data will contain the effects of larger scale phenomena, and therefore, efforts must be made to simulate those phenomena to the best of our ability. Therefore, the computer domain must be large enough to capture meso-α scale events, as well as semi-permanent mesoscale structures such as rolls or cells that are capable of responding to energy cascading effects of the thermals and large eddies. This implies that the domain must be two and a half times as large as the characteristic length scale of the phenomenon to be simulated. This can be readily achieved with the downscaling method, since resolutions range from tens of meters in the inner domain, to thousands of meters in the largest domain. It is very important to note that the downscaled simulation is not considered to be a form of LES, and is not expected to accurately reproduce the timing and exact statistics of all turbulent features of the flow. What is sought after, however, is whether the downscaling technique can accurately reproduce the major characteristics and evolution of the land breeze itself. These features are more likely due to the interaction between the meso-α features with the land surface characteristics portrayed at the microscale.

1.3 Predictability and Forecast Improvement

At this point it is necessary and important to briefly discuss the topics of predictability and forecast improvement. Many questions about these topics remain unanswered. If the resolution of the inner domain is increased, what information do we really gain? Are the features resolved improving our knowledge and understanding of the atmospheric state? Can features not resolved or predicted at the larger scales really be accurately represented at finer scales?

Although the answers to some of the above questions may seem obvious, deeper thought into these issues reveals some extremely difficult inquiries about the benefits of downscaling. Although previous works (Clark and Farley, 1984; Phillips and Shukla, 1973) have shown that increased resolution can help us to gain insight into structural features, these improvements are typically made in the gathered statistics of the event. In this study, it is believed that a very small portion of the variance of the land breeze structure actually comes from large eddies. Rather, the main influences are the meso-α scale features such as the strength and direction of the large scale flow and the position of mesoscale frontal systems, together with the highly resolved topographical influences such as the thermal gradient between the shoreline and Lake Michigan. Since this is the case, and the land surface features are highly predictable, the predictability of the micro-α scale event will take on the predictability of the meso-α scale. This brings up new questions: What scale is needed to accurately reproduce the features and characteristics of the land breeze? Do we need 32-meter resolution, or will 100-meter resolution capture the same general characteristics?

Due to the fact that there are several scales being simulated simultaneously, it becomes very difficult to determine the accuracy of the simulation. Very small errors at the large scale may effect the fine scale to a much more noticeable extent. These errors may be so miniscule at the large scale that they are not even noticed in an evaluation of the large-scale evolution, and an assessment of the accuracy of the simulation at the meso-α scale may indicate a very precise simulation. These same errors may have severe implications upon the accuracy of the resulting high resolution forecast. But again, what is meant by severe? In the case of the land breeze, is a frontal displacement of several hundred meters in the high-resolution domain considered a poor forecast, when the data that the simulation is initialized from has a resolution of tens of kilometers? If so, is it still considered a poor forecast at 250-meter resolution? When the resolution is increased, most would expect the accuracy of the simulation to follow suit. The simulated event could appear to be highly representative of the observed flow if comparison of observations and the statistics of the flow is done over the entire inner domain, but may in fact be horrendous if the comparison is done at a single point that happens to lie in an area that is on the wrong side of the front. One could argue that the replication of the event and some (not necessarily all) of its characteristics is a major improvement over a simulation that does not resolve the event at all, even if some of the positions of the micro-α structures are misplaced. At the same time, someone with interests inside the several hundred meters of missed frontal position would likely disagree.

The questions presented above hold the key to determining the usefulness of dynamic downscaling in micro-scale simulation. They will be addressed in regards to the land breeze studied here in the following chapters.

1.4 Lidar

In a method similar to that used by radar (radio detection and ranging) and sonar (sound navigation and ranging), lidar (light detection and ranging) operates on the idea that a light pulse emitted to the atmosphere will be scattered by molecules and particulates in the atmosphere. The primary difference between these three methods, of course, is the wavelength of the energy used for the detection. In the case of lidar, some of the light energy that is scattered in the atmosphere from the initial pulse will be returned towards the system's receiver. Here the light is collected by a telescope, and directed towards a detector which can determine the amount of light back scattered (scattered at the receiving optics) by the atmosphere.

There are several prominent types of lidar systems currently in operation. One of the main distinctions between the types of systems is whether it measures only elastic scattering occurring in the atmosphere, or both elastic and inelastic scattering. Elastic scattering occurs at the same wavelength as the emitted laser pulse. In inelastic scattering, the wavelength of the reemitted light is shifted when compared to the emitted light (Kovalev, 2004). Raman scattering is a good example of inelastic scattering. High spectral resolution lidars have the capability to measure and separate the molecular and particulate contributions to the backscatter signal received (Grund and Eloranta, 1991). Additionally there are differential absorption lidar (DIAL) systems that transmit two wavelengths and use the fact that certain particulates and molecules absorb light energy

at specific wavelengths to determine concentrations of these specific absorbing constituents in the atmosphere.

Lidar systems can be set up in many configurations. Some always look almost directly upward (usually at a small angle to zenith in order to better handle specular reflections), while other systems have scanning capabilities, allowing them to take volumetric measurements. All systems, however, have three main subsystems. These include a laser/transmitter for emission of the light signal, a receiver/detector to collect and measure the backscattered signal and some sort of recording system in order to control the system and analyze data that is being received (Kovalev, 2004).

One important consideration in lidar studies is the fact that not all lidar systems are eye safe. That is, some lidar systems utilize wavelengths of laser light that could be damaging to the eye if viewed directly. Generally speaking, wavelengths under 315 nm and wavelengths over 1700 nm are absorbed in the cornea, while light in the area between 315 and 400 nm is absorbed by the lens of the eye. Energy from light at wavelengths between approximately 1400-1700 nm is dispersed through the entire eye. Finally, the region between 400 and 1400 nm can cause irreversible retinal damage if exposure occurs at sufficient intensity levels. Radiation at these wavelengths is not absorbed until it reaches the retina, causing serious damage. Therefore, systems operating at these wavelengths are not safe for viewing, and should only be viewed directly using safety glasses. Because of these potential hazards, great care must be taken when using systems utilizing these wavelengths outdoors, in order to prevent accidental viewing by non-involved parties. In the case of the land breeze, this means that the lidar

system used could not observe the upstream structure of the flow, and only was able to capture the boundary layer structure out over the lake.

1.4.1 The Lidar Equation

Backscattered light incident upon the photodetector of a system consists of several different constituents. Included in these are the elastic single scattered component, the elastic multiply scattered component which has been scattered several times before reaching the receiver, the inelastic components, and the background flux due to light from the sun.

Therefore, the equation for total energy incident upon the receiver looks like:

$$N(r) = \frac{N_0}{r^2}\frac{cA}{2}\left[\beta_a(r)\frac{P_a'(180°,r)}{4\pi} + \beta_m(r)\frac{P_m'(180°,r)}{4\pi}\right]\exp\left[-2\int_0^r \beta_e(r')dr'\right] + M(r) + B \quad (1.1)$$

where: $N(r)$ is the total number of photons incident on the receiver field from inside the field of view, from range R, N_0 is the number of transmitted photons, c is the speed of light, A is the area of the receiver telescope, $\beta_a(r)$ is the aerosol scattering cross section per unit volume (m^{-1}), and $\beta_m(r)$ is the molecular scattering cross section per unit volume (m^{-1}). $P_a'(180°,r)$ and $P_m'(180°,r)$ are the aerosol and molecular backscatter phase functions, respectively, $\beta_e(r')$ is the extinction cross-section per unit volume (m^{-1}), $M(r)$ is the contribution due to multiple scattering, and B is the contribution due to background sources.

From here, a simplified version of the single scattering elastic lidar equation can be obtained by assuming multiple scattering and molecular scattering can be neglected at the particular wavelength used, and background sources are corrected for:

$$P(r) = \frac{E}{r^2} K \beta_s(r) \frac{\mathscr{P}(180°, r)}{4\pi} \exp\left[-2\tau(r)\right] \tag{1.2}$$

Where: $P(r)$ is the energy incident upon the receiver, E is the transmitted laser pulse energy, r is the distance along the path of the light, $\beta_s(r)$ is the scattering cross section per unit volume (m^{-1}), K is a system constant, equal to $\frac{cA}{2}$. $\mathscr{P}(180°, r)$ is the aerosol backscatter phase function, and finally $\tau(r)$ is the one way optical depth between the lidar and the backscatter volume at r.

1.5 Validation and Comparison

One of the most important aspects of studying microscale phenomena such as the land breeze using numerical simulation is the method used in validating the simulation output. Typically, LES studies have been mostly statistical in nature, and therefore, measurements taken for validation purposes have largely been focused into statistical quantities as well. As briefly mentioned earlier, this does not necessarily give one a good picture of the complete structure of the flow, since several different scenarios can lead to similar statistics. A suite of measurements, including ones that visualize the studied scenario similar to those taken by lidar systems becomes a very effective means for comparison, since now not only can statistics be compared, but the structure and appearance can also be validated. For the most part, studies have tended to concentrate on either the numerical simulation or observation of these structures, and little has been

done in linking the two modes of study. This study attempts to link the observation and simulation of this particular event through inter-comparison of like quantities derived from both modes of study.

The limited number of studies that do combine simulation and observation show promising results in the area of model validation. Shafran et al. (2000) utilized large-scale wind and radiosonde measurements in order to validate the 12 and 4 km resolution grids in their study of how the use of different boundary layer schemes may affect the output on larger scales. Clappier et al. (2000) utilized a somewhat more thorough dataset in order to attempt validation of their numerical simulations of the sea breeze and its relation to air pollution in the Athens area. Aircraft measuring atmospheric constituent concentrations, specifically O_3, NO and NO_2, were used, as well as a differential absorption lidar, and twenty ground stations measuring typical atmospheric quantities such as wind, temperature, and relative humidity. This data set allowed the authors to make more direct comparisons at higher resolutions. Still, the model domain used only had a high horizontal grid resolution of 2 km. This is not a high enough resolution to effectively simulate small-scale land breeze events. It would be difficult to justify validation of higher resolution simulations using this type of set up, since the measurements taken are point measurements, meaning that the measurement only observes the state of one point of the atmosphere at any given time. Because of this, a three dimensional analysis of the atmospheric state at higher resolutions than those investigated would be difficult to attain with the data available.

In order to achieve this four dimensional analysis (three spatial and time), remote sensing techniques utilizing high temporal and spatial resolution, such as the lidar

technique, need to be applied. Several studies in recent years have employed lidar backscatter measurements for comparison with high-resolution numerical simulations, including works by Darby et al. (2002), Fast and Darby (2004), Duclaux et al. (2002) and Mayor et al. (2003).

The study done by Fast and Darby utilized a Doppler lidar in order to observe wind structures in down-valley and canyon flows. In order to achieve accurate comparisons, the authors obtained radial velocities relative to the lidar location at each model grid point, interpolated these velocities vertically in order to create planes corresponding to the constant elevation scans taken by the lidar. Then, observed radial velocities were averaged over each model grid cell for statistical evaluations. Predicted wind fields, as pointed out by the authors, cannot be evaluated fully, since a particular observed radial velocity could be obtained from more than one wind direction. One important finding in this work was that the comparisons yielded very high correlation coefficients in cases that were mostly synoptically forced, while highly localized features had lesser correlation. This indicates that the model did a good job of capturing flows linked to synoptic patterns, as might be expected. Localized flows, however, were often misrepresented in the model, mainly with regard to the timing of the event.

Agee and Gluhovsky (1999) claim that if comparison is to be done between LES and field observations, that a bandpass filter must be implemented to the observed data in order to more accurately filter out of it the effects of the large scale as well as the very small features not resolvable by the model resolution. Since, in the present study the large scale is incorporated, and the resolution of the simulation is somewhat similar to that of the lidar, this is seemingly not needed.

The work done by Mayor et al. also presents some interesting results. For one, it is one of few comparisons between very high-resolution boundary layer structure observed by lidar, and high-resolution numerical simulations of similar structures in the boundary layer. An important aspect to this study was that the lidar observations include effects from all scales, while the LES output presented, as mentioned earlier on, did not necessarily incorporate influences from the large scale. This made it very difficult to make direct comparisons between the two. It was, however a breakthrough work in terms of comparison techniques used for the validation process. A virtual scattering parameter was developed in order to relate directly the model output, specifically the relative humidity, to the output from the lidar. This was a large step in comparison between numerical and observed features. Additionally, cells were compared statistically, in a manner that allowed the same statistics to be gathered from the lidar data as gathered from the model output. These techniques were reasonably portable and can be applied to future studies in this area.

1.6 The Land Breeze

The land breeze is one of the most commonly witnessed small-scale events due to its connection to the shoreline, where a large portion of the world's population is gathered. Although not as commonly studied as its more popular counterpart, the sea breeze, a significant effort has been put forth to better understand the complex nature of this microscale event. This effort has been increased with the findings that these circulations can have significant impacts upon pollution dispersion, as discussed in Keen, Lyons and Schuh (1979) and Clappier et al. (2000). Additionally, the land breeze can have a significant effect upon the formation of shore-parallel snow bands, which can form along

the updraft region established at the convergence zone between a land breeze and the opposing prevailing winds or a land breeze from the opposite shore of a lake (Ballentine, 1982; Elsner et al., 1989; Hjelmfelt 1990, 1992; Passarelli and Braham, 1981).

The circulation establishes itself when a substantial temperature gradient forms between a colder land surface and a warmer water surface. The pressure gradient established as a result of this flow causes air to flow offshore, and the circulation is formed as a result of continuity (Jeffreys, 1922; Haurwitz, 1941,1947; Schmidt, 1947). Therefore, the size of the temperature gradient between the air over the land surface and that over the water surface is a very influential factor in determining the strength of a land breeze.

In addition to the magnitude of the temperature gradient between the air over land and water, Haurwitz adds that there is also a dependence upon the strength and direction of the synoptically forced flow. Figure 1.1 shows the December 21 case reviewed in the present study, in which the prevailing winds are light and directly opposing the land breeze, leading in part to its well-defined appearance. For a sea breeze situation, Schmidt recognized a similar effect, noting that the most striking realization of the phenomenon occurred into a moderate offshore flow. The direction of the prevailing wind is also somewhat important in determining whether or not a land breeze will form at all.

Estoque (1962) determined that for the case of a sea breeze, an offshore (into the sea breeze) background flow is most favorable for the formation of a sea breeze, while onshore flow (with the sea breeze) is the least favorable. Zhong and Takle (1993) also discussed the effects of large-scale flow on the land breeze circulation, noting that, in the case of a sea breeze, onshore synoptic flow advects cold air toward the land surface

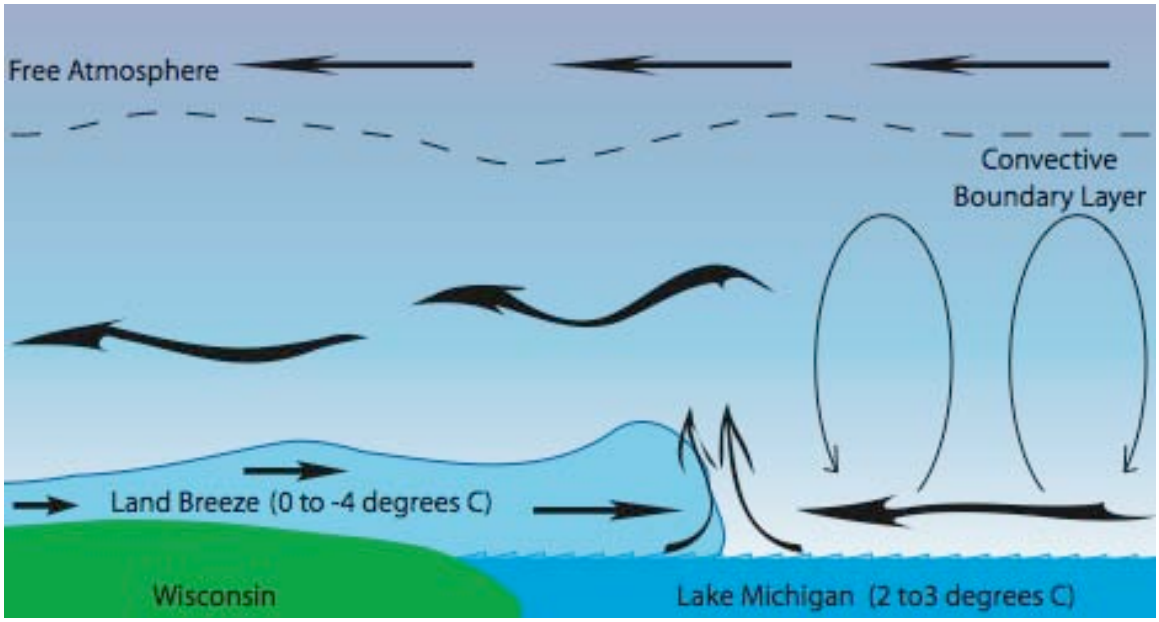

Figure 1.1: Idealized illustration of the December 21 land breeze.

reducing the horizontal temperature gradient and thus, weakening the circulation. This finding would seem to indicate that any flow perpendicular to the temperature gradient would weaken a potential circulation, including the circulation itself, since the thermal gradient would be reduced over the area involved. Also discussed by Zhong and Tackle is how increased prevailing wind speeds decrease the strength of the convergence of these circulations, as well as the vertical motions associated with that convergence. Finally, they concluded that stronger and deeper land breezes are associated with offshore large-scale flow, while onshore flow generates weaker and shallower land breezes. This finding is shown in several cases of Lake Michigan land breezes, which have a very well defined shallow, and relatively weaker land breeze flowing into the prevailing flow, and an ill-defined, stronger land breeze flowing along with the prevailing flow.

Because of its colder nature, the land breeze undercuts and lifts the warmer air situated over the water surface (Neumann and Mahrer, 1971). This intersection of the two air masses leads to a substantial updraft, especially in the case where the prevailing wind is opposing the land breeze. Mitsumoto (1983) also found the land breeze to undercut the ambient air, using a laboratory tank experiment. Also discussed in this study is the difference between the shape of the land breeze head and that of the sea breeze. In the tank, the sea breeze head was typically rounded with a strong updraft, while the land breeze head was flatter and more wedge-shaped. This is likely caused by the experimental design, with only the land surface being heated, causing a significantly less stable environment for the sea breeze to penetrate into than that encountered by the land breeze. The lack of instability at the head of the land breeze inhibits the formation of an updraft and raised head. An example of a more rounded land breeze head is that observed in Tokyo by Ohara et al. (1989) using tethersondes and an acoustic sounder. Here, the land breeze does move into unstable conditions, and the head is more rounded as a result. The stability of the surrounding flow therefore influences the structure of the land breeze, and possible scenarios for this flow are discussed in the next section.

The shape of the head of the land breeze can have significant implications on the structure of the atmosphere downwind of the head. There are clear indications that Kelvin-Helmholtz type billows will form behind a rounded head, leading to significant horizontal variation of vertical wind speed (Ohara, 1989). These billows are responsible for the formation of an interface region between the land breeze and the free stream flow.

Additional observational studies of the land breeze have been completed by Schoenberger (1986), using Portable Automated Mesonetwork (PAM) II stations, Agee

and Hart (1990), by airplane, Winstead (2000) using Synthetic Aperture Radar (SAR), and Kolev (1998), Eloranta et al. (1999) and Nakane and Sasano (1986) using scanning lidar systems. Schoenberger's study reveals what mesoscale and synoptic conditions favor the formation of the land breeze. He found that the land breeze over Lake Michigan is most pronounced when the skies over the lake are clear, and the onshore flow is light. These are typical conditions in the latter stages of a cold air outbreak. Also, it was pointed out that lake induced pressure troughs, favorable for the formation of land breeze circulations, are a rather common regional mesoscale atmospheric feature over Lake Michigan. These findings are supported in Winstead's study, along with several others that note land breeze formation under these conditions.

Complementing these observational studies is a similar list of attempts at modeling the land breeze. Some examples include the previously mentioned studies by Keen et al. (1979), Ballentine (1982), Alpert and Neumann (1983), and Hjelmfelt (1990). These studies did not attempt to simulate the dynamics of the land breeze itself, but rather simulated the occurrence of land breeze, and any effects that it may have on other phenomena such as lake induced snow and pollution. Relatively large domains were utilized at resolutions too coarse to simulate the small-scale features of these circulations. A more detailed numerical investigation of the land breeze itself was carried out by Sha et al. (1991), in which the Kelvin-Helmholtz instability (KHI) of the gravity current is investigated. As discussed by Ohara, it is stated that KH billows allow for turbulent mixing between two different density fluids in the wake formed by the frontal region, or in the case of a land breeze flowing into a prevailing headwind, the area behind the head of the flow. Also, it is observed that the head of the circulation is typically around two

times deeper than the following flow. Although much of this work is dedicated to the simulation of the sea breeze, a land breeze flowing into a convective boundary layer can act similarly, and many of the fluid dynamical aspects of the flow will be similar to that of the sea breeze.

1.7 Overview

Having described at a very basic level the tools required for this work, as well as some of the history of similar studies, and having presented the aim of this particular study, this section is presented to introduce the rest of this work. Chapter two will present a brief overview of the University of Wisconsin Volume Imaging Lidar (UW-VIL). Chapter three will review the Lake-ICE experiment, as well as the synoptic and local meteorological conditions for 21 December, 1997, the date that the land breeze was recorded in the lidar data. Chapter four will discuss the results from the numerical simulations of the land breeze. Chapter five compares the lidar data with the model results, using a virtual scattering parameter (Mayor, 2001), as well as by comparison of the major features of the flow, including boundary layer height, land breeze depth, depth of the land breeze head, eddy and cell sizes in the offshore convective flow, wind speeds and direction of both the onshore and offshore flows, and other meteorological measurements compared with the data at the National Data Buoy Center site near the lidar location. Chapter six will focus on conclusions as well as recommendations for future studies in this area. Additionally, there are two appendices, the first of which focuses on the adjustments made to the University of Wisconsin Non-Hydrostatic Modeling System (UW-NMS) and the second of which discusses the formulation of the NMS.

Chapter 2

The University Of Wisconsin Volume Imaging Lidar

2.1 Specifics

The University of Wisconsin Volume Imaging Lidar (UW-VIL) is currently one of three systems run by the lidar group at the University of Wisconsin – Madison. Of the three, it is the only one that is designed to scan the atmosphere to capture three or four-dimensional images of atmospheric aerosol backscatter. Although it can only determine relative backscatter, it is useful in mapping differences in backscatter such as those typically found between the planetary boundary layer and the free atmosphere, at the edges of clouds and fog, and between pollution plumes and the free atmosphere.

The first version of the VIL was created in the early 1970s, when scanning capabilities were added to an already operative system. Throughout the 1970s, improvements and updates were put in put into place in order to improve the data collection and scanning capabilities of the system. The mid 1980s saw the creation of a system resembling the current version of the VIL. A new 20-watt Nd:YAG transmitter was incorporated into the system at this time, and data collection hardware was updated. Additionally, a beam steering unit (figure 2.1), to facilitate efficient scanning of areas and volumes was added and the unit was moved to a trailer van (figure 2.1) for portability. It

was during the mid 1990s that the most recent updates were completed, with a new Infinity Coherent laser and Silicon Graphics workstation added to the system.

When compared with most other current systems, the VIL is a relatively simple type of lidar. However, it does have powerful transmission and detection capabilities. The system operates at 1064 nm, utilizing the Infinity Coherent laser. Use of the 1064 nm wavelength has two primary advantages. The first is that the solar signal is weaker at 1064 nm than it is at 532 nm. The second is that there are more initial photons present, allowing an increase in signal to noise ratio, which is primarily limited by the amount of photons present. Unfortunately, at this wavelength, the VIL is not eye-safe, meaning that its deployment is limited to areas that are scarcely populated, and not heavily traveled. In addition, a safety observer is employed to cut transmission if human activity is spotted inside the scan area.

The Infinity laser has some unique characteristics. The seed laser is diode pumped, and amplification occurs in a pair of flash lamp pumped Nd:YAG rods. This could present potential issues, since the high temperatures produced by the flash lamps could change the shape of the wave front of the amplified light. Because the wave passes through the amplification rods a total of four times per pass, twice in one direction, and twice in the opposite after reflection, this wave front distortion could be very significant. This problem is addressed using a phase conjugate mirror instead of an ordinary mirror (figure 2.2), which essentially inverts the waveform to allow it to revert to its original shape after passing through the amplification rods the second time.

Figure 2.3 is a schematic illustrating the components of the VIL. The alignment mirror that aligns the outgoing transmitted pulse and the telescope is mounted on the

Figure 2.1: The VIL's beam steering unit (left) and the system assembled inside of the semi-trailer (right) with the beam steering unit visible on the roof.

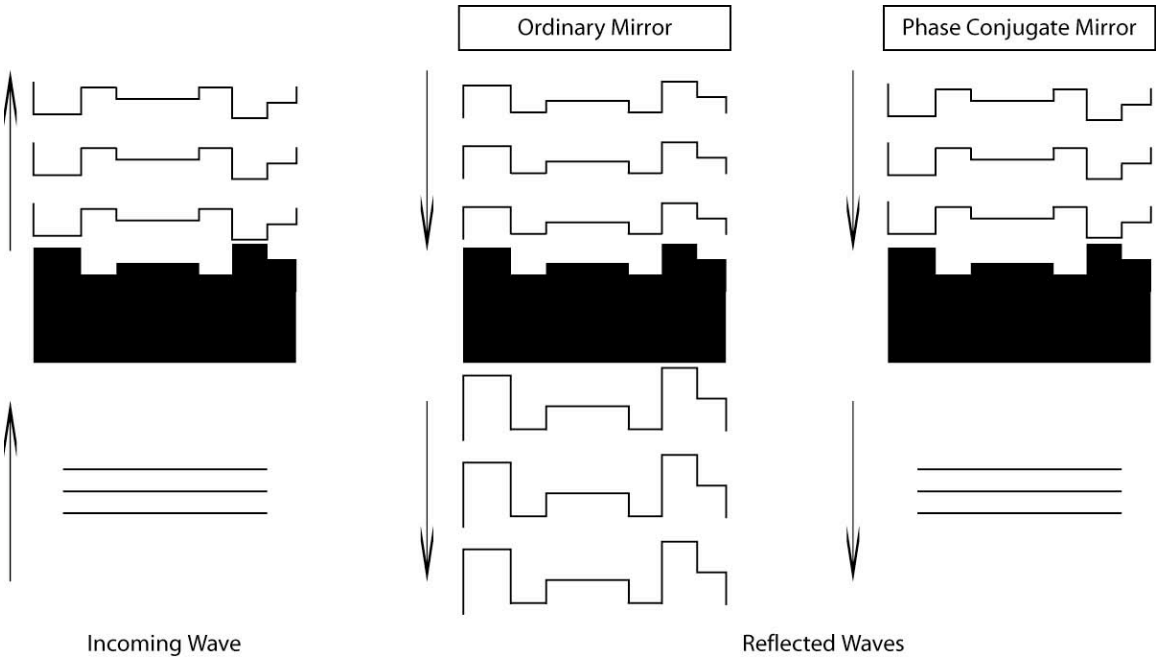

Figure 2.2: An illustration showing the effect of the phase conjugate mirror employed in the Infinity laser. The leftmost column shows the incoming wave and the waveform after passing through the amplifiers the first time. The right two columns show the waveform after reflection and passing through the amplifiers for the second time using a traditional mirror (center) and phase conjugate mirror (right).

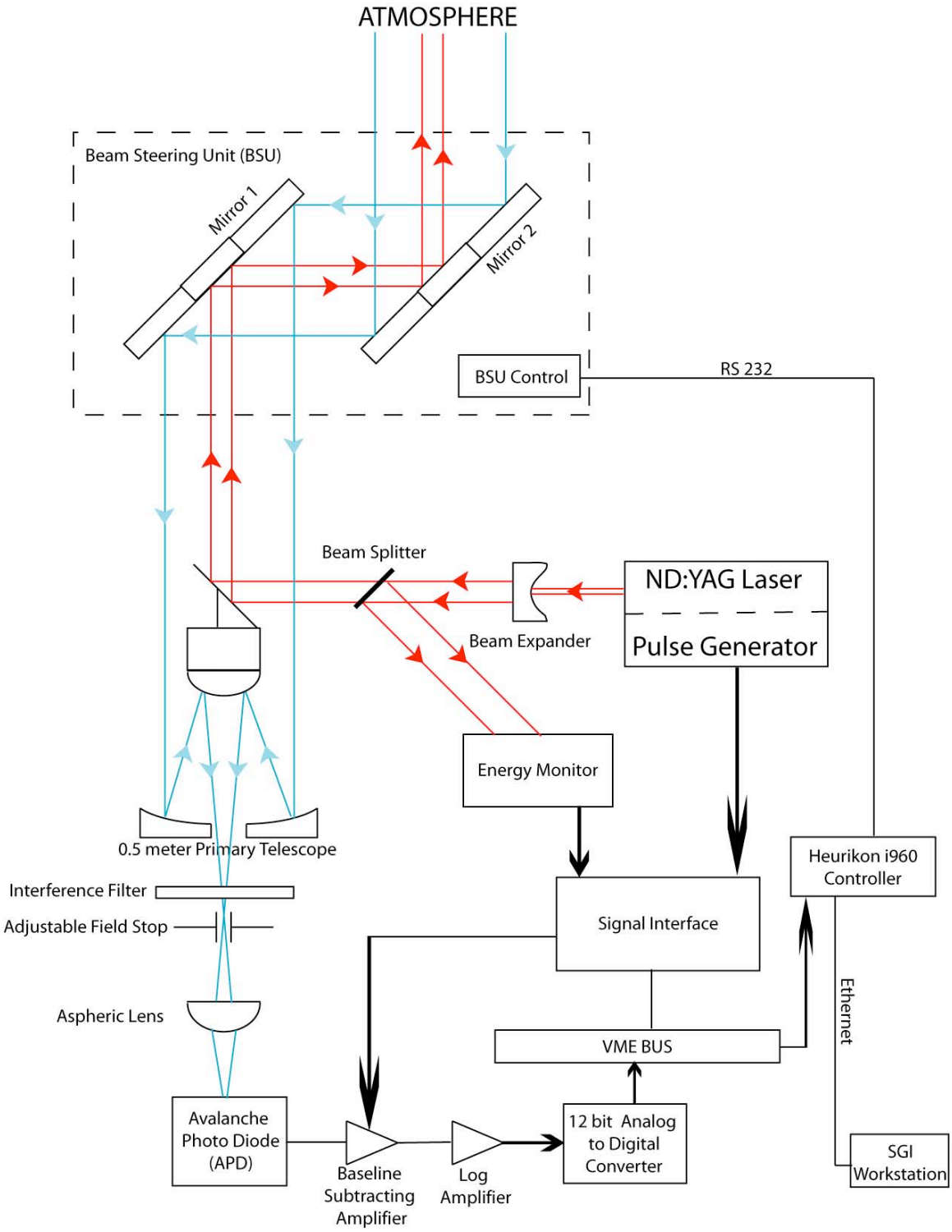

Figure 2.3: A schematic of the VIL.

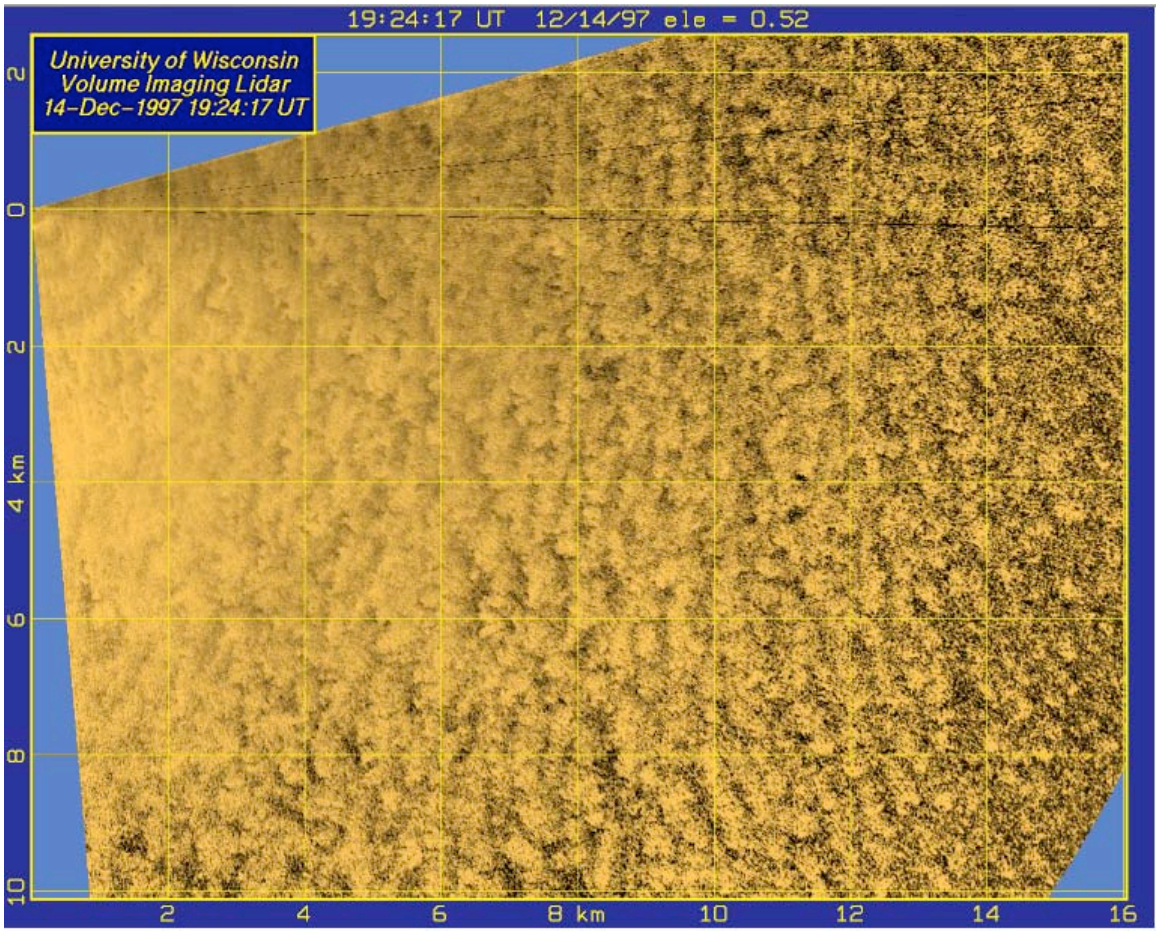

Figure 2.4: Output showing an example of the ringing (concentric rings, upper left) that occurs when the baseline-subtracting amplifier is saturated by stray scattered light from the initial laser pulse inside the system.

telescope secondary. This ensures that the receiver is pointing in the same direction as the outgoing laser pulse. One issue with such a configuration is that light scattered by the optical components from the initial laser pulse can reach the detector and saturate the baseline-subtracting amplifier. Because recovery from such saturation does not happen instantaneously, the measurement would be effected. In order to minimize this occurrence, several tubes and caps are used to attempt to isolate the outgoing pulse and prevent any scattering from reaching the detector. This is not done between the laser and

the alignment mirror, however, in order to maximize telescope area. Therefore, some effects are seen in the data, most commonly in the form of ringing when the data is viewed at high resolutions (figure 2.4). Additionally, each of the two flat mirrors contains two parts, with the center portion being able to handle the intensity of the outgoing pulse, and the rest of the mirror capable of reflecting the weaker incoming signal.

The system telescope utilizes a 0.5-meter primary mirror, and a secondary mirror, together set up to form a Cassegrain style telescope. From here, the return signal passes through an interference filter, so that light that is not at the wavelength of the laser does not get to the detector. The optical filter used transmits light in a 1 nm range around the emitted wavelength, reflecting light at other wavelengths. Next, a field stop is used in order to narrow the field of view and again attempt to decrease noise sources. An aspheric lens is utilized in order to allow for the telescope field of view to be projected onto the detector, after passing through the field stop. An avalanche photo diode (APD) is used for detection purposes, rather than a photomultiplier type system in order to increase the efficiency of detection. From here, the now electric signal passes through a baseline-subtracting amp to isolate the signal from outside noise, and a logarithmic amplifier. The logarithmic amplifier increases weaker signals a larger amount than stronger ones, allowing increased ability to see features in the aerosol structure. Additionally, the logarithmic amplifier transforms the one over range-squared dependence to be represented linearly, making it easy to remove from the data. The signal is then converted from analog to digital, and that information is passed along to the system controller, as well as to a workstation for processing.

Some additional corrections are made to the data. A high pass median filter can be employed in order to attempt to visualize the aerosol structure hidden in shadows caused by highly scattering features. Additionally, since these shadows hinder efforts to gather information about the motion of the aerosol field since they are essentially discontinuities in the field, filtering them out will increase the accuracy of cross-correlation techniques used in determining the aerosol motion.

Another correction implemented is a distortion correction, which reduces errors caused by the finite amount of time needed to complete an RHI volume scan. Since a scan of this nature takes two to three minutes to complete, and the aerosol structures observed could have been advected significantly with a mean wind, this correction is vital to tracking aerosol position, and to creating a continuous scan volume. In the correction, an estimate of the mean horizontal wind vector is utilized to displace individual backscatter profiles by the product of the wind speed and the time change since the scan. This method is further discussed in Sasano et al. (1982) and Schols and Eloranta (1992).

2.2 Scanning Patterns

One of the unique features of the VIL is its ability to scan through the atmosphere using the beam-steering unit. The motors used to turn the beam-steering unit allow the system to scan through any point in the sky. The azimuth angle can cover 360 degrees, while the elevation angle can range from zero to 90 degrees, completing a hemisphere of scanning volume. Typically, the full 360-degree range of the azimuth is not utilized since the system is focusing on a particular area. Additionally, since the system is not eye-safe, the safety of the public and of the operators also factors into not using a 360-degree scan pattern.

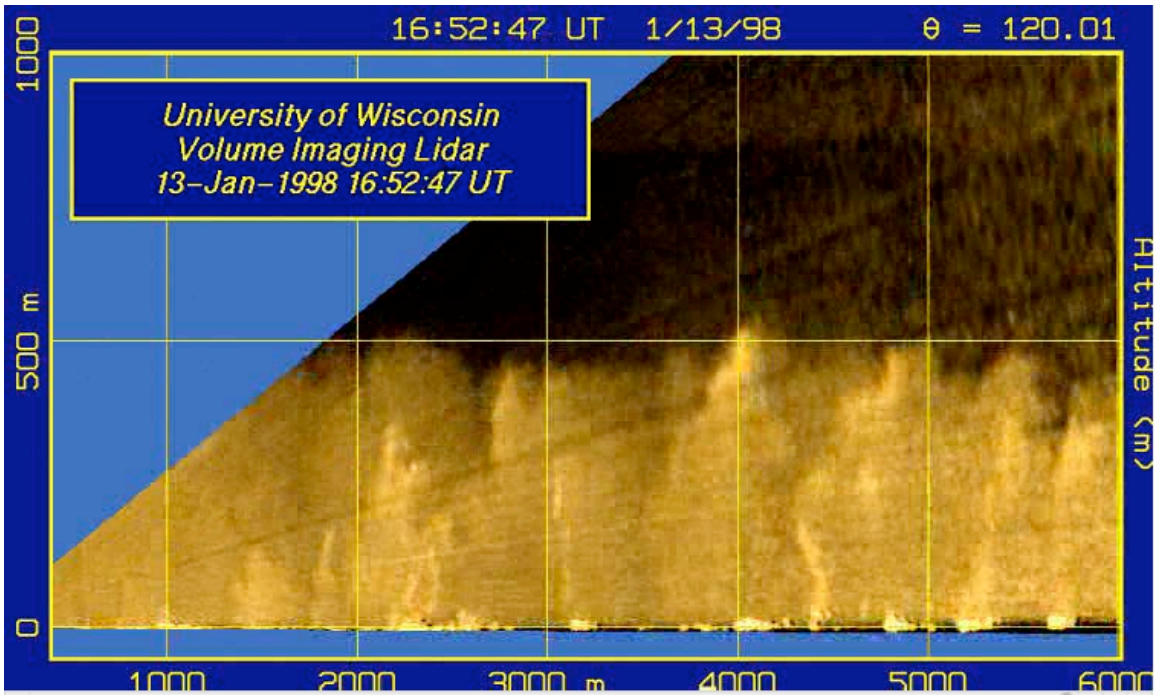

Figure 2.5: An example of a Range-Height Indicator (RHI) scan. Note that the vertical axis is elevation from ground level and the horizontal axis represents horizontal range. This particular image is from 13 January 1998.

During the Lake-ICE experiments, three main scan patterns were utilized. The first of these was a Range-Height Indicator (RHI) type scan (figure 2.5). In an RHI, the azimuth angle is held constant, and the elevation angle is changed, resulting in an image of a vertical slice of the atmosphere. This type of scan is very useful for looking at vertical structures such as eddies and convective plumes, as well as for looking at the vertical structure of the boundary layer.

A second type of scan involves taking several RHI scans, and changing the azimuth angle after each one, resulting in a volume scan. This type of scan is known as an RHI Volume scan (figure 2.6). These scans present a good picture of both the vertical and horizontal structure of the atmospheric aerosol structure. One drawback of this type of

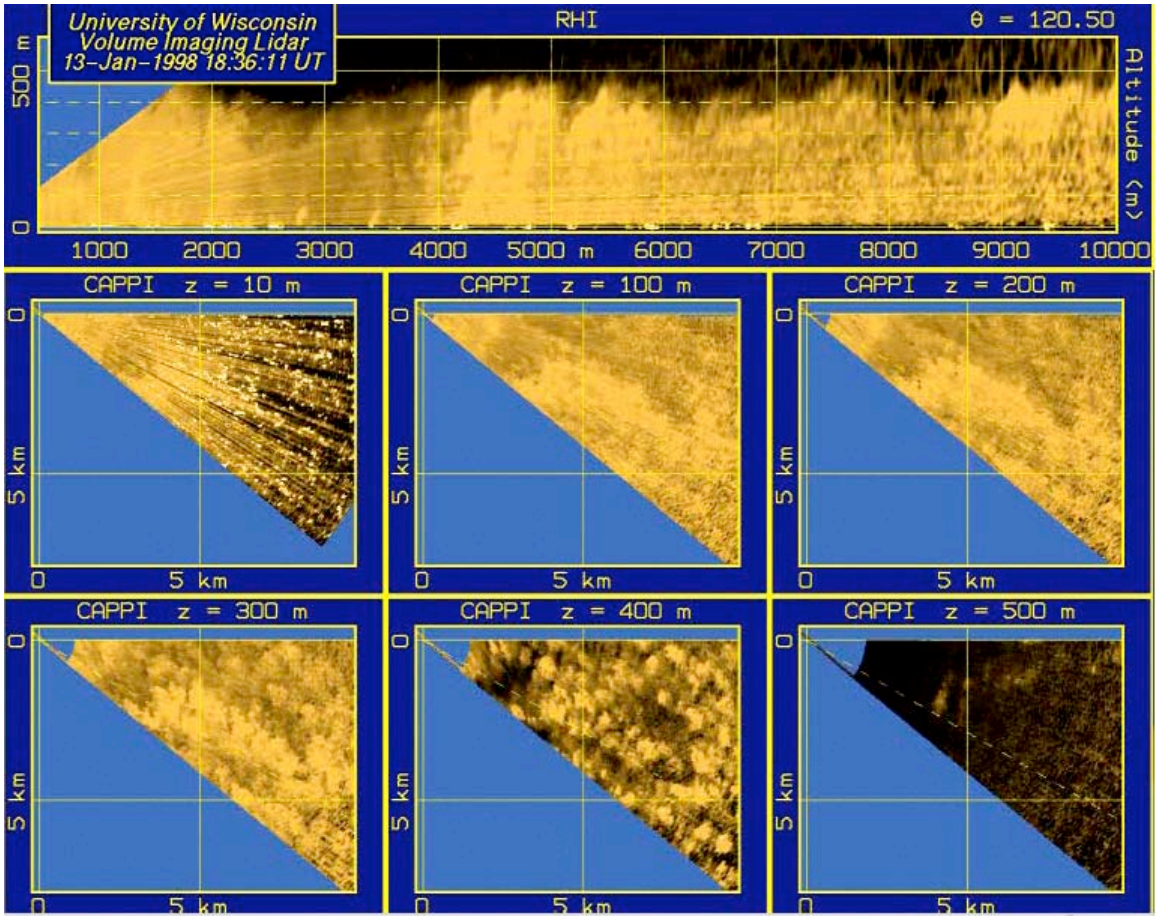

Figure 2.6: An example of Range-Height Indicator (RHI) volume scan imagery. Note that in the top image, the vertical axis is elevation from ground level and the horizontal axis represents horizontal range, similar to an RHI. The bottom images show constant altitude plane-parallel indicator (CAPPI) scans at six elevations. This particular image is from 13 January 1998.

scan is that they take significantly more time to complete than normal RHI scans. Because of this, the temporal resolution of specific structures is reduced.

The third type of scan utilized during Lake-ICE was a plane-parallel indicator (PPI) scan (figure 2.7). This type of scan involves holding the elevation angle constant, while changing the azimuthal angle, resulting in a constant altitude planar image of the aerosol structure. These images are still at a non-zero angle relative to the ground however, since the beam must always be pointed slightly upward. Because of this, constant altitude PPIs

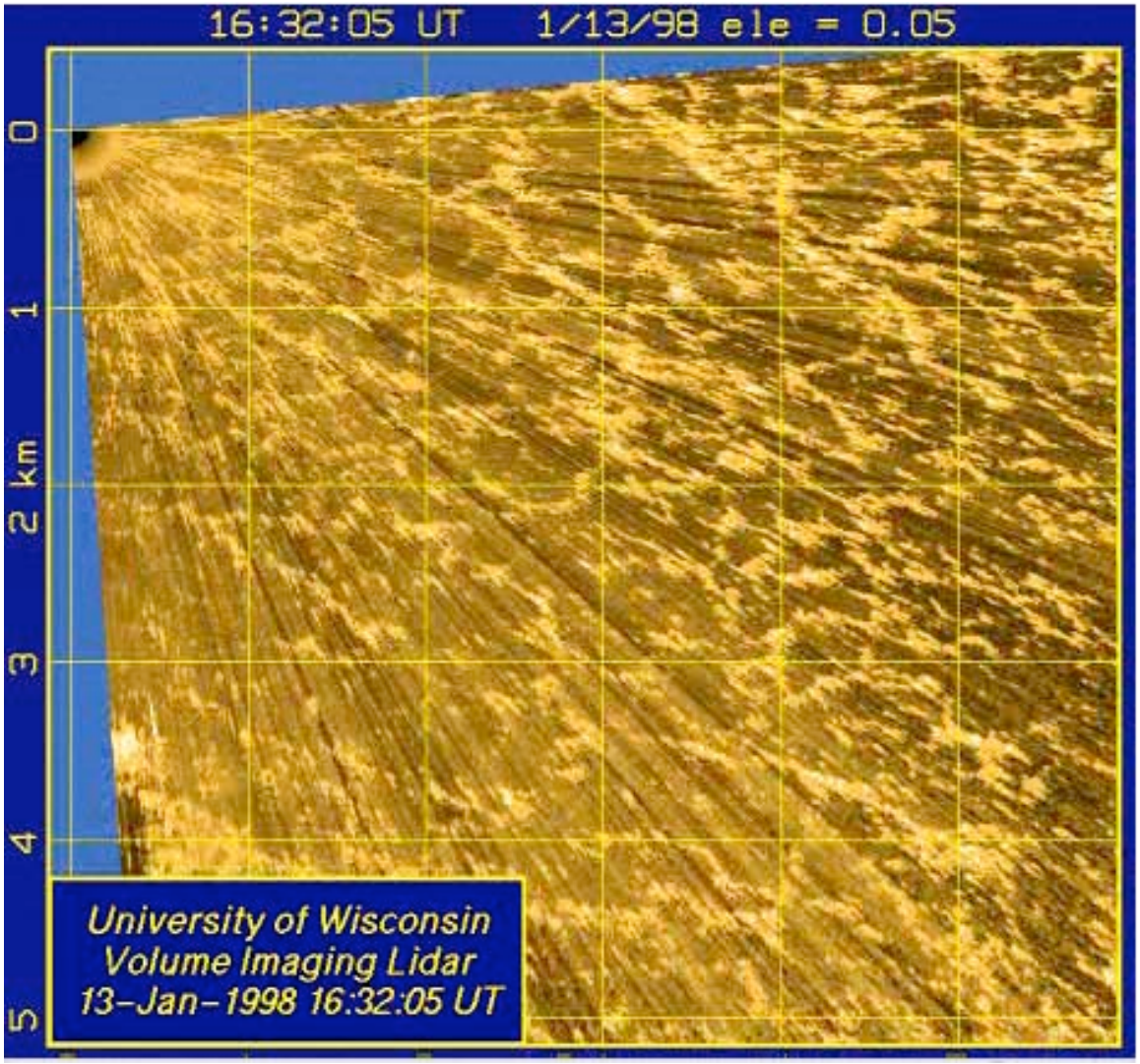

Figure 2.7: An example of a Plane-Parallel Indicator (PPI) scan. Note that the vertical axis and horizontal axis represent horizontal range, with the top left being the position of the lidar system. This particular image is from 13 January 1998.

(CAPPI) are produced through interpolation of the RHI volume scans. This scan pattern is particularly useful when investigating a mainly horizontal phenomenon.

Since the land breeze has significant features both horizontally and vertically, all of these scan patterns were utilized on 21 December. More information on the types of scans used is presented in chapter three.

Chapter 3

Lake-Induced Convection Experiment (Lake-ICE) Observations

3.1 The Lake-Induced Convection Experiment (Lake-ICE)

During the winter of 1997 and 1998, a large-scale field study occurred around Lake Michigan, in the Midwestern United States. This experiment, known as the Lake-Induced Convection Experiment (Lake-ICE) (Kristovich, et al. 2000), had as its primary objective gaining a better understanding of the meso-γ-scale and micro-γ-scale convective circulations taking place over a warm lake surface during cold air outbreaks. Additionally, an effort was made to better understand the interactions between these two scales, as well as to understand the processes by which these circulations aided in the formation of atmospheric circulations at the meso-β and meso-α-scales, such as lake enhanced snowfall.

Due to the fact that several of the structures studied during Lake-ICE are of a much smaller scale than can be observed with traditional and established observational networks such as the NWS sounding network, a multitude of instruments were employed over and around Lake Michigan in order to capture the phenomena more accurately.

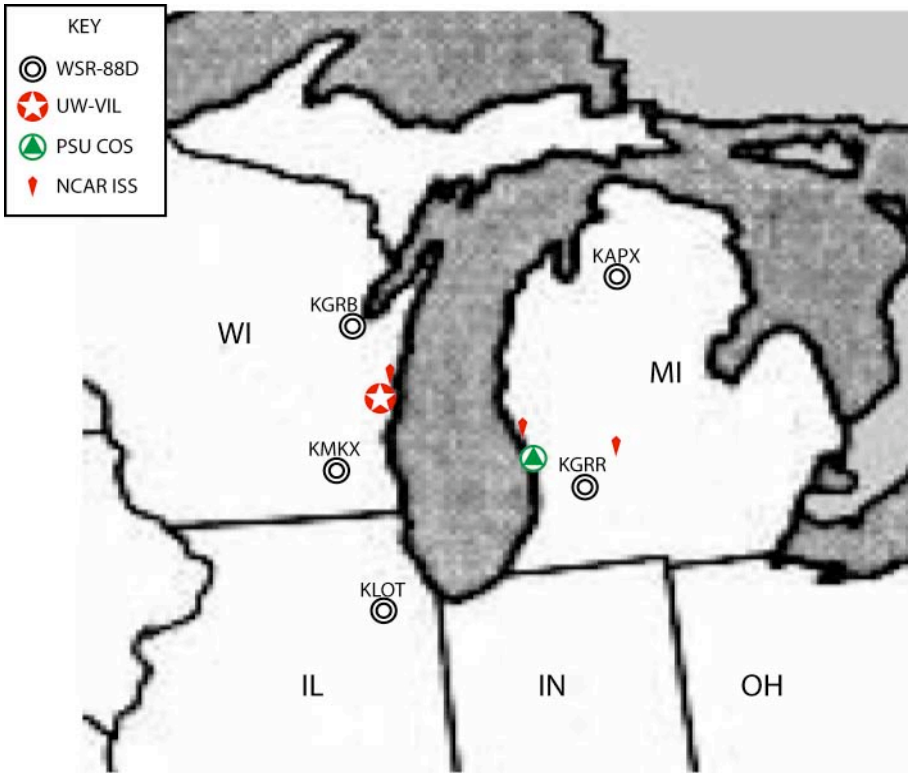

Figure 3.1: Locations of instrumentation used during Lake-ICE.

Included in this group of instruments were two research aircraft, the National Center for Atmospheric Research (NCAR) Electra aircraft and the University of Wyoming King Air, three NCAR integrated sounding systems (ISS), the Pennsylvania State University Cloud Observing System (PSU COS), and the University of Wisconsin Volume Imaging Lidar (UW-VIL). Additionally, several WSR-88D radar sites were available near the lake, including those in Green Bay and Milwaukee-Sullivan, Wisconsin, Romeoville (Chicago), Illinois, and Grand Rapids and Gaylord, Michigan. Also utilized were satellite-based Synthetic Aperture Radar (SAR) images. Figure 3.1 shows the locations of these instruments. Together, these instruments were capable of spanning several

Figure 3.2: Pictures taken around the VIL site by Shane Mayor and Ed Eloranta. The top left image is looking east from the lidar site, the top right image is of the lidar onsite, looking west, and the bottom image is looking towards the south-southeast from the lidar site.

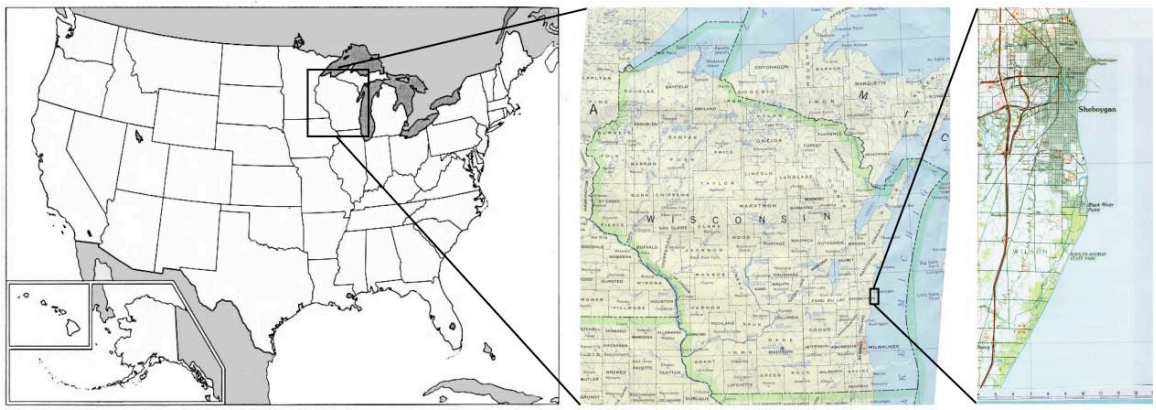

Figure 3.3: Maps indicating the location of the Sheboygan area where the UW-VIL was located. The leftmost map is of the United States, the center map of the state of Wisconsin, and the rightmost of the Sheboygan shoreline. The VIL was located on the first point above the "S" in Sheboygan on the rightmost map.

Figure 3.4: The National Data Buoy Center site in Sheboygan, Wisconsin (SGNW3).

scales of atmospheric circulations, allowing insight into the interaction between the scales.

The instrumentation utilized most for this particular study is the UW-VIL. The VIL was located at Sheboygan, WI on the western lakeshore. Figure 3.2 shows some pictures taken by Dr. Shane Mayor and Dr. Ed Eloranta from the lidar site, as well as some pictures of the lidar on site.

Figure 3.3 shows some maps of the area to get a better understanding of where the site is located. One of the nice features of this site is that there is a National Data Buoy Center (NDBC) recording station (SGNW3) within approximately one kilometer of where the lidar was located. This station, shown in figure 3.4, is located on the jetty extending out from the mouth of the Sheboygan River. Data generally available from this station include hourly wind speed, direction, gust speed, gust direction, atmospheric

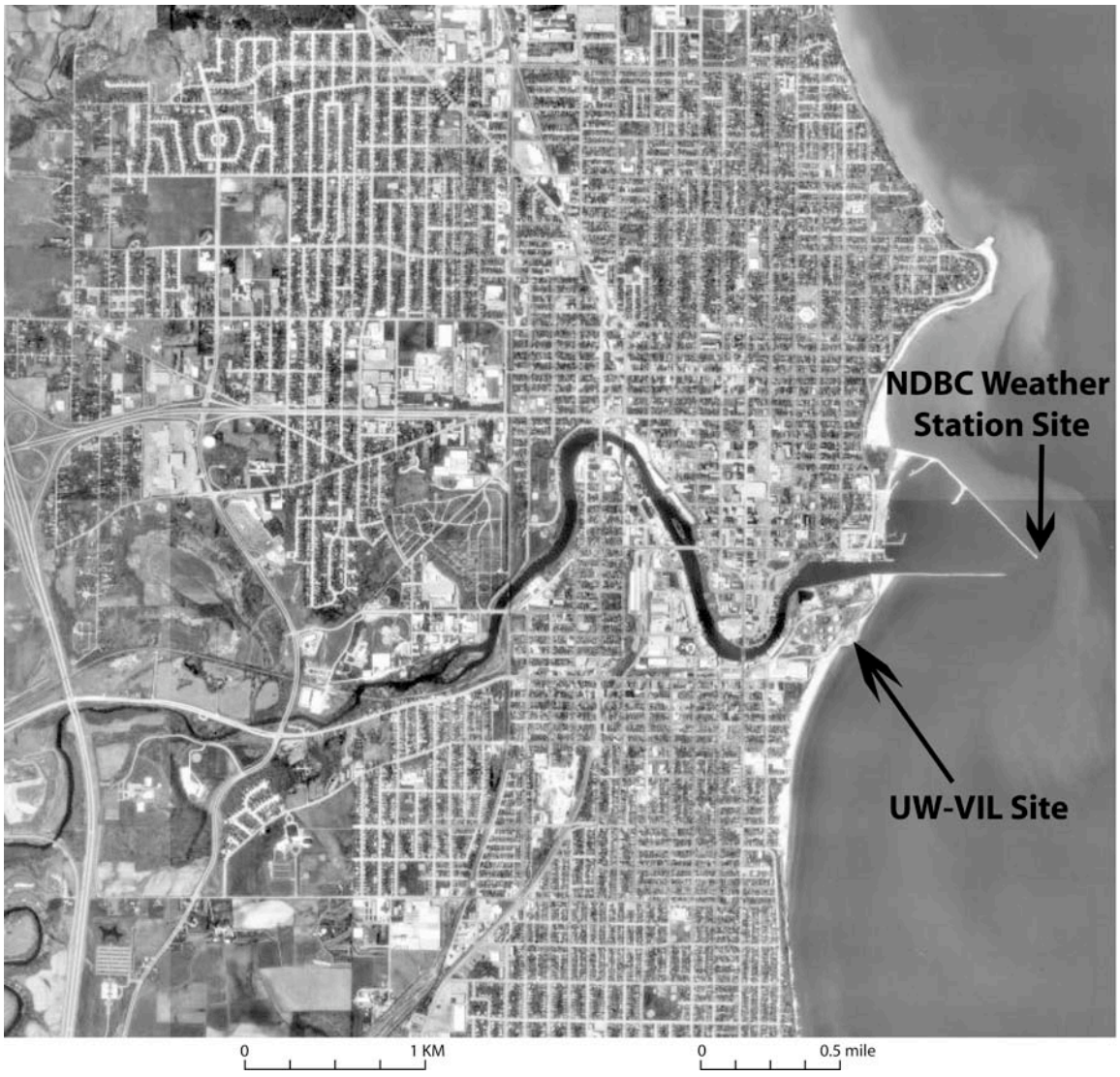

Figure 3.5: A satellite image of the Sheboygan area. Arrows indicate the locations of the UW-VIL and the NDBC weather station site. (Image courtesy of the United States Geological Survey (USGS))

pressure, air temperature, dew point temperature, and water temperature, as well as 10-minute wind data. A satellite image of the Sheboygan region, including the lidar site and the jetty containing the NDBC site is shown in figure 3.5. The area around the lidar site is industrial in nature, with buildings, smokestacks and roads. West of the city of Sheboygan, the terrain consists mostly of gently rolling hills, occupied by farmland and some slightly wooded areas. Some small towns are also located to the west, including

Kohler, Johnsonville, and Elkhart Lake. The elevation changes very little near the lakeshore, with only 100-200 m of elevation change within 100 km of Sheboygan.

3.2 21 December 1997

Late on the 20th of December, and into the morning of the 21st, an area of surface high pressure moved across the Great Lakes, into southeastern Canada. Surface winds at the lidar site gradually shifted from westerly to northwesterly, to calm, and then to northeasterly and easterly. Wind speeds were generally light, ranging from calm to 5-6 ms^{-1}. Surface temperatures ranged from around –7° C during the early morning hours, to near 0° C during the daytime hours, when prevailing winds were advecting warmer air from over the lake surface. Surface maps of the Great Lakes area for the day are shown in figures 3.6-3.8. Lake surface temperatures for the date ranged between 3-5° C, as shown in figure 3.9.

Conditions near the lidar site, taken at the NDBC site (figures 3.10 and 3.11) indicate similar trends, with surface air temperatures ranging between –3.5° C and 0° C during the land-breeze, and water temperatures hovering around 2.5° C to 3° C. In all of the NDBC data, a very apparent discontinuity shows up. This is the result of the land breeze breaking down around 16:40-17:00 GMT. This was also observed by the scientists working at the lidar site on this date, with notes from the site indicating the disappearance of the land breeze occurring at 16:40 GMT or so. Wind directions naturally do not match the larger scale, as the land breeze does not show up in the synoptic analysis. Winds at the NDBC site were mainly west northwesterly, until the breakdown of the land breeze. Wind speeds show the light nature of the flow within the

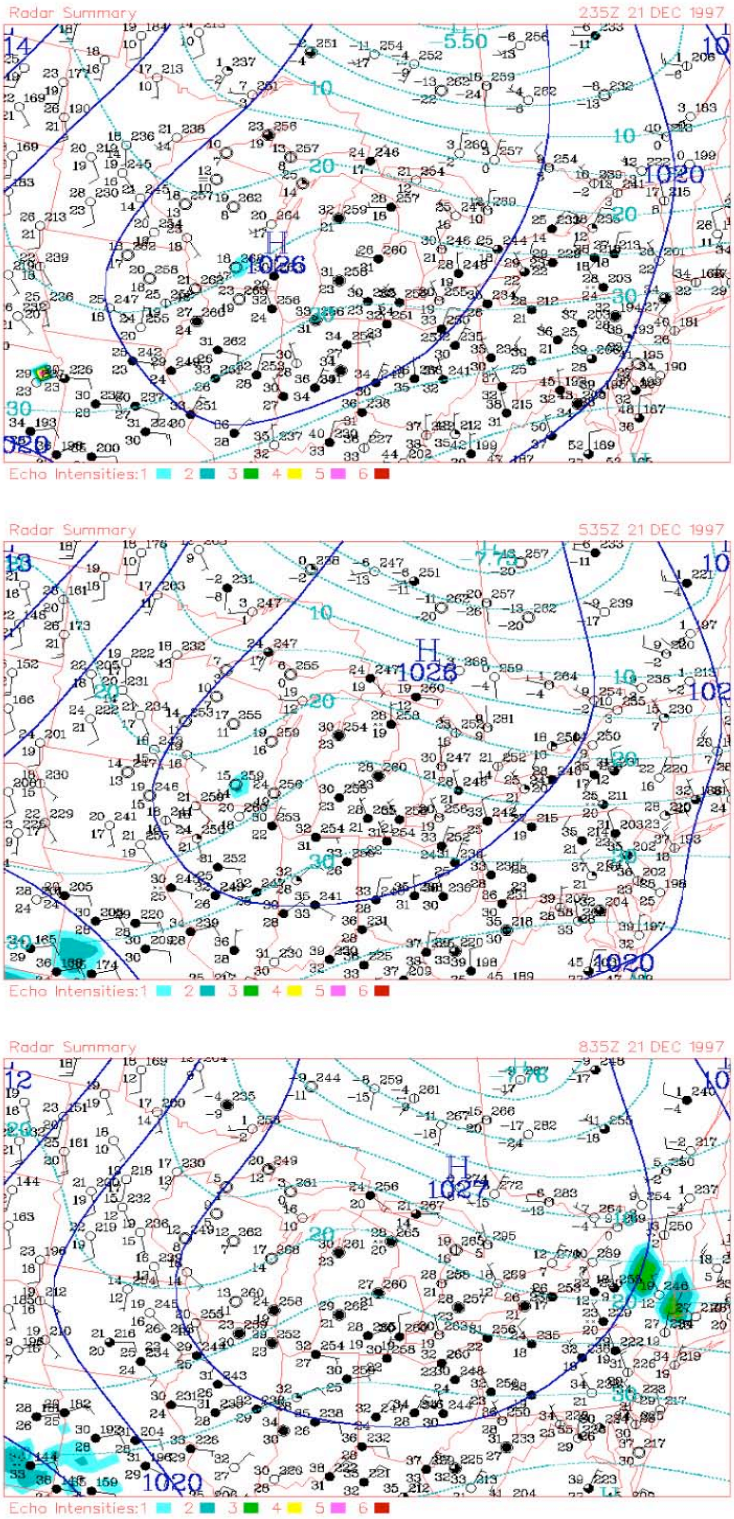

Figure 3.6: Surface data for the Great Lakes Region for 3, 6 and 9 GMT on 21 December (from top to bottom). Dark solid lines indicate isobars, with the lighter lines indicating isotherms. Station data is shown, as well as radar echoes from the date.

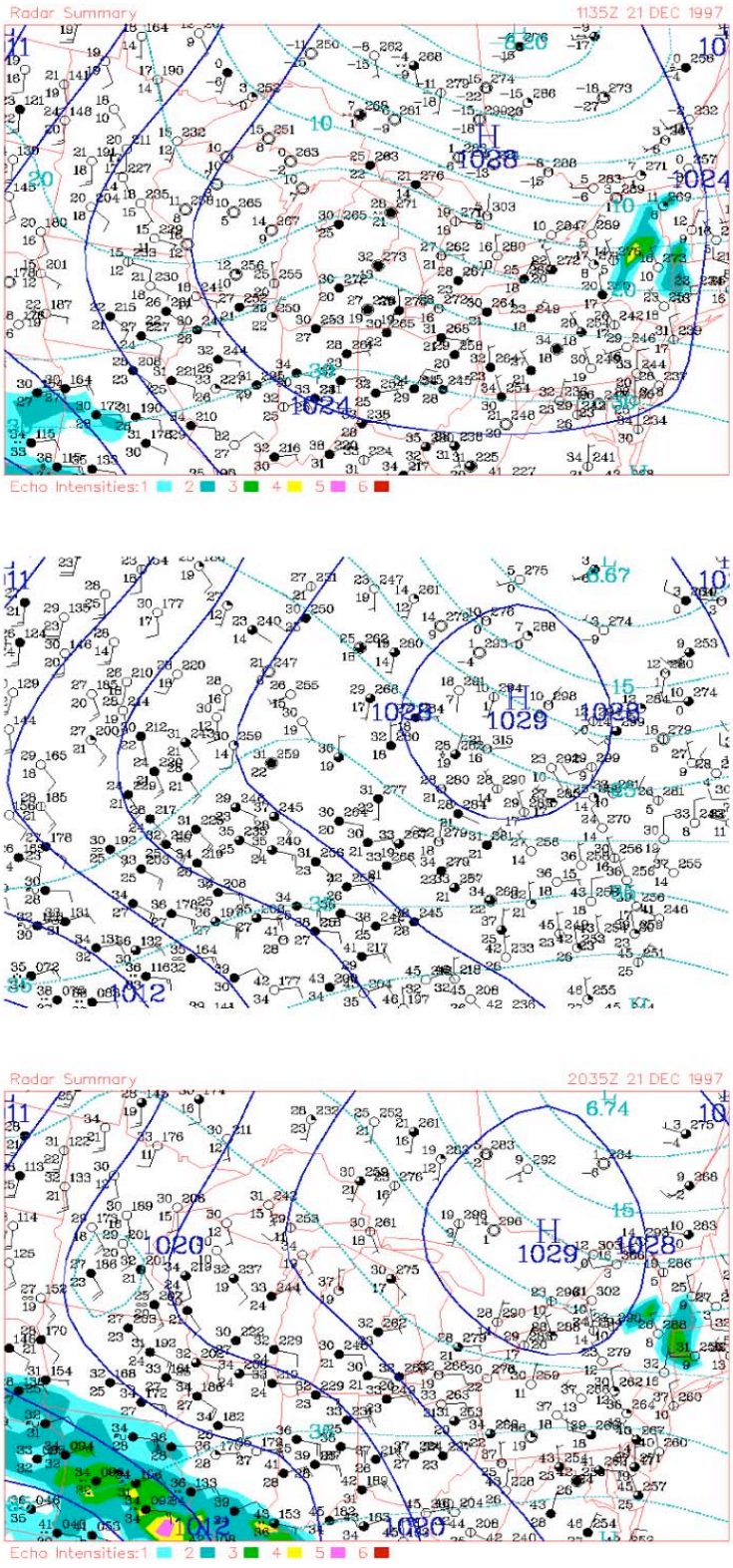

Figure 3.7: Same as figure 3.6, except for 12, 15 and 21 GMT on 21 December.

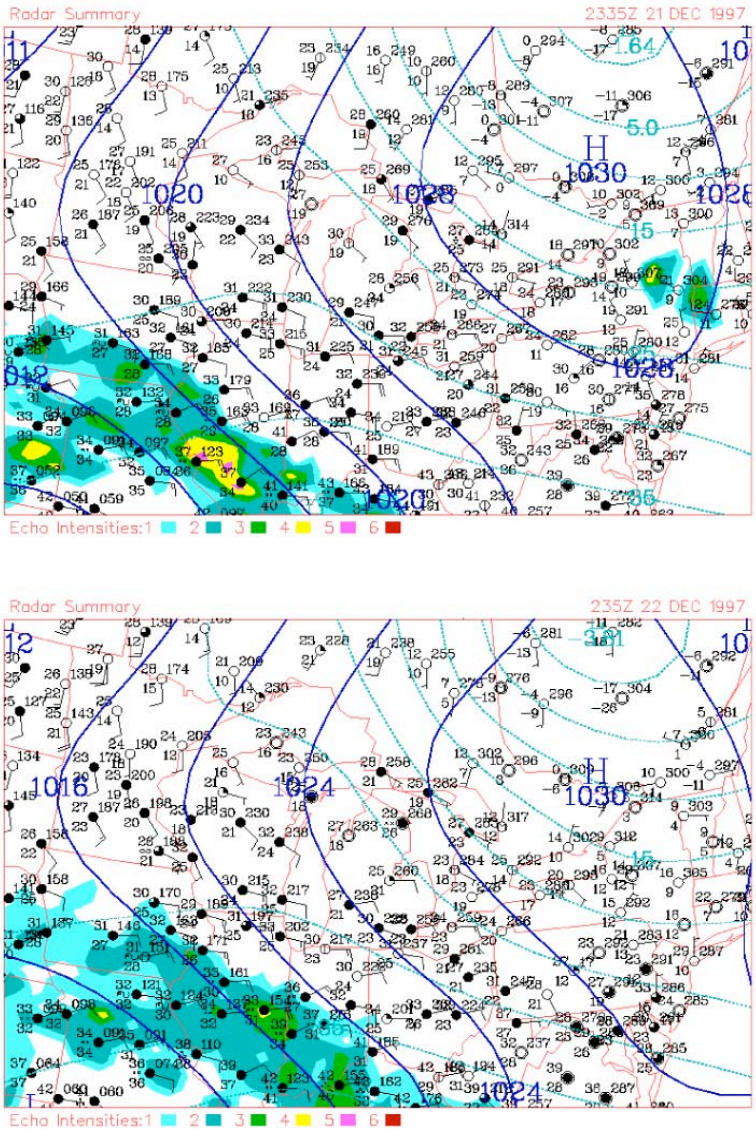

Figure 3.8: Same as figure 3.6, except for 0 and 3 GMT on 22 December.

land breeze, with velocities ranging between 1-5 ms^{-1} before the land breeze breaks down later on in the day.

VIL operations on the 21st consisted of several different data collection sessions. These are outlined in figure 3.12. The first data was collected in the form of an RHI volume scan, from 12:43 until 13:11. This scan was continued at 13:13, and carries on until 15:21 (Figure 3.13). These two scanning sessions show the land breeze shape, with

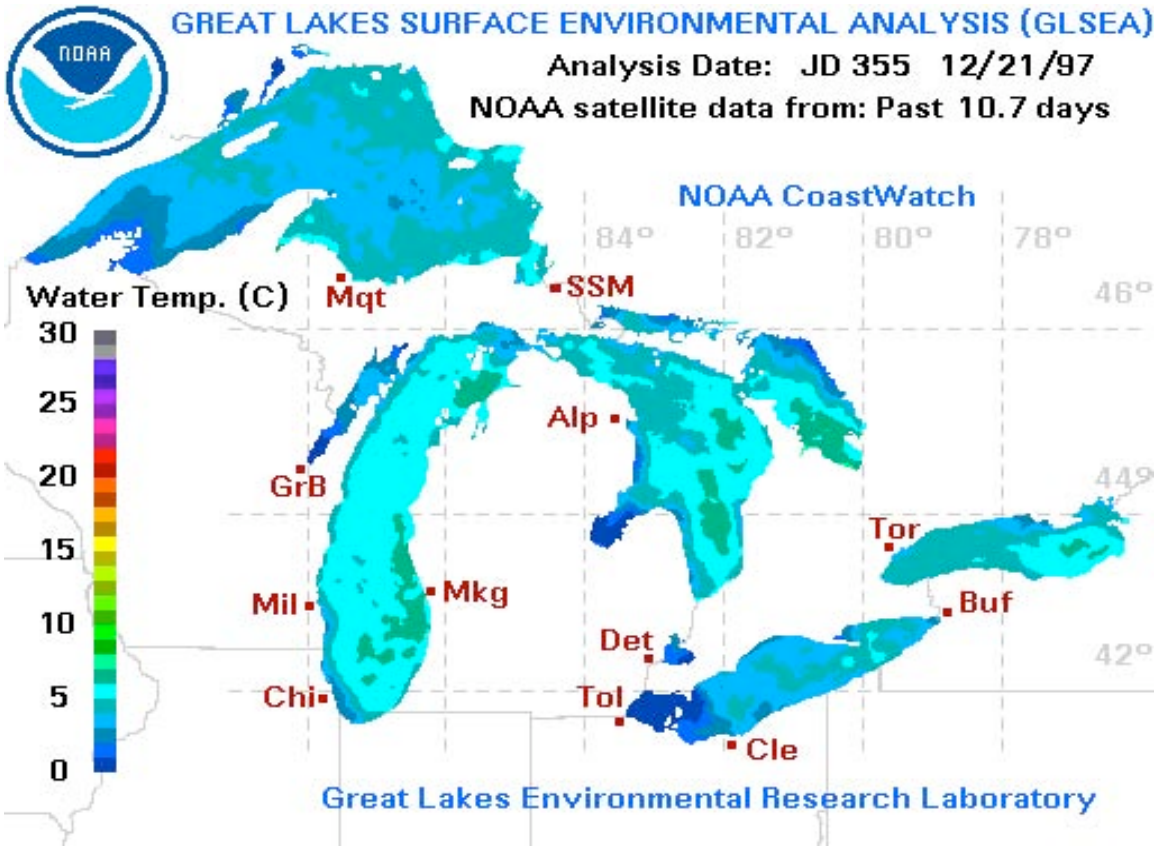

Figure 3.9: Great Lake surface temperatures, as taken from the NOAA-14 satellite. (Image courtesy of NOAA)

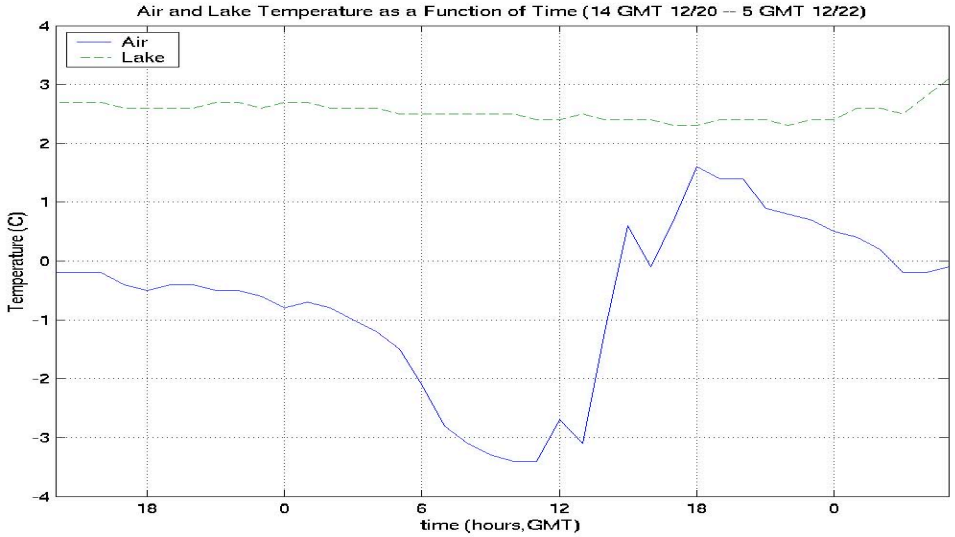

Figure 3.10: Temperature data taken at the SGNW3 NDBC site. The time scale ranges from 14 GMT 20 December to 5 GMT 22 December.

initial lidar observations showing a poorly defined land breeze flowing out to 10 km or so offshore. The land breeze shows up in the lidar data as the area of higher backscatter at the left of the images. There are two primary reasons for the increase in backscatter in the land breeze itself. The first of these is that the flow coming off of the shoreline is likely dirtier than that over the lake. That is to say, there is a higher concentration of aerosols present in this flow because of the activity in the city of Sheboygan and at the industrial sites upwind from the shoreline. The second reason is that the flow coming offshore likely has a higher relative humidity than the air flowing in off the lake when flowing offshore because of its colder temperature. Aerosols tend to swell in regions of high relative humidity, increasing the backscatter from these particles (Covert et al., 1977; Day and Malm, 2001; Fitzgerald and Hoppel, 1982).

At the start of the data session, the land breeze current is between 200-400 m deep. The fact that the flow extends so far offshore, and that it does not have a very well defined edge would seem to imply that there was very little in the form of a counter flow, whether it be synoptically forced large scale flow or the opposite shore land breeze. As the scan progresses, however, the land breeze seems to be forced back towards the shoreline, and the edge of the flow becomes much more defined. Also, the depth of the circulation decreases along with the retreat, with the land breeze only around 50-100 m deep towards the end of the scanning period. With the land breeze becoming shallower, and having to flow against the prevailing easterly winds, a nose develops at the front of the circulation. This nose shows up very well in the CAPPIs in figure 3.13 as a line of higher backscatter around the position of the intersection between the land breeze and the larger scale flow.

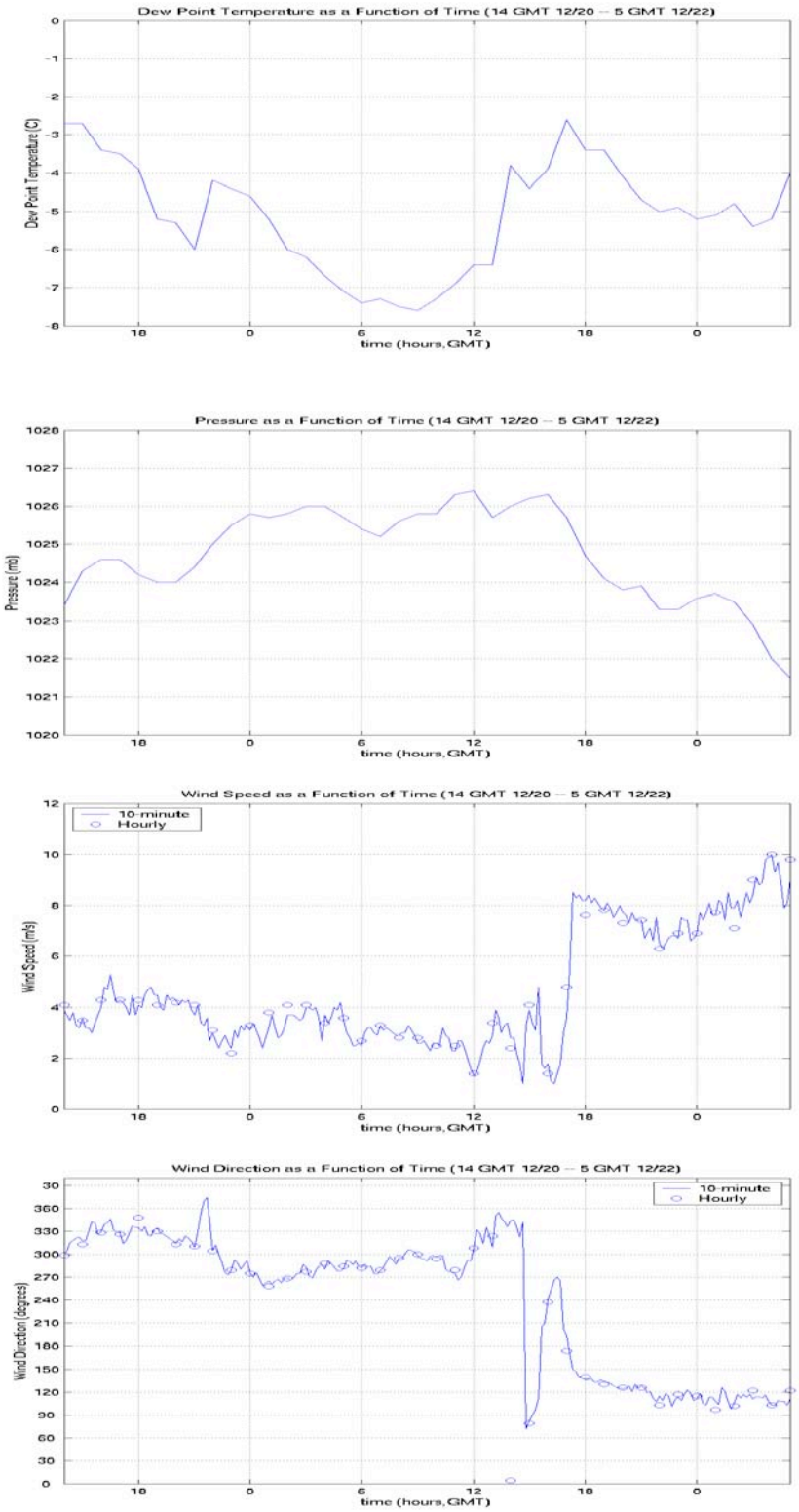

Figure 3.11: Dew point temperature, pressure, wind speed, and wind direction data taken at the SGNW3 NDBC site. The time scale ranges from 14 GMT 20 December to 5 GMT 22 December.

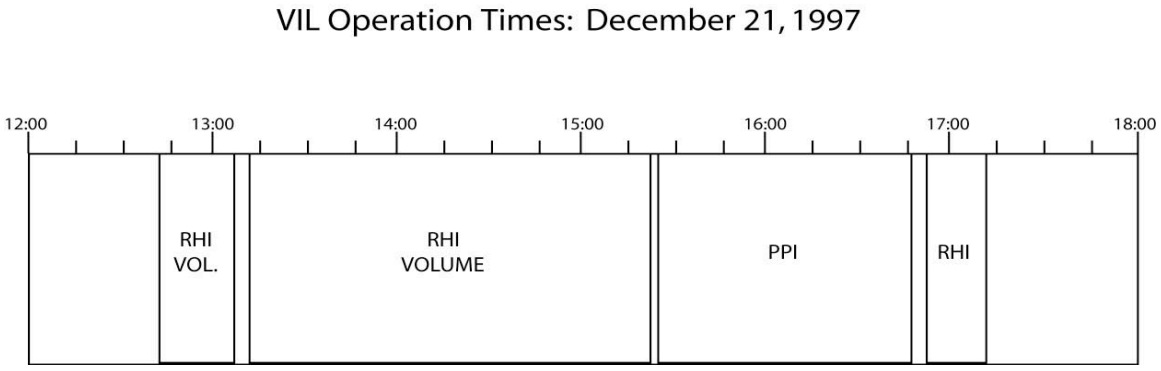

Figure 3.12: Operation periods for the VIL on 21 December 1997.

Another point of interest in these scans is the depth of the boundary layer. It appears as though the layer deepens slightly as the day starts, growing to near 800-900 meters. Also, as the day progresses, gravity waves appear along the top of the boundary layer. These waves are likely due to the convection that was taking place as the cold air from the eastern shore of the lake was advected in the westward synoptic flow over the relatively warm lake surface. Towards the end of the scanning period, clouds can be seen developing along the crests of these waves at the top of the boundary layer.

The next scanning period occurred between 15:24 and 16:46. These 0.06° elevation PPI scans, cover around 70 km^2 as shown in figures 3.14-3.15, extending 10 km west of the lidar site and around 7 km south. The lidar is located in the upper left-hand corner of these images. In these figures the land breeze can be seen very clearly as an area of increased backscatter extending around 1.5-2 km offshore. At this point in the evolution of the circulation, the land breeze has been forced very close to the shoreline and there is a very distinct interface between the land breeze and the prevailing flow. When animated, this data shows an oscillating boundary at this interface, with the land breeze battling for position against the synoptically forced onshore flow. In figure 3.15, clouds

and snowfall can be seen entering the scan area. These are associated with a weak frontal zone advancing from the southeast, which eventually overpowers the land breeze and diffuses its structure. Also noticeable are the two streaks of enhanced backscatter located inside the land breeze at around 1 and 3.25 km south of the lidar site. These are likely due to industrial activities on shore.

Another interesting scan from this time period is that shown in figure 3.16. This was taken at the same time as the top figure in figure 3.14, but has been enhanced to obtain a better view of the structure of the relatively cleaner onshore flow. In that flow some cellular type convective structures can be seen moving into the land breeze boundary from the east. These cells appear to have diameters of around 300-500 m.

The final scan period of the day was between 16:51 and 17:12 GMT. This was a 2D RHI scanning period, covering from 0° to 15° elevation (figure 3.17). At this point, the land breeze has more or less been overpowered by the front discussed earlier. There is still some eastward motion in the aerosol field right at the surface, but otherwise, everything is moving towards the west. The streaks falling from the clouds in this image are snowfall, which was documented at the lidar site. Although it may appear that the boundary layer depth has decreased significantly, this is not the case. The lidar is being blinded by the clouds at the top of the boundary layer, and what is really being observed as clean air around 650 m is more likely shadows caused by the fact that the lidar signal has been attenuated. During this scan period, scientists at the lidar site noticed an increase in the surface roughness of the water approaching the shoreline, likely caused by the stronger winds outside of the land breeze. Also, shifts in the direction were noted by blowing flags around the site, with the shift being from westerly winds to southeasterly.

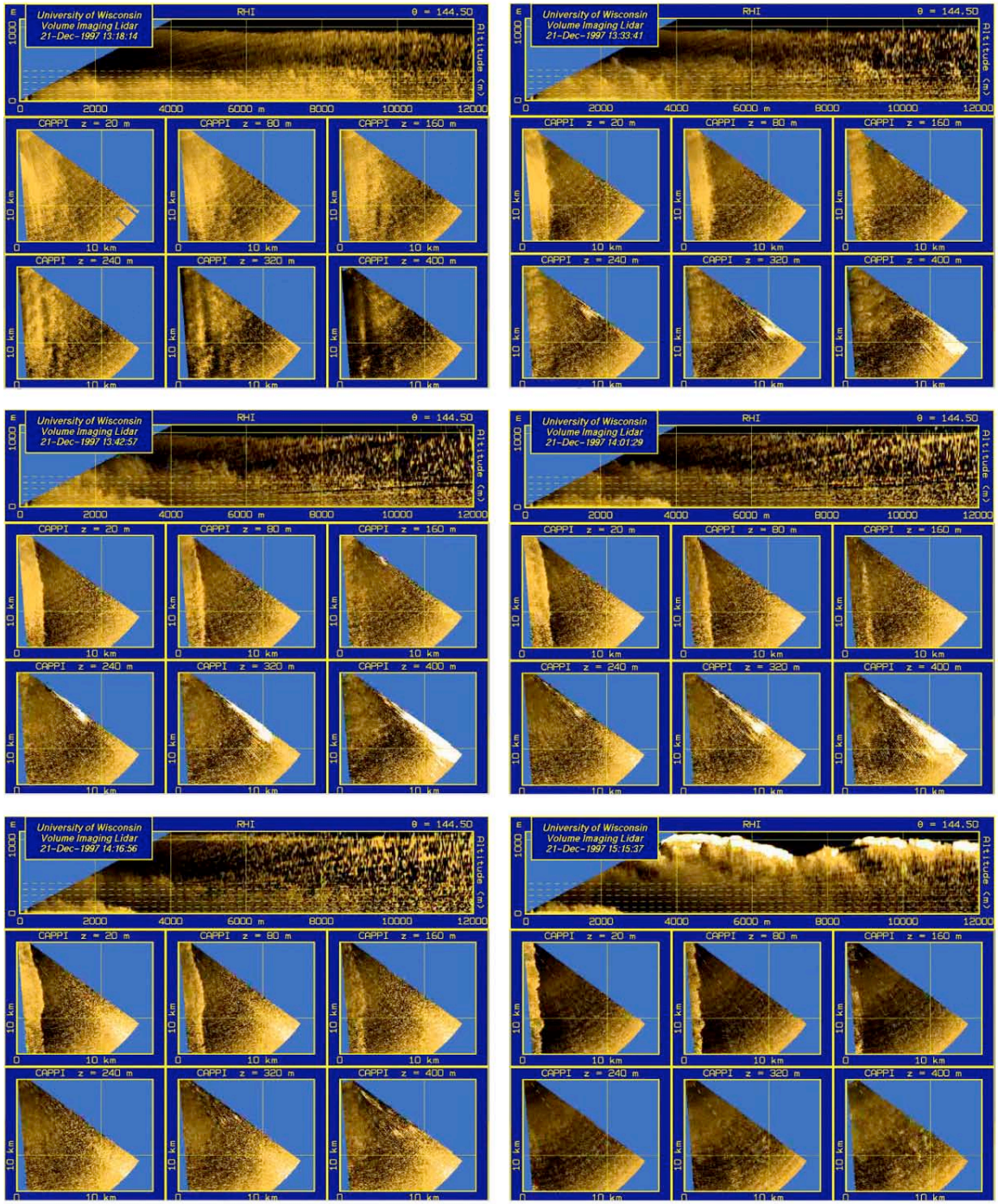

Figure 3.13: RHI volume scans from six separate times taken during the 13:12-15:21 GMT scan period. The top image in each scan is an RHI scan extending eastward over the lake, with the bottom six being CAPPIs with increasing elevation angle from top left to bottom right.

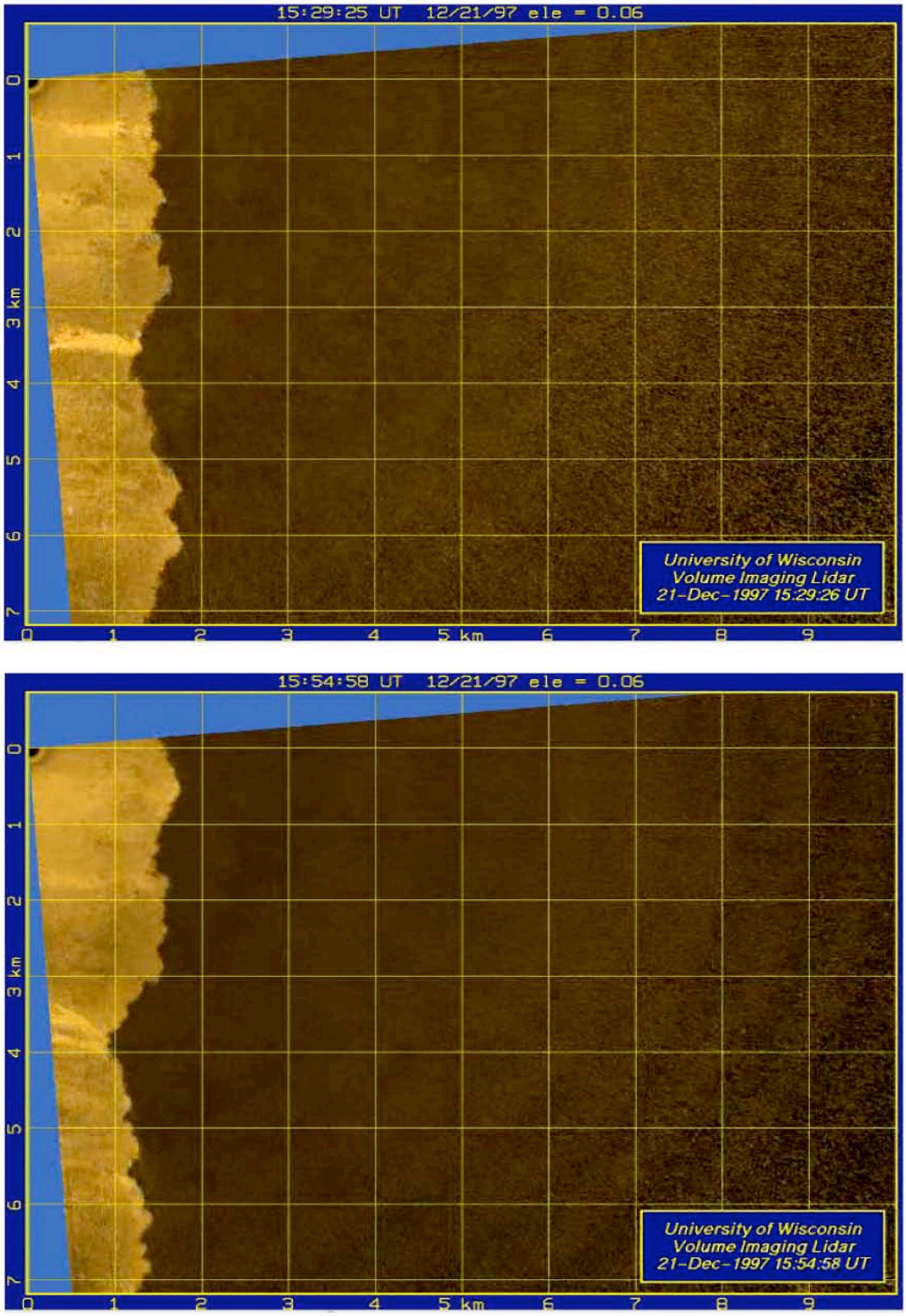

Figure 3.14: PPI scans from the 15:24-16:46 GMT scan period.

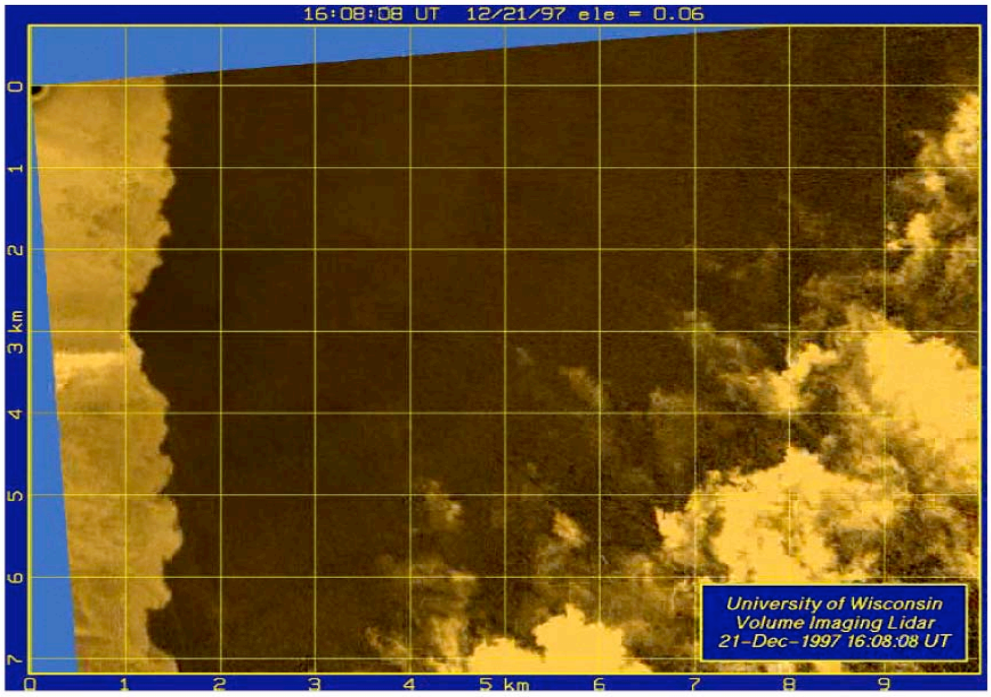

Figure 3.15: PPI scan from late in the 15:24-16:46 GMT scan period. Note the precipitation moving in from the east.

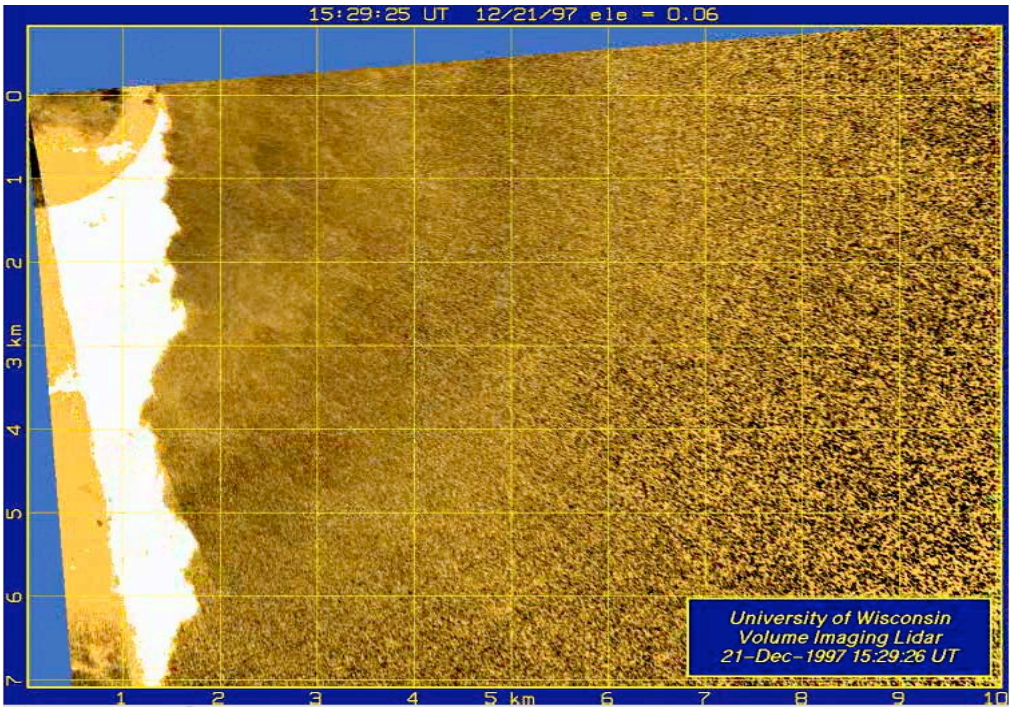

Figure 3.16: Enhanced PPI from the 15:24-16:46 GMT scan period showing the structure of the onshore flow.

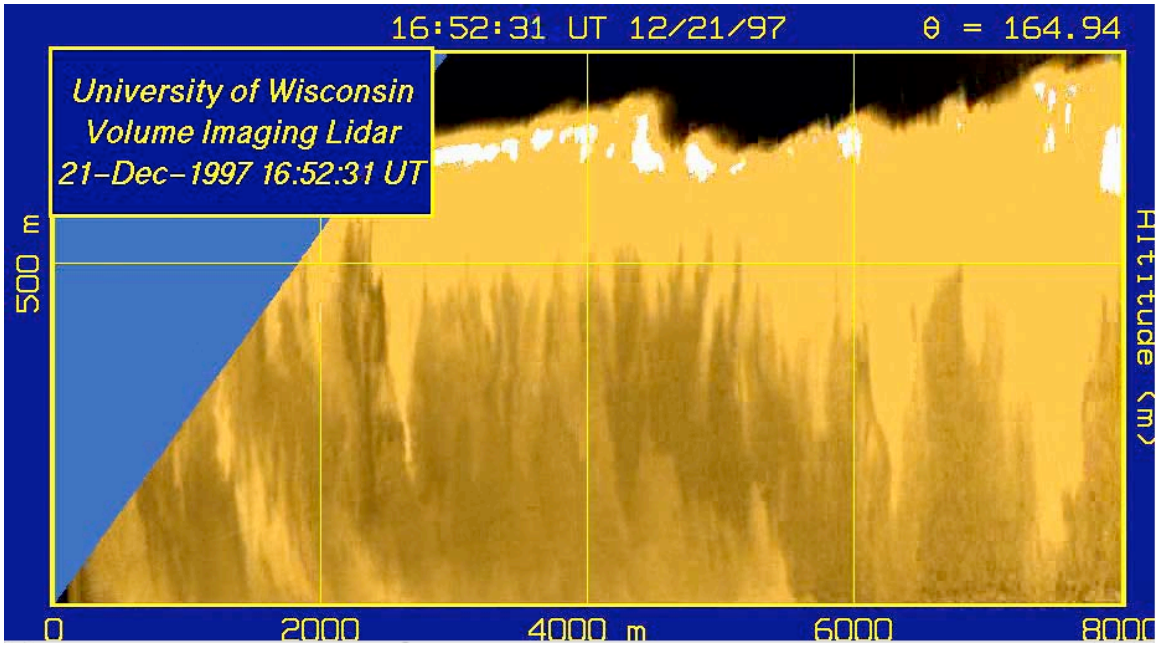

Figure 3.17: An RHI scan from the 16:51-17:12 GMT scan period. Vertical streaks are precipitation falling from low clouds at around 700 m.

Chapter 4

Land Breeze Simulations

4.1 Introduction

In order to attempt to cover the numerous scales included in the dynamics of this situation, simulations were completed utilizing the University of Wisconsin Non-Hydrostatic Modeling System (UW-NMS) (Tripoli, 1992). The model has several features that aid in the simulation of this wide range of scales. The first of these features is its two-way nesting capability. This element allows for studies of the interactions between meso-α and larger scale features with microscale features. In the case of this land breeze, the large scale is very important in terms of its structure, size, strength and formation, and these characteristics would likely not be represented accurately without the inclusion of the large scale. Naturally, it would be ideal to be able to include a very high resolution across the entire domain of a simulation. Unfortunately, today's computing resources do not allow this to be an option. Therefore, being able to increase the resolution locally aids us in including both large and smaller scale events.

In addition to the nesting capability, another important feature built into the NMS is the variably stepped topography scheme. Two popular methods of handling topography have been the terrain following coordinate system, in which the grid boxes actually take a

similar shape as the topographical features, or a stepped type topography, where a grid box is either part of the terrain or part of the atmosphere.

Although both techniques have their strong points, the terrain following coordinate system has a difficult time when representing very steep topography, and the stepped system has difficulties with very gradual slopes, since the entire grid box is filled when a grid box is considered to be terrain, essentially turning gentle terrain into a flat surface. The NMS utilizes a variably stepped topographical scheme, in which grid boxes can be partially filled based on what percentage of the grid box is in fact underground. Then, the center is adapted to be in the middle of the above ground section. Since it is a stepped technique, the ability to resolve steep terrain is maintained. However, since now grid boxes can be partially filled, subtle terrain features can now also be resolved. This becomes very important when the resolution becomes higher, and grid boxes are similar to each other in terrain height.

The NMS can be initialized from a meteorological analysis file, or can be initialized from an idealized initial condition, as commonly done in large eddy simulation (LES). Since in this study we wish to simulate features at the scale of the lidar resolution, and the observing network used for initialization is at a much coarser resolution than that required to observe these structures, some part of the simulation must be interpolated from a coarser grid.

In this chapter, results from several simulations will be discussed. The majority of simulations were run on a 4-processor Dell machine with 4 GB of memory. The main emphasis will be on a simulation (simulation 'B') run on a new dual 64-bit Opteron processor machine that utilizes 6 GB of memory, and is equipped with a RAID storage

system for holding the output from simulations. In this simulation, several of the domains were significantly increased in size, and a passive tracer was added in order to facilitate the use of a virtual scattering parameter.

One issue that remains with these simulations is the time required for simulating significant amounts of model time. For simulation 'B', fifteen seconds worth of model time needs 1.3 hours to run on the current hardware. This means that one hour of model time requires around 13 days to run, and 15 hours would take almost 200 days. Obviously this is not an acceptable time frame, and therefore, as mentioned earlier, a temporal staggering of grid implementation is employed. Even with this approach, however, simulation of the 4.5 hours of lidar observations from the 21st with six grids would require almost two months of time. Therefore, the first aspect of this study, represented by the data shown in this chapter simply includes the recreation of a land breeze of approximately the same proportions as that observed. The second aspect to be studied and discussed in chapter 5 is the timing of the size and strength adjustments observed with the lidar.

4.2 Simulation 'B'

Simulation 'B' was set up as shown in table 4.1. The set up resulted in the simulation of a land breeze, as will be discussed here. Although expected, this does show that structures not necessarily present within the initial conditions can be replicated through dynamical downscaling when forced by well-represented land surface features and their interaction with the predictable large-scale flow.

The vertical resolution for simulation "B" was set up in a stretched configuration in order to focus on the boundary layer. The first fifteen grid boxes had a constant 20-meter

Grid	Horizontal Points	Vertical Points	Horizontal Resolution (m)	Horizontal Size (km)
1	65x65	50	60000	3780x3780
2	77x77	50	12000	900x900
3	52x52	50	2400	120x120
4	197x157	50	480	93.6x74.4
5	452x362	50	160	72x57.6
6	502x502	50	32	16x16

Table 4.1: Basic description of the nested grids for simulation 'B'.

spacing. The elevation around Sheboygan point is around 200 meters, with lake level being 177 meters. Therefore, the nearest 100 or so meters above the surface are resolved at 20 meters spacing. From here, the vertical spacing is increased by 120% with each higher box, up to a maximum spacing of 750 m. This results in the top grid box being at around 16 km above sea level. Although events at this height may not directly influence processes occurring in the boundary layer, they must be incorporated in order to accurately portray synoptic forcing.

The main difference between this simulation and others in this work is the size of the inner domains. Figure 4.1 shows the grid set up for simulation 'B'. Domains 4,5 and 6 were significantly increased in size relative to previous simulations, particularly in the east west direction, while maintaining the resolutions utilized earlier on. A standard arrangement of the grids from previous simulations can be seen in table 4.2. This increase was implemented in order to allow the predominantly zonal structure of both flows to develop further, and to insure that several structure cycles could be completed inside the domain. In previous simulations where the inner domains were smaller, the land breeze had a very flat structure, with no indication of undulation along the top of the

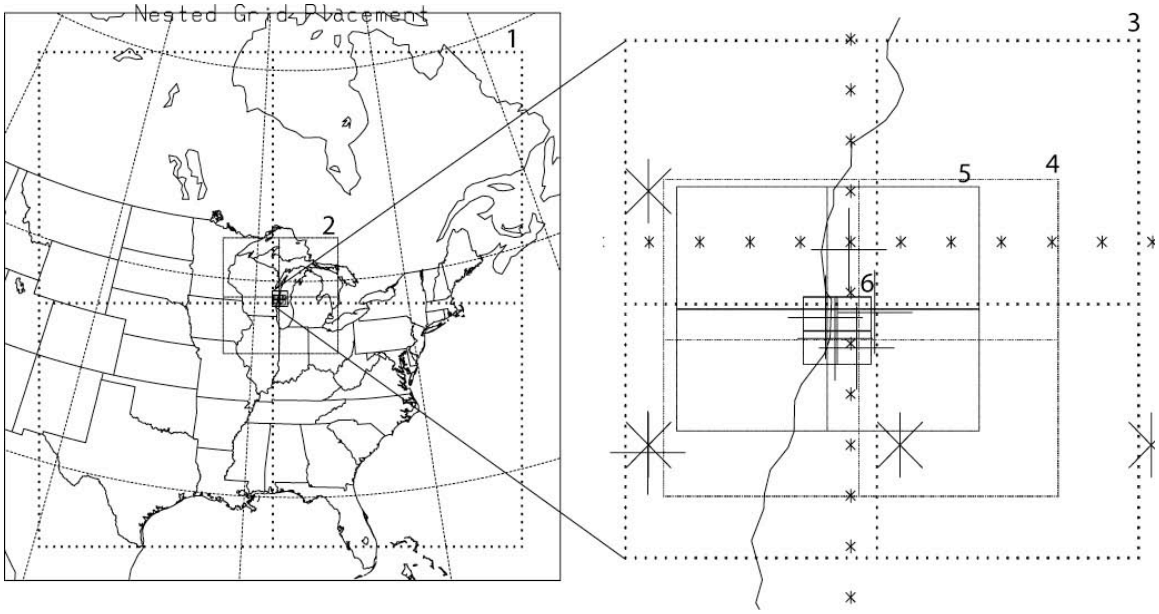

Figure 4.1: Positioning of the six nested grids in simulation 'B'. Grids 3-6 have been magnified for better viewing. Grid 3 is barely visible in the left image.

Grid	Horizontal Points	Vertical Points	Horizontal Resolution (m)	Horizontal Size (km)
1	65x65	50	60000	3780x3780
2	77x77	50	12000	900x900
3	52x52	50	2400	120x120
4	132x132	50	480	62.4x62.4
5	182x182	50	160	28.8x28.8
6	182x182	50	32	5.76x5.76

Table 4.2: Typical arrangement of the nested grids for simulations other than 'B'.

land breeze (figure 4.2). Also, the results from the inner domain would often resemble a magnified version of the next coarser domain because of a lack of mature turbulence at the resolution of the inner domain to change the flow significantly. One of the main objectives of this increase in grid size was proper formation of the structure of the onshore convective flow, since its interaction with the land breeze appears to control

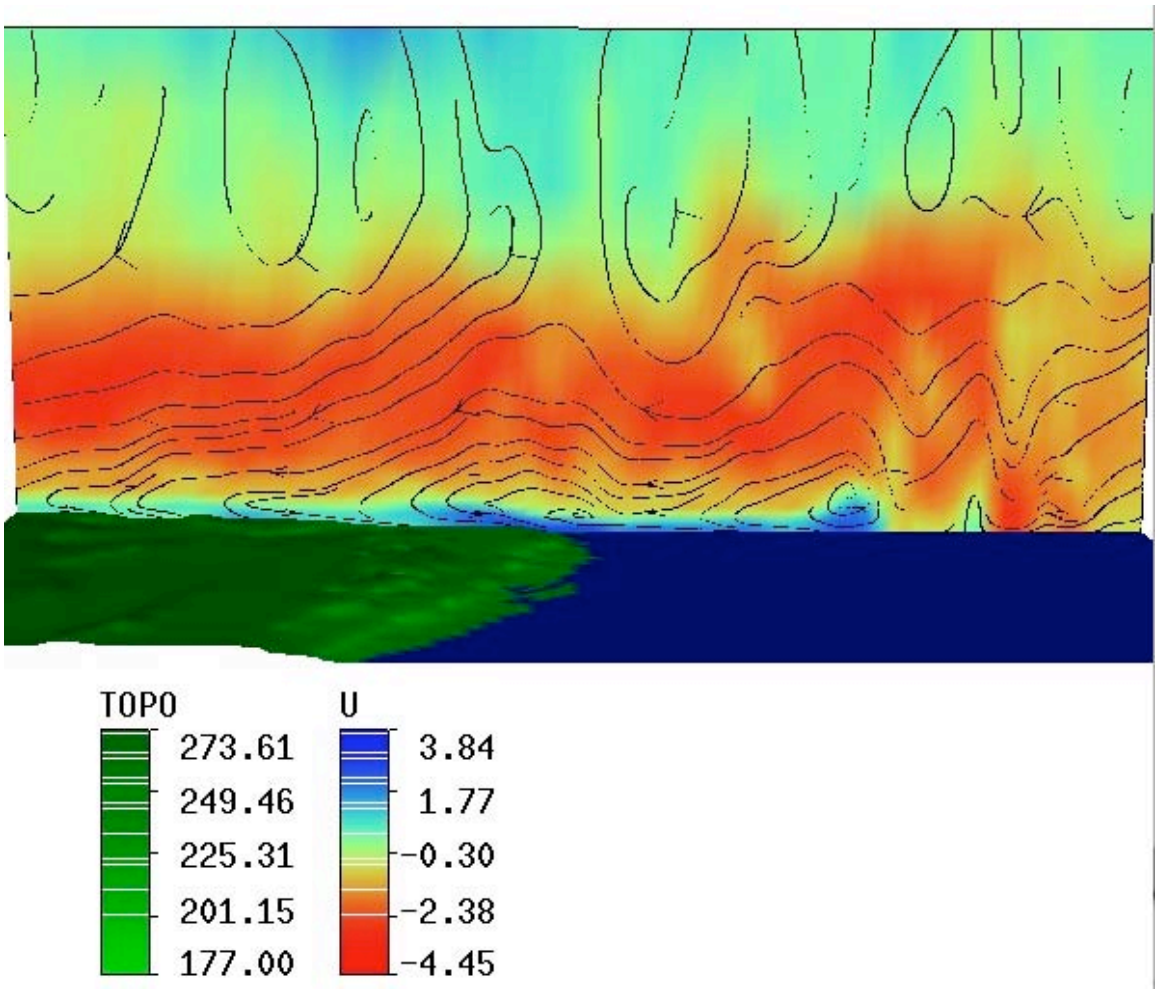

Figure 4.2: A vertical cross-section of the fifth grid of a previous simulation showing the zonal component of the wind, streamlines of the flow, and contours of topography. This is a projected three-dimensional image, with north being into the page, east towards the right of the page, and up being towards the top of the page. From lake level to the top of this plot is approximately 1.2 km. Note the flatness at the top of the land breeze.

many of the features of the land breeze head. Also unique in this simulation is the fact that the inner domain is partly over the coastline. In previous simulations, the inner grid had been placed completely offshore due to issues with momentum transfer at the nesting boundaries over topography. The unrealistic plumes that formed as a result of these issues would propagate through the domain, distorting the flow. This issue has been resolved and is discussed in the appendix.

This simulation was initialized using an ECMWF 00Z analysis from December 21. Additionally, a high-resolution topographical data set is utilized in order to capture the shoreline and topographical features affecting the flow as accurately as possible. The dataset used for the Wisconsin portion of the topography, in which the high-resolution, innermost grids are located, includes 100 m topographical resolution. Use of this data set did require some adjustment to the routine that determines the location of the shoreline in order to accurately represent the shore, since it was set up to determine the coastline at coarser resolution than that being implemented in the simulation.

4.2.1 Synoptic Features

Since the successful simulation of this land breeze circulation involves correctly forecasting the synoptic conditions for the day, some emphasis must be placed on the model's ability to correctly forecast the location and approximate intensity of large-scale pressure systems.

Looking at the actual analysis from 1200Z on 21 December (figure 4.3), two main surface synoptic systems appear to be influencing conditions over Lake Michigan. The first of these is a large anticyclone over southeastern Canada. The second is an area of low pressure located over northeastern Texas. The significance of these systems has previously been discussed in chapter 3, and will not be reviewed here. The UW-NMS appears to reasonably capture the locations and strengths of these two systems. Figure 4.4 shows the UW-NMS forecasted synoptic situation for approximately the same time as the above analyses. The intensities of the systems in the model appear to match the intensities given in the analysis, with the low-pressure system having a central pressure of 1003 mb and the high-pressure system being at 1029 mb. The locations

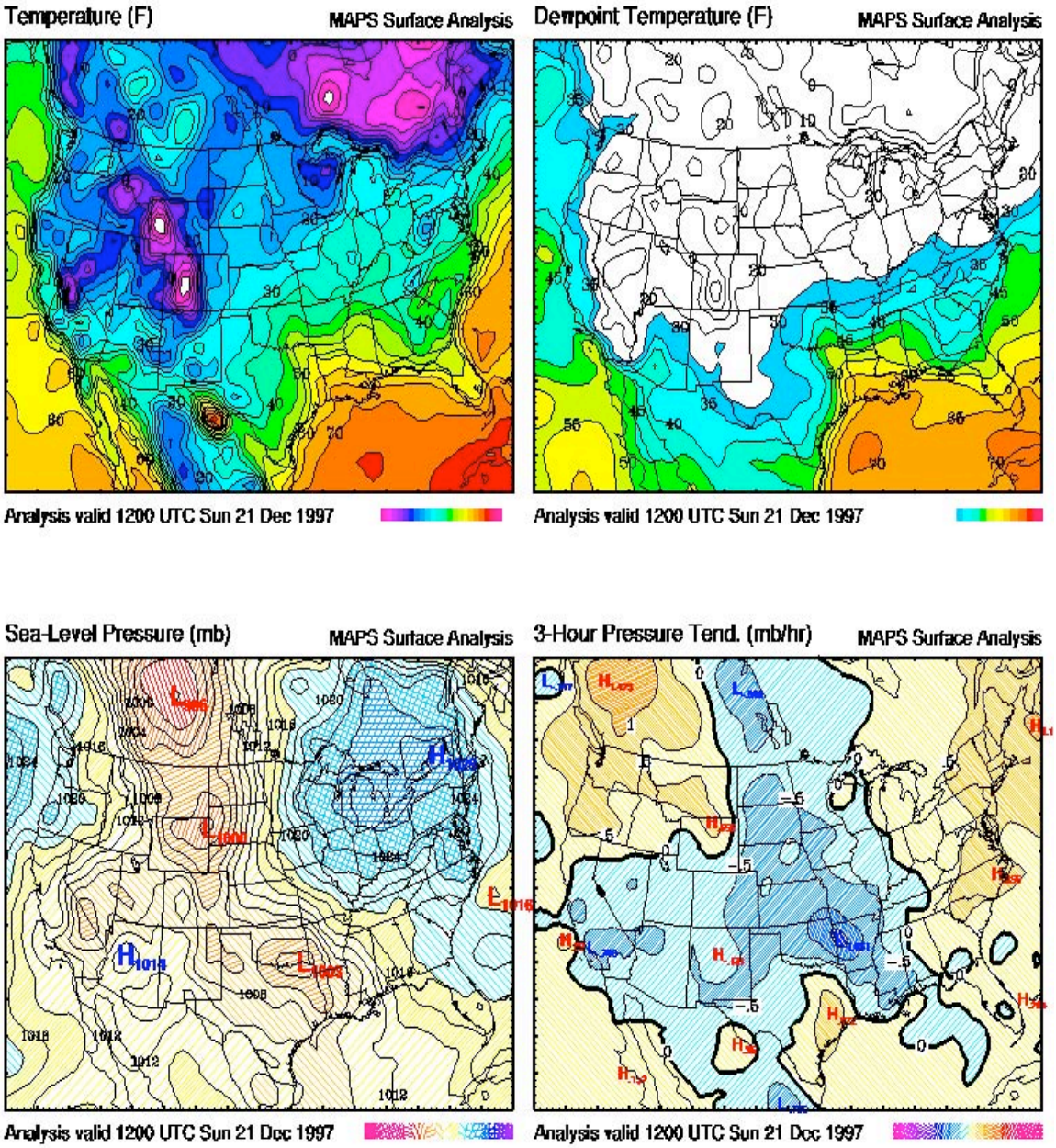

Figure 4.3: The surface synoptic analysis for 1200Z, 21 December 1997. Clockwise, from the upper left are temperature, dew point, pressure tendency and sea level pressure maps.

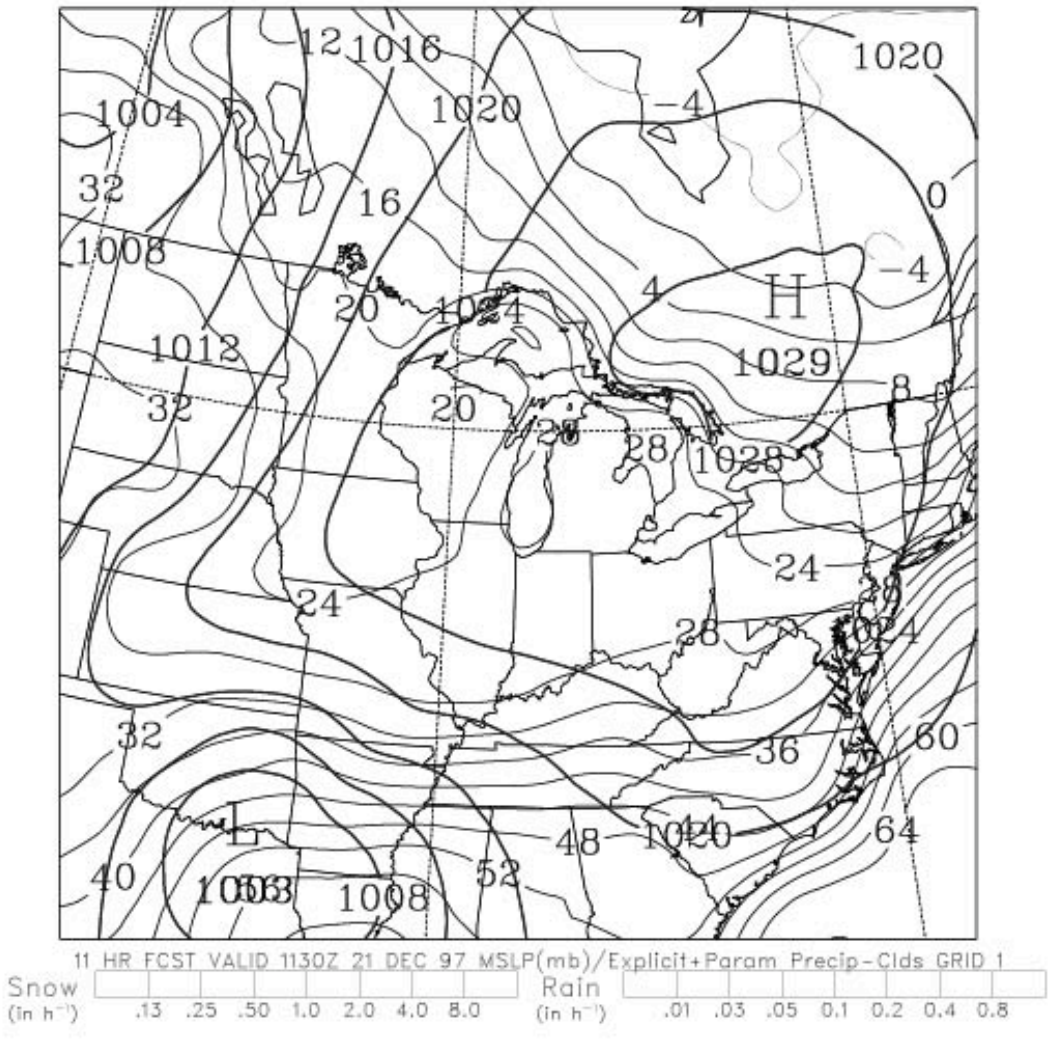

Figure 4.4: The NMS forecast for the synoptic forecast at 1100Z on 21 December.

match the analysis well. These two similarities should lead to similar synoptic conditions over the forecast area for this relatively small time period. It is of vital importance, however, to remember that miniscule errors at this scale can have devastating consequences at the microscale. Comparisons between the actual conditions and the model output at the microscale will be discussed in chapter 5.

One noticeable feature present in the simulations is an enhanced area of low pressure

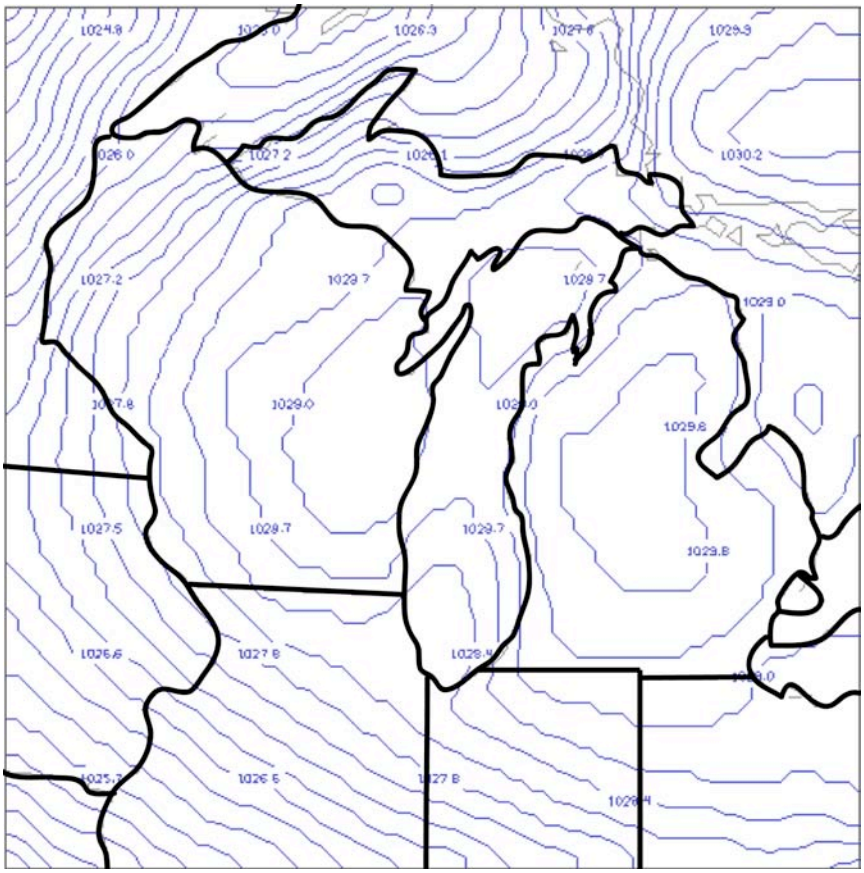

Figure 4.5: Surface pressure analysis (contoured at 0.3 mb increments) from the 2nd model domain. Note the lower pressure developing over southern portion of Lake Michigan.

over southern Lake Michigan (figure 4.5). Similar features have been discussed by Petterssen and Calabrese (1959), as well as by Schoenberger (1986). In this case, the continual warming of the air overlying the lake surface, together with radiational cooling over Wisconsin during the nighttime hours allow this shore perpendicular pressure gradient to set up a very favorable situation for the formation of a land breeze. A similar feature is noticeable over Lower Michigan, with a closed off area of high pressure over the peninsula, and lower pressure over lakes Michigan and Huron.

4.2.2 The Land Breeze

In simulation "B", the size of the sixth grid is comparable to that of the fifth grid in previous simulations, and the fifth grid is similar in size to the fourth grid in previous simulations. The increased grid size allows the entire land breeze to be captured inside the 5th grid. This can be seen in the zonal velocity data (figure 4.6).

The land breeze is clearly visible in figure 4.6 right along the shoreline, especially at the lower levels. The strongest portion of the land breeze appears to be the offshore portion, with the flow accelerating with the reduced frictional force over the water surface. Looking at the higher elevations, the return flow of the land breeze circulation presents itself, as there are stronger winds directly over the shoreline when compared with the over water and inland flow at the same elevation, especially at 573 m above the lake level.

Another prevalent feature in this data is the presence of the wave structure behind the head of the circulation. These undulations may be Kelvin-Helmholtz type waves forming downwind from the land breeze front, which is acting as a lifting mechanism for the onshore flow. Similar Kelvin-Helmholtz billows were discovered to form as a result of the sea/land breeze circulation by Sha et al. (1991). These features are most noticeable at 73 and 113 m above lake level, as there appears to be a break in the eastward flow right over the shoreline, possibly the result of a low point in the stationary wave pattern present at the top of the land breeze allowing the return flow to get to these lower altitudes and intrude into the center of the land breeze.

Also interesting to note about this feature is that the strongest evidence of this wavelike structure apparently shows up at the same latitudes as the strongest offshore

flow in the land breeze. This implies that there may be a connection between the amplitude of the wave and the strength of the flow creating the head of the land breeze. Physically, this would make some sense, since an increased offshore flow, assuming continuity, would cause a semi-permanent offshore frontal piling up of mass at the head of the circulation, leading to a taller head. This would, in turn, create a larger obstacle for the prevailing flow to have to pass, essentially increasing the steepness of the ramp, resulting in a larger amplitude wave in the wake of the head. Model output shows that this is in fact the case, with the tallest regions of the land breeze at the frontal zone occurring at the horizontal velocity streaks.

The vertical velocity data (figure 4.7) also reveals wind parallel structures, along with the perpendicular structures discussed above. There is a very clear convergence zone present at the intersection of the land breeze and the prevailing easterly flow around 4-5 km offshore, marked by an area of relatively stronger upward vertical motion. East of this line, there is an organized cellular convective pattern, while to the west, there is very little vertical motion, with the exception of the above noted phenomena. This is likely due in part to the stability introduced to the layer by the cold airflow of the land breeze. Of the layers shown, only 750 m above lake level shows any significant vertical motion over the shoreline, and this is likely the result of the convective layer to the east of the front being incorporated into the return flow aloft.

Some interesting features exist in the relative humidity fields (figure 4.8) as well. The first of these is that the land breeze appears to have higher relative humidity levels than the prevailing easterly flow, despite the fact that the land breeze is coming off of the dry land surface and the prevailing flow has just crossed over a very large moisture

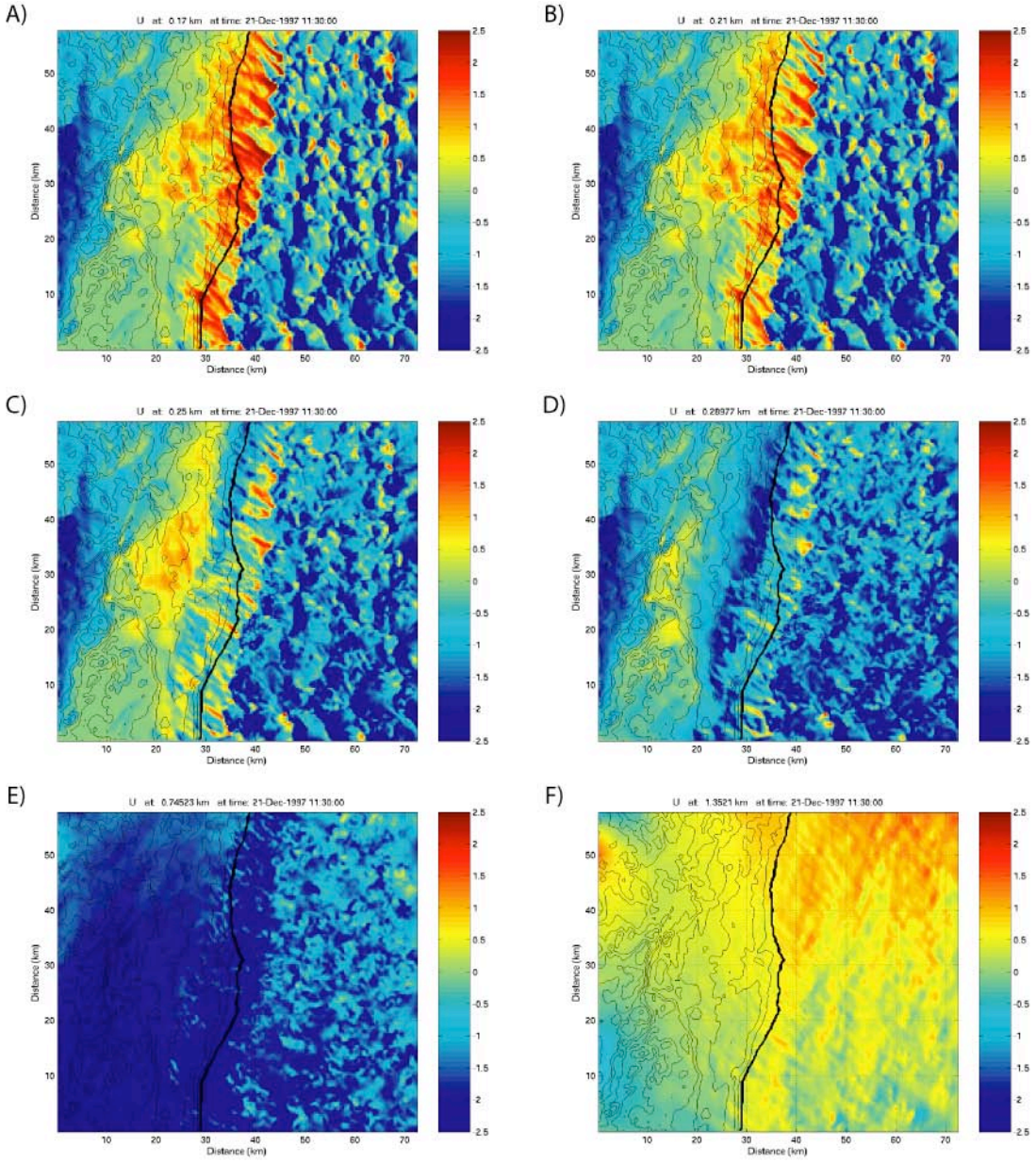

Figure 4.6: Simulation "B" grid 5 output for the zonal velocity component at the surface (A), 33 m above lake level (B), 73 m above lake level (C), 113 m above lake level (D), 573 m above lake level (E), and 1173 m above lake level (F). Topography is contoured in black. (Note: elevations stated in plot headings are absolute, and not from lake-level)

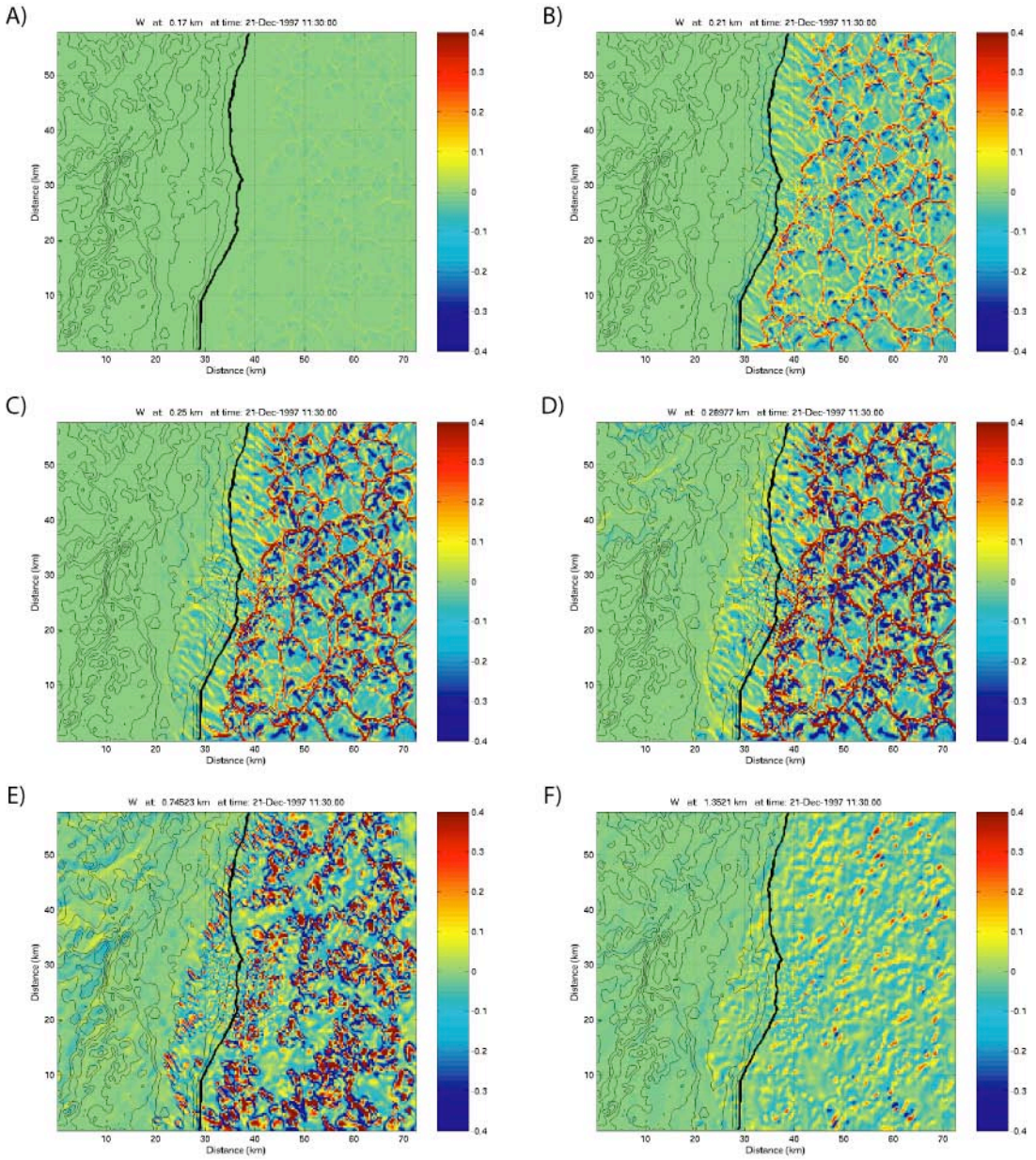

Figure 4.7: Simulation "B" grid 5 output for the vertical velocity component at the surface (A), 33 m above lake level (B), 73 m above lake level (C), 113 m above lake level (D), 573 m above lake level (E), and 1173 m above lake level (F). Topography is contoured in black. (Note: elevations stated in plot headings are absolute, and not from lake-level)

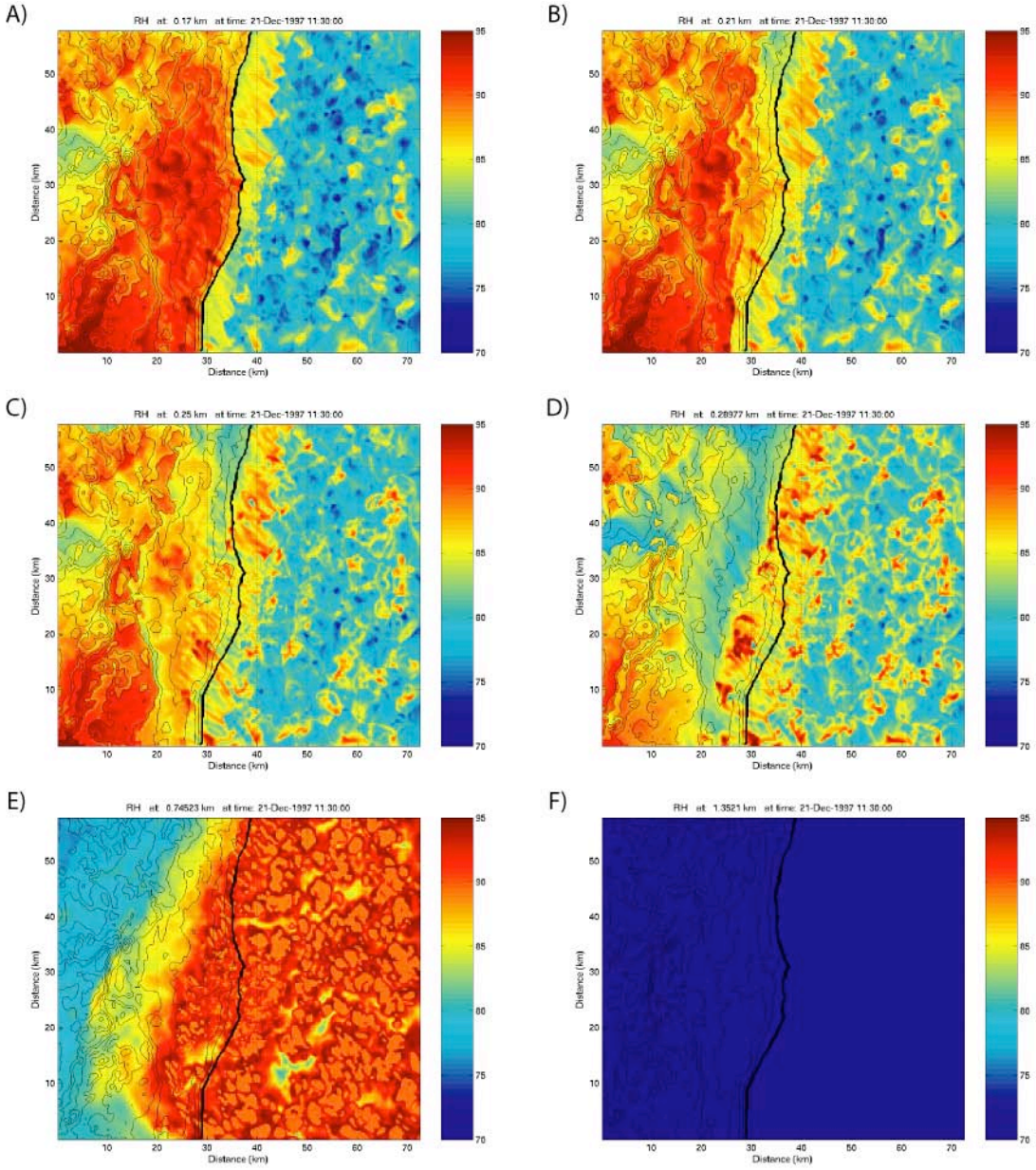

Figure 4.8: Simulation "B" grid 5 output for the relative humidity at the surface (A), 33 m above lake level (B), 73 m above lake level (C), 113 m above lake level (D), 573 m above lake level (E), and 1173 m above lake level (F). Topography is contoured in black. (Note: elevations stated in plot headings are absolute, and not from lake-level)

source in Lake Michigan. This is because of the temperature contrast between the two air masses, with the land breeze air being significantly colder. Because a portion of the air that is being drawn into the land breeze, either from above or from its farthest western extent has likely been over the lake in the recent past, its moisture content is higher than it would be if just coming over the Wisconsin topography. This can be seen at higher elevations, particularly the 573 m above lake level plot, in which it becomes obvious that the relative humidity of the return flow is quite high. Therefore, when this air is mixed with the flow moving offshore, and is cooled, it ends up having a higher relative humidity than the contrasting prevailing flow. This relative humidity gradient is of great importance to the lidar observations, since aerosol size is proportional to relative humidity (Covert et al., 1972; Fitzgerald and Hoppel, 1982; Day and Malm, 2001).

The second feature of note is the high relative humidity values over the shoreline at low levels. These are likely a result of the corresponding model grid points being located underneath the topography. Comparing the contours of topography and the high relative humidity areas, and noting that the high relative humidity areas basically follow specific topographical contours lead to this conclusion.

The 16 km sixth domain data reveals significantly more detail than can be determined from the fifth grid. Starting with the zonal velocities (figure 4.9), there are flow parallel streaks present in the land breeze, with the land breeze flowing from the west-northwest. These streaks appear to form at locations where the flow passes along the north side of a shoreline point that intrudes into the lake. This is likely an effect of the additional friction provided by the topography in these instances. Also noticeable is the alignment of the land breeze front with the shape of the shoreline. This is particularly

prevalent in the southern half of the domain, where the shoreline is oriented southwest-northeast, rather than south-north as in the northern half of the domain. These types of terrain effects have been brought up by previous studies, particularly one done by Winstead and Mourad (2000) in which the horizontal extent of a land breeze measured with Synthetic Aperture Radar (SAR) is compared to the surface roughness features of the terrain upwind of it.

The meridional component to the flow (figure 4.10) also reveals similar streaks to those seen in the zonal flow. Interestingly, however, here the streaks are in the opposite direction to the land breeze, with the land breeze itself showing a northerly component, and the streaks and the prevailing onshore flow both containing southerly flow. This northwesterly behavior of the land breeze has been previously documented in numerous studies, including those by Passarelli and Braham (1981), Ballentine (1982) and Alpert and Neumann (1983). The turning of the flow inside the streaks is likely a direct result of the zonal acceleration off of the shoreline, and the subsequent redistribution of the excess of mass inside the accelerated volume.

The turning of the accelerated flow also shows up in the vertical velocity output (figure 4.11). Land breeze parallel streaks of upward vertical velocities show up on the north sides of the streak locations over and inside the land breeze. This indicates that the northward turn visible in the meridional data is creating wind parallel convergence zones inside the land breeze causing a roll type circulation, with updrafts at this convergence zone. These circulations appear to extend up to the return flow, at which point the cellular structure of the offshore flow takes over. These wind parallel rolls also show up in the 5^{th} grid data (figure 4.7).

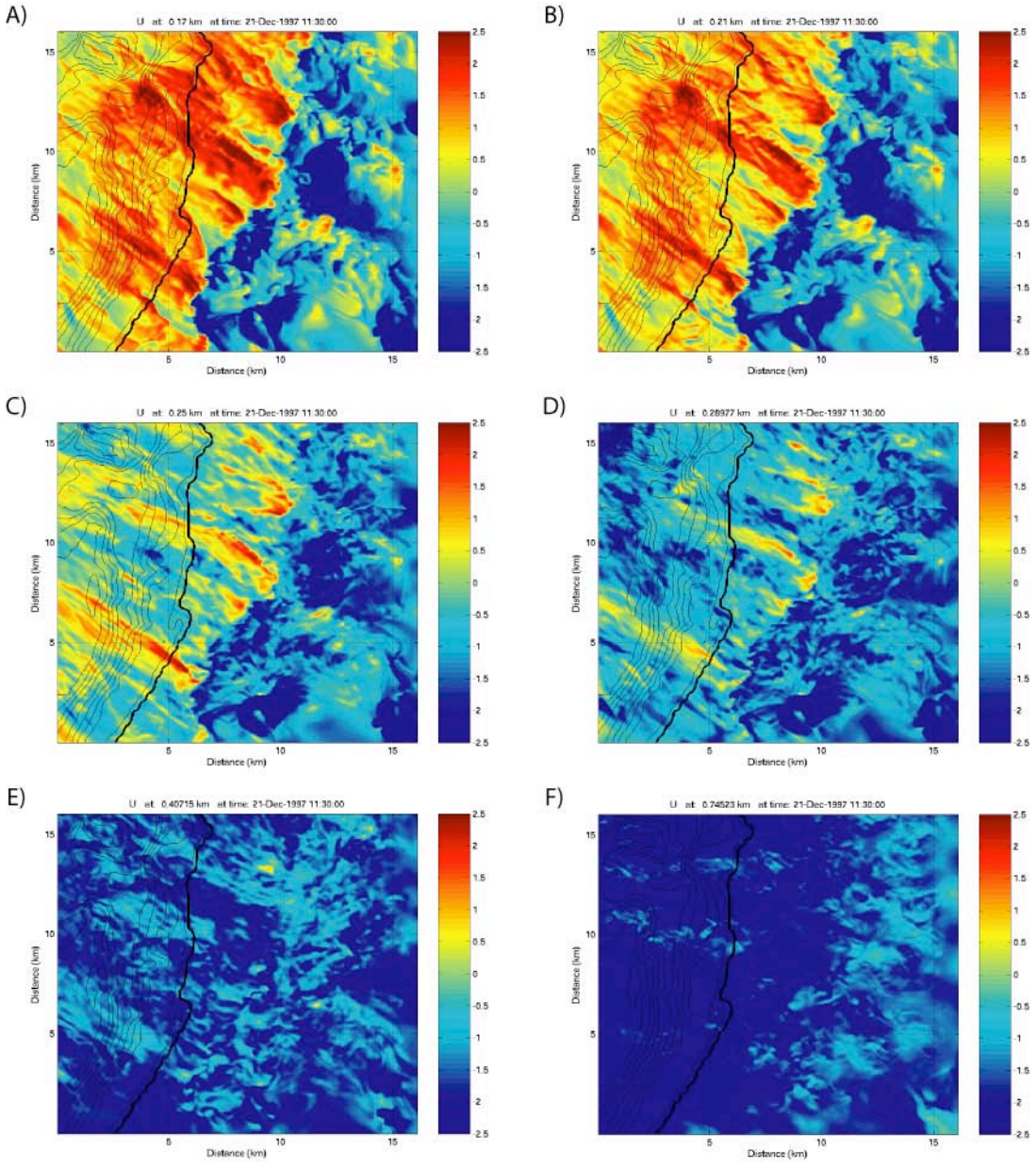

Figure 4.9: Simulation "B" grid 6 output for the zonal velocity component at the surface (A), 33 m above lake level (B), 73 m above lake level (C), 113 m above lake level (D), 213 m above lake level (E), and 573 m above lake level (F). Topography is contoured in black. (Note: elevations stated in plot headings are absolute, and not from lake-level)

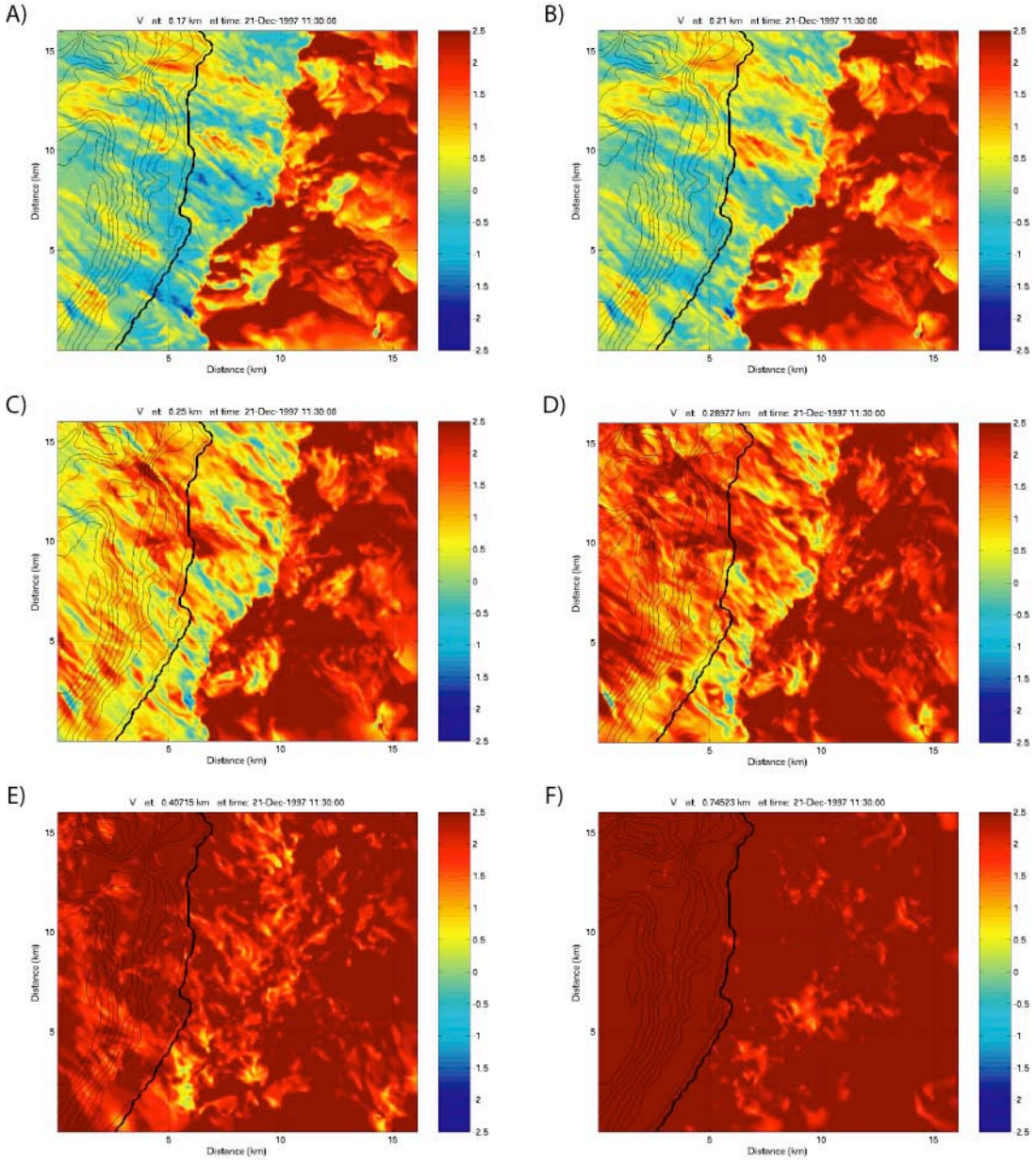

Figure 4.10: Simulation "B" grid 6 output for the meridional velocity component at the surface (A), 33 m above lake level (B), 73 m above lake level (C), 113 m above lake level (D), 213 m above lake level (E), and 573 m above lake level (F), from top. Topography is contoured in black. (Note: elevations stated in plot headings are absolute, and not from lake-level)

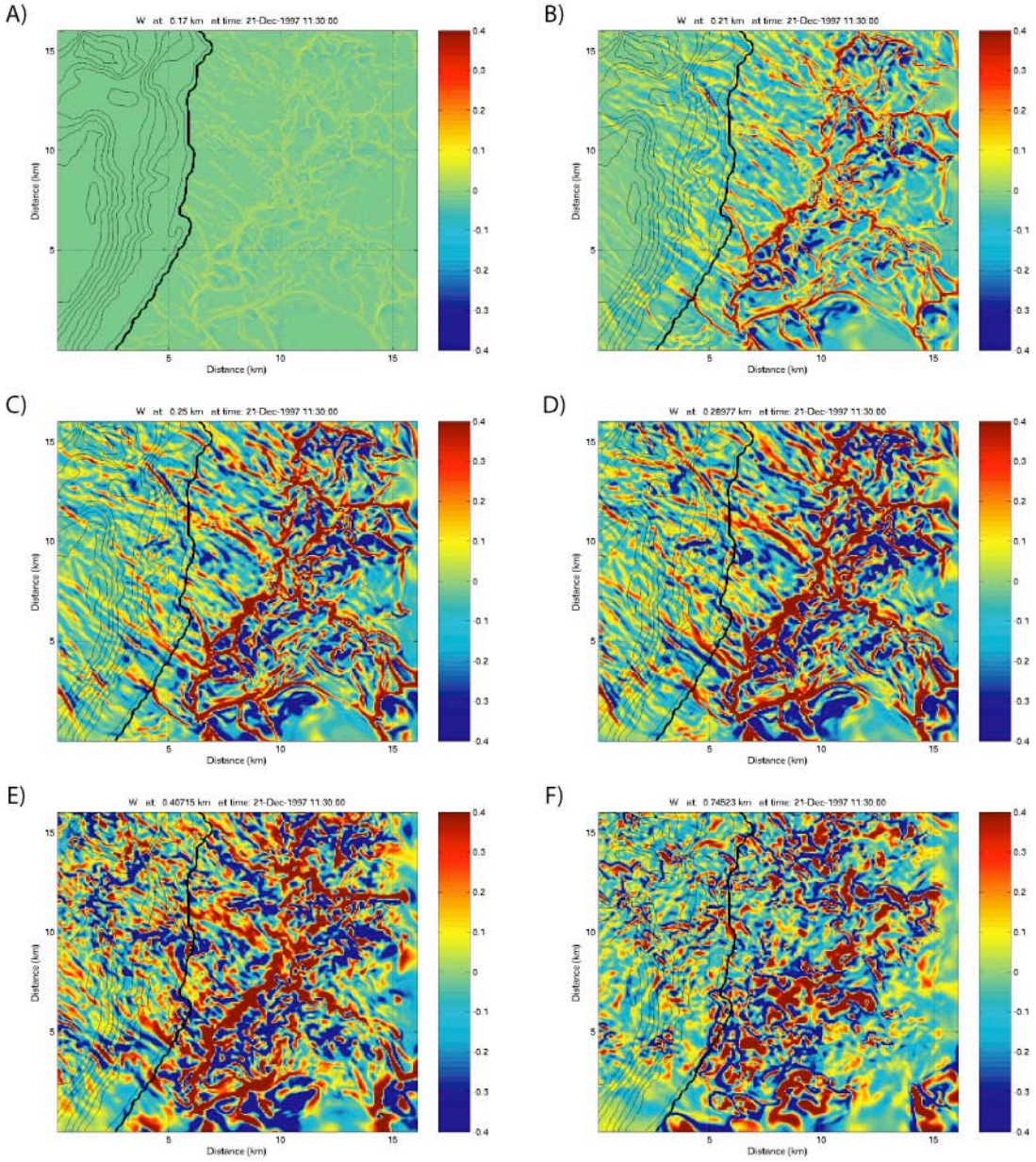

Figure 4.11: Simulation "B" grid 6 output for the vertical velocity component at the surface (A), 33 m above lake level (B), 73 m above lake level (C), 113 m above lake level (D), 213 m above lake level (E), and 573 m above lake level (F). Topography is contoured in black. (Note: elevations stated in plot headings are absolute, and not from lake-level)

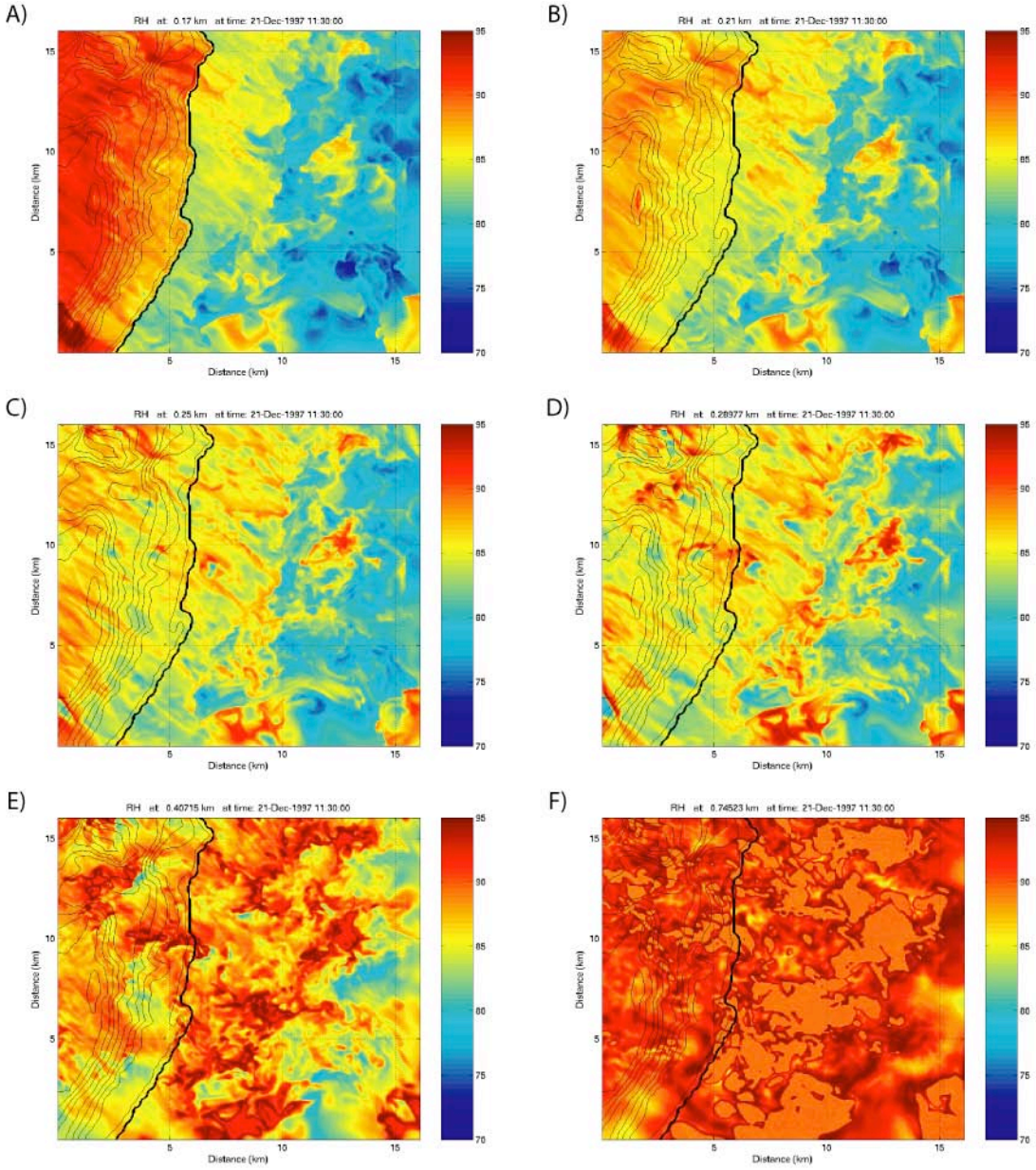

Figure 4.12: Simulation "B" grid 6 output for the relative humidity at the surface (A), 33 m above lake level (B), 73 m above lake level (C), 113 m above lake level (D), 213 m above lake level (E), and 573 m above lake level (F). Topography is contoured in black. (Note: elevations stated in plot headings are absolute, and not from lake-level)

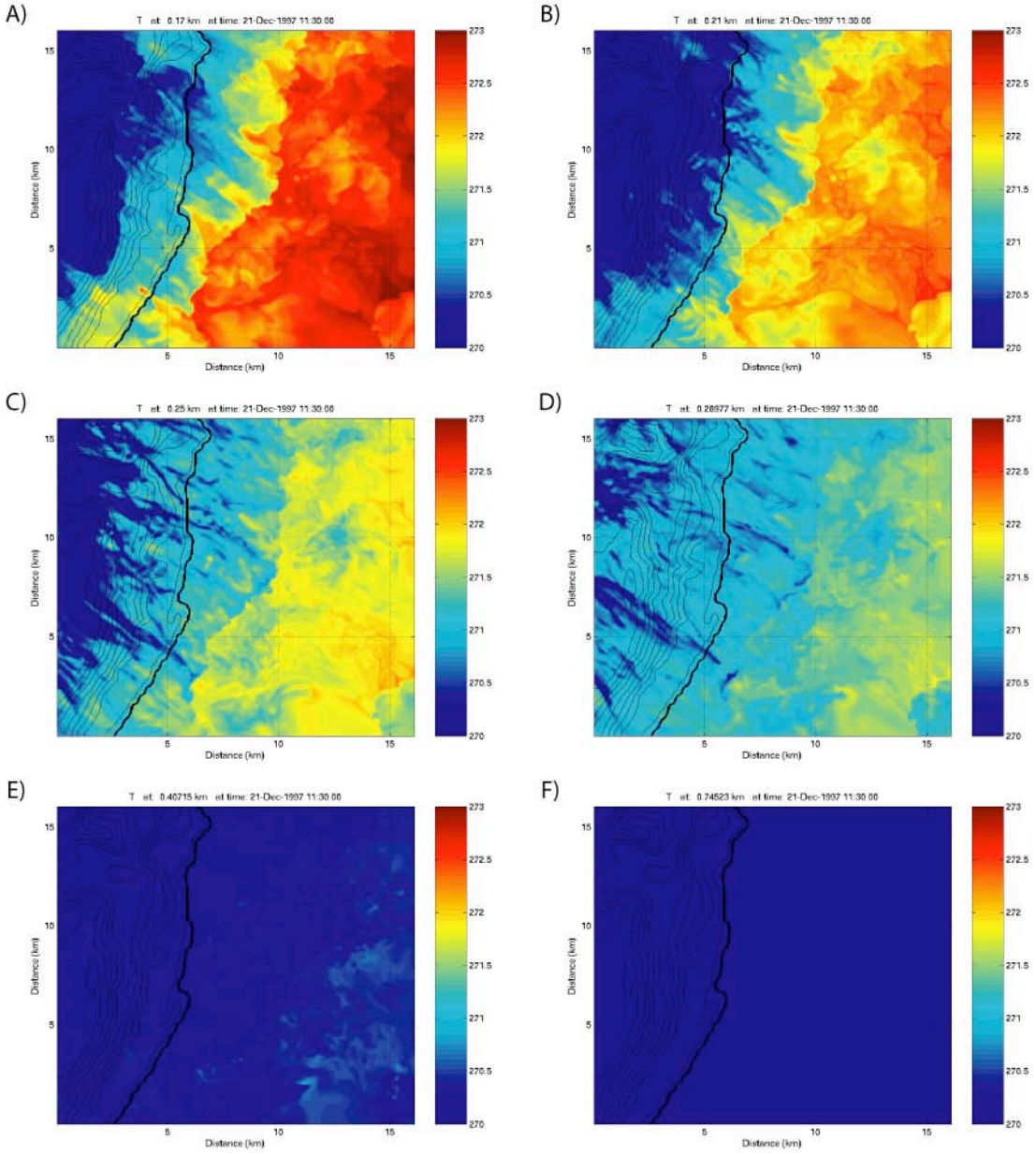

Figure 4.13: Simulation "B" grid 6 output for the temperature at the surface (A), 33 m above lake level (B), 73 m above lake level (C), 113 m above lake level (D), 213 m above lake level (E), and 573 m above lake level (F). Topography is contoured in black. (Note: elevations stated in plot headings are absolute, and not from lake-level)

The 6th grid relative humidity output (figure 4.12) reveals similar features as that of the 5th grid. The land breeze clearly has higher relative humidity values than the flow around it, with relative humidity increasing with altitude. The flow parallel streaks seen in the velocity data appear to advect regions of higher relative humidity out over the lake.

Finally, looking at the temperature output for the sixth grid (figure 4.13) the intricacies of both the land breeze and the prevailing flow, as well as those of the intersection between these flows become very apparent. Particularly at lower elevations, the temperature contrast is quite dramatic, with changes of 4-5 Kelvin over only a kilometer or so. These contrasts are most prevalent around the streaks discussed earlier. These areas of increased wind speed advect the colder air from over the land surface further out over the lake than the rest of the land breeze. This leads to an undulating intersection of the two contrasting flows. This undulation is also helped by the intermittent cellular structures of the convective onshore flow colliding with the boundary. The cells appear to overpower the land breeze individually at the point of intersection, similar to an air bubble intruding upon a liquid surface. The structure of these cells is also quite apparent in the temperature plots, with temperature differences of a degree or two across individual cells in the onshore flow near the surface.

4.2.3 Virtual Scattering Parameter

One of the elements added to simulation "B" is a virtual scattering variable produced inside the NMS. The technique used mirrors that implemented by Mayor (2001), in that it utilizes a passive tracer, together with the model relative humidity output in order to come up with a scattering estimation of the atmospheric state. The passive tracer is introduced at the initialization of the model run as 1 at the two grid points nearest to the

surface, and 0 elsewhere. It is then advected with the flow and distributes throughout the domains in a way similar to aerosols in the atmosphere, either increasing or decreasing in population depending on net convergence or divergence in one area.

This tracer is then multiplied by a relative humidity induced scattering parameter that is calculated from data collected in a study done by Fitzgerald et al. (1982). This is done in order to include the effect of swelling of aerosols in high relative humidity, as discussed in the introduction. A best-fit curve to the data from the Fitzgerald study (figure 4.14) represents relative backscatter as a function of relative humidity, and reveals the increase in backscatter caused by higher relative humidity. The equation to this curve is given by:

$$\alpha = -2.5 + \frac{8.4}{(100 - RH)^{0.2}} \tag{4.1}$$

where α is the relative scattering as a result of the relative humidity value (RH). As discussed in Mayor (2001), this is a very elementary technique for the reproduction of scattering in the simulation. The data that is used to determine the curve shown in figure 4.14 was taken in Washington DC for the particular aerosol population present at that time. Studies of aerosol type and population, as well as their effect on scattering for different relative humidity values specifically for the Sheboygan area would improve this estimation tremendously. Additionally, incorporating different tracers for the different types of aerosols present would increase the accuracy of this calculation. For this particular case, having some sort of source of tracer along the shoreline to replicate the effects of the industrial areas situated in this region would also aid in the accurate recreation of the aerosol concentration within the observed atmosphere. Figures 4.15 and

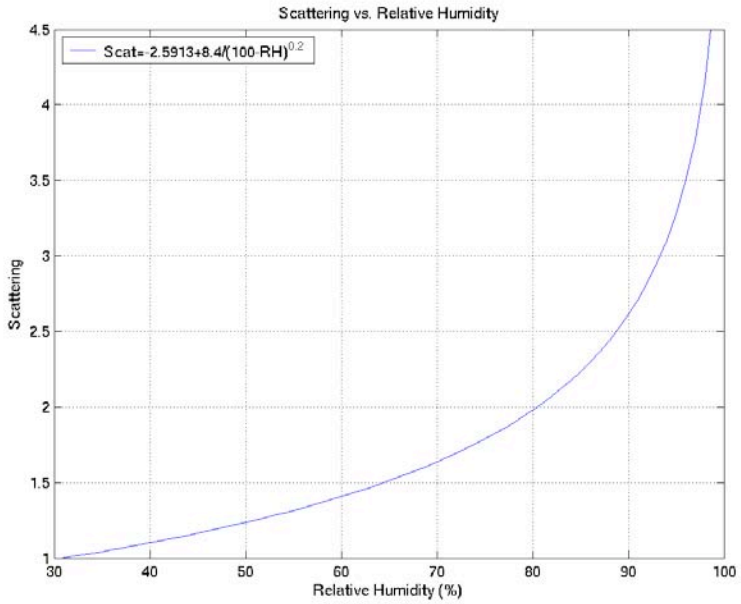

Figure 4.14: A best-fit curve to data from Fitzgerald et al. (1982) representing the relationship between relative humidity and scattering.

4.16 show the result of this scattering parameter, when applied to the sixth grid. Figure 4.15 is a cross section of the scattering parameter, showing the land breeze flowing offshore very near the surface of the earth. Also visible is the undulating top of the planetary boundary layer, shown by a sharp contrast in scattering at around 800 m. Waves along the top of the land breeze can be detected, likely Kelvin-Helmholtz type features resulting from the prevailing flow having to rise up over the head of the land breeze. Figure 4.16 depicts the virtual scattering parameter at several elevations above sea level. The decrease in scattering between the 73 m elevation and 160 m elevation in the land breeze location gives a good indication of the shallow nature of the circulation. Additionally, the streaks seen in the grid 6 data reviewed previously also present themselves in the scattering parameter. At the 160 m level, only the areas that contained strong updrafts, such as the frontal zone between the land breeze and the synoptic flow

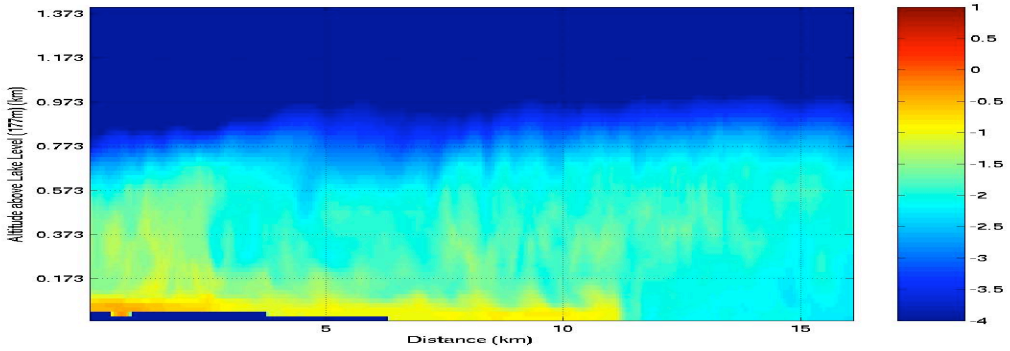

Figure 4.15: A cross-section displaying the virtual scattering parameter on the sixth grid. The blue blocky area on the bottom left is topography.

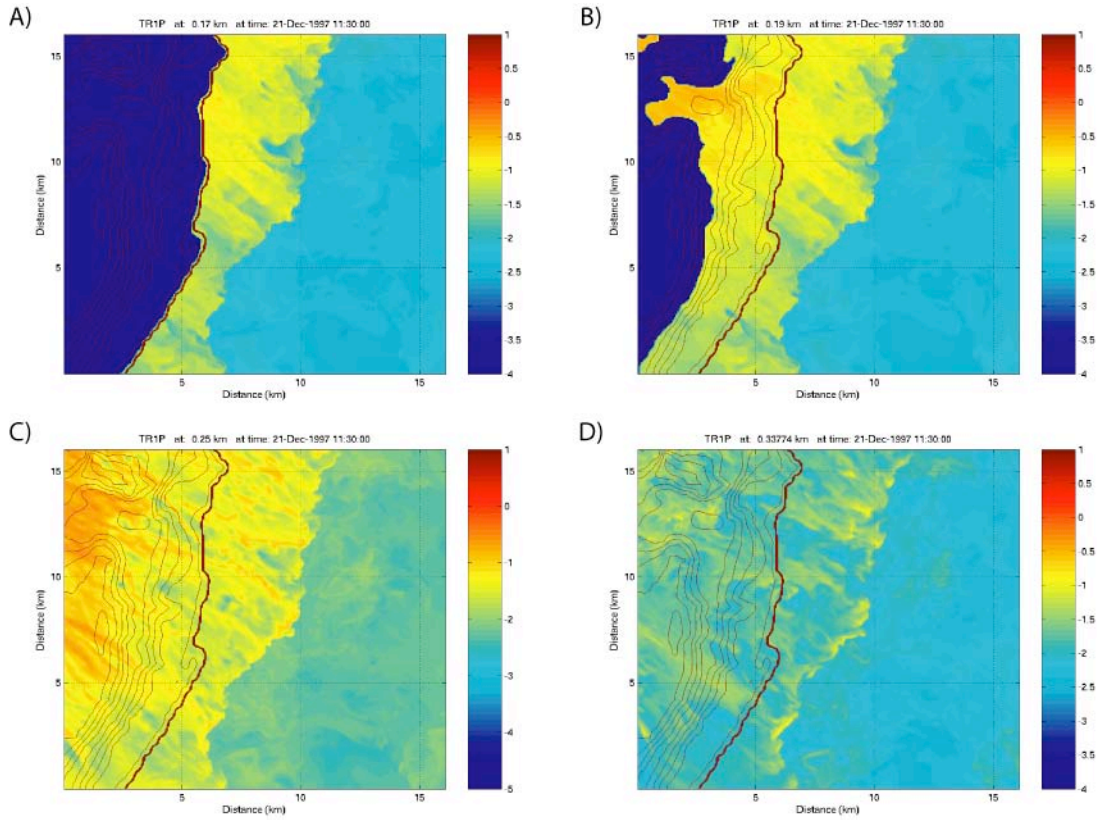

Figure 4.16: The virtual scattering parameter for grid 6 at lake level (A), 13 m above lake level (B), 73 m above lake level (C), and 160 m above lake level (D). (Note: elevations stated in plot headings are absolute, and not from lake-level)

still show strong scattering due to a maximum of tracer concentration in that area. One other interesting feature clearly detectable in the scattering data is the influence of the shoreline on the land breeze in the simulation. The scattering parameter shows the land breeze following the curvature of the shoreline relatively closely.

The next chapter will take the data presented in this chapter and compare it to the lidar observations discussed in chapter 3.

Chapter 5

Comparison of Lidar and Model Data

5.1 Overview

One of the most important portions of this study is the validation of model output through the lidar observations taken. With the help of the VIL and NDBC site data, we can begin to address some of the questions presented about predictability and forecast improvement. Here, two approaches are used in order to do this comparison between the two datasets. The first involves quantitative comparison between model and lidar results. Since the lidar only measures relative backscatter directly, a crude attempt is made at incorporating a similar variable in the virtual scattering parameter into the UW-NMS, as discussed in chapter 4. With this model scattering we can use variance calculations to derive the land breeze depth, horizontal extent, land breeze head depth, and boundary layer depth. Another method of deriving quantitative results involves extracting information from the lidar data that can be compared with model variables. This is done in the present study to make comparisons of wind speed and direction. The second approach used to validate the model output is a qualitative comparison with the lidar data. Comparison of the shape and extent of the land breeze can be done this way, and it is

particularly important in comparison of the undulating structure of the land breeze front, which would likely be lost in statistical comparisons.

Using these techniques, several aspects of both the land breeze as well as the flow surrounding it were analyzed. Characteristics derived from the lidar data include all of those presented in the previous paragraph as able to be determined from the variance calculations. Additionally, the data from the NDBC site is used in order to further validate the conditions around Sheboygan Point produced by the model.

A central issue in the validation of this circulation is the timing of the events associated with it. In this chapter, model accuracy in recreation of both the event itself, as well as the timing associated with the evolution of this land breeze will be reviewed.

5.2 Timing of the Simulation

One of the more important points that this work is meant to address is that certain types of small-scale phenomena can, and must, be simulated from the large scale down. Because of this, the position and existence of the land breeze must be controlled, to a certain extent by the large-scale flow. Therefore, the timing of the land breeze should be able to be simulated with some accuracy. The most elementary event to be reviewed is the break down of the land breeze simulation. This is the point at which the land breeze front retreats over the shoreline at Sheboygan Point, out of the lidar field of view. Additionally, the large-scale frontal position leading up to the break down can be compared, in order to test the speed of evolution in the simulation against the actual evolution.

Figure 5.1 compares the surface wind speed and direction of the simulation output with the wind speed and direction measured at the NDBC site. The NMS appears to

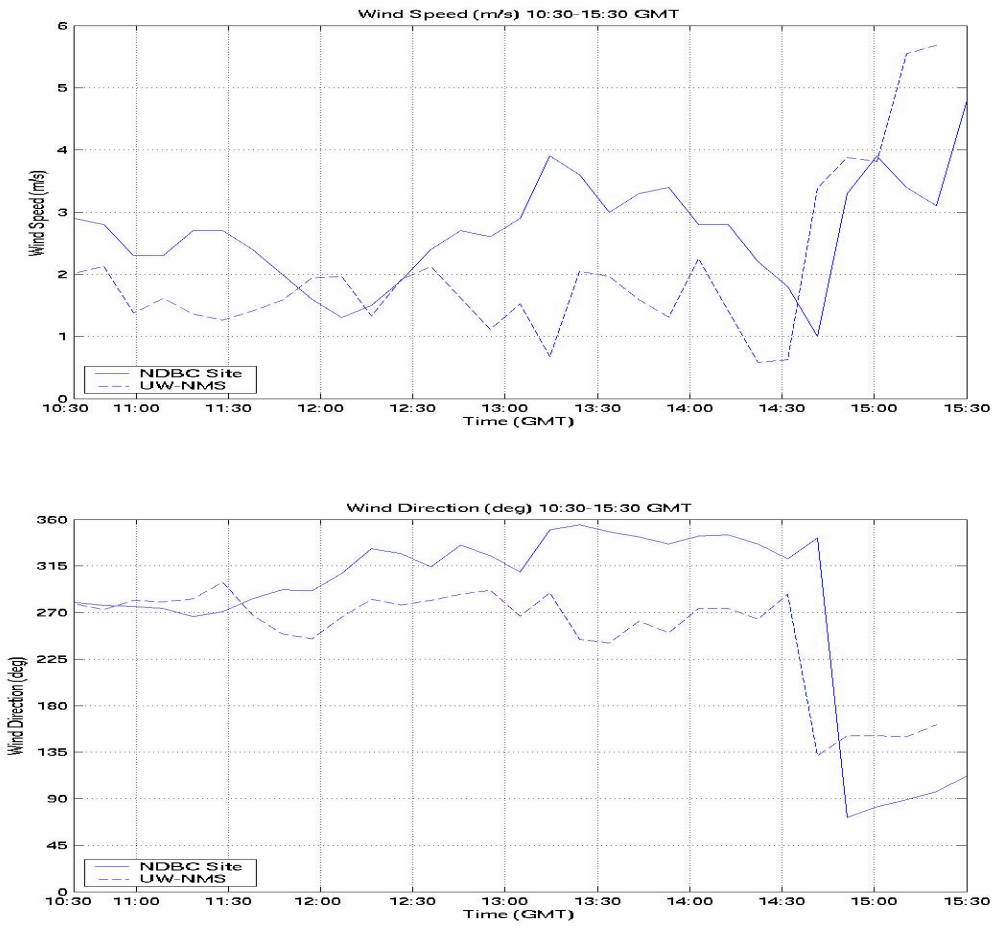

Figure 5.1: Comparison of the simulation surface wind speed (top) and direction (bottom) and the NDBC measured speed and direction for the period 10:30-15:30.

simulate a weaker land breeze than observed. More importantly, the simulation appears to closely replicate the passage of the land breeze front over the NDBC site, with a noticeable increase in speed. This passage comes out even more clearly in the wind direction plot, with winds shifting suddenly from the west to the southeast. Again, the timing of the passage of the front appears to match remarkably well, with both sets of data showing the wind shift occurring at around 14:45.

Looking at the NDBC data from even later on in the period (figure 5.2), it becomes obvious that, although there was an original shift in the winds, the land breeze has a final

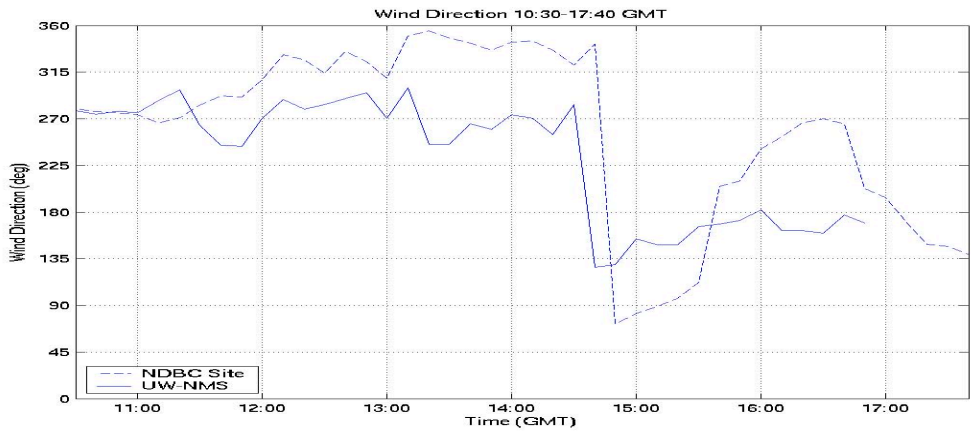

Figure 5.2: Surface wind direction measured at the NDBC site from 10:30 to 17:40 on December 21, 1997.

push, which carries it back offshore. The final shift in wind direction does not occur until 17:00 or so, a similar observation to that made by the VIL operators for the date. Interestingly, there is no mention of the earlier wind shift in the operator logbook, nor is it clearly visible in the lidar data. This is likely a result of the NDBC site being situated offshore. Also, the simulation structure indicates that there is a possibility that the land breeze was so shallow at this point, that a wave coming over the top of the land breeze actually reached near enough to the surface for the wind to shift at the NDBC site as that particular wave passed. The fact that the land breeze gradually recovers before dying off again would seem to indicate that this was not just a temporary convective cell breaking into the land breeze, but possibly an early warning indicating the termination of the circulation. This is also shown by the fact that the simulation also predicted this change at almost exactly the correct time, leading to the conclusion that this shift is a large-scale frontal passage. The smaller scale motions would not likely be timed with the accuracy that is shown in the original wind shift. This plot also reveals the difficulty the UW-

NMS has with trying to simulate the timing of the smaller scale effects, as the recovery of the land breeze does not occur in the simulation output.

5.3 Simulation of A Land Breeze

As shown in the preceding chapter, a land breeze was present in several NMS simulations run for December 21, 1997. Comparisons done for all simulations with the exception of simulation 'B' do not include any type of virtual scattering, and all means for comparison need to be inferred from the model output of meteorological parameters. Some of these methods are discussed at the end of this chapter. With the introduction of the virtual scattering in simulation 'B', more direct comparisons can be done between the two data sources. Due to this, the comparisons will focus on this simulation, with a brief mention of comparison techniques used to validate other simulations and the observations from those comparisons.

5.3.1 Simulation 'B'

Besides having the virtual scattering parameter available for comparison, simulation 'B' also incorporates larger grids, and is able to better represent mature turbulence in the center of the nested domains. Care has to be taken to not rely solely upon the virtual scattering parameter for validation since several different aspects influence scattering. These include relative humidity, anthropogenic sources of aerosol on both the shore and over the lake, and natural sources of aerosol such as blowing dust. Out of these, relative humidity is the only one that is truly accounted for in the model. The other sources are generically grouped into a tracer in order to get a feel for the relative backscatter between areas of different concentrations. Therefore there is no discrimination between different

sizes and shapes of aerosol, or are there any continuous point sources for production of such aerosol. Additionally, the best-fit curve used to relate scattering to relative humidity was created using data from Washington DC, and this region likely has different aerosol types and concentrations than the Sheboygan, WI shoreline. For these reasons, parameters other than the model-produced scattering are also reviewed.

Figure 5.3 shows comparisons of the model derived wind direction and speed as well as water and air temperatures with the same quantities measured at the NDBC site. There is remarkable agreement between the model predicted wind directions and the measurements made onsite with the exception of the end of the data period. Noticeable in both the wind direction and speed plots is an increase in variation in the data after 10:30 GMT. At this point, the sixth grid was introduced into the simulation, and it is likely that the spin up process from the inner grid effected the measurements made on grid 5. The NMS wind speed does appear to be slightly lower than those measured at the NDBC site. A possible explanation for this lies in the plot of the temperature data, as the temperature difference between the air and the lake surface is about one degree lower in the model than the one presented in the measured data. This decrease in thermal gradient would lead to a weaker land breeze. Since the wind direction is in general agreement with that measured, this is a likely scenario. This is a good example of a small difference in the large-scale conditions that leads to more significant errors at the microscale. The effect of this particular chain of events on the position of the land breeze front will be reviewed later on in this chapter. Another point of interest in the temperature data is that there is no variation in the model-produced data. This is because the temperature and lake temperature, as measured in this simulation are rounded to the nearest whole degree

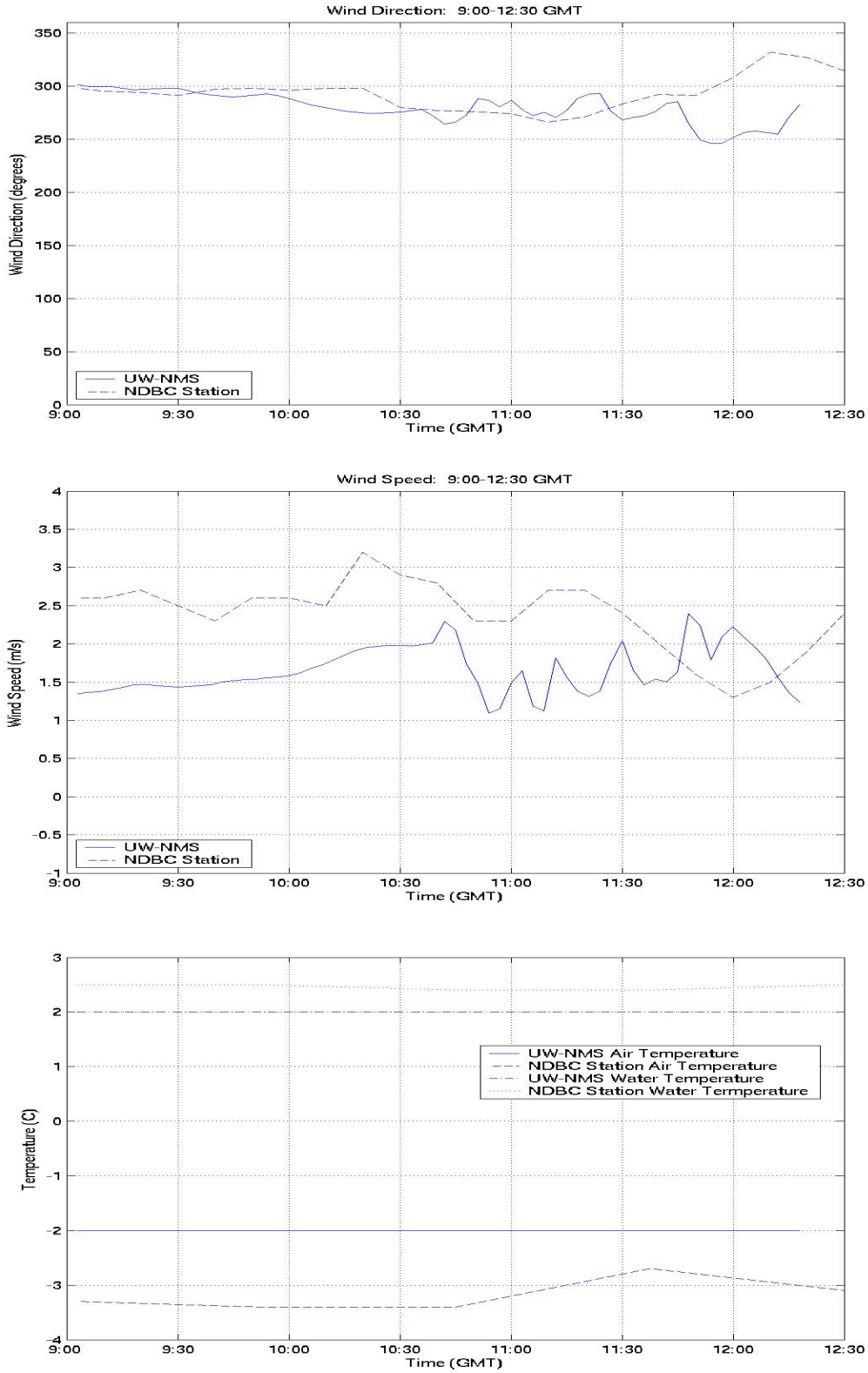

Figure 5.3: Surface wind direction (top), speed (middle), and air and water temperature (bottom) data for the 5th grid of simulation "B" when compared with NDBC observations.

Kelvin. Therefore, there is about a 1 K range of temperatures that can result in the same model output, resulting in little variation.

The virtual scattering parameter is implemented in a model-produced RHI volume scan in figure 5.4. For comparison, a VIL RHI volume scan is positioned below it. Comparison of these images reveals some striking similarities. First, the planetary boundary layer depth appears to be almost identical at around 800-900 m. It can be picked out by the sharp contrast in backscatter between the well mixed, relatively dirty boundary layer and the cleaner, free-flowing atmosphere above.

Another similarity is seen in the horizontal extent of the land breeze. Both images have the land breeze extending 4-5 km offshore. The difference between the horizontal land breeze extent displayed in the upper RHI images is again due to the angle at which the VIL was scanning to capture that data. Since it is not perpendicular to the shoreline, but rather at 144.5° relative to north, there is larger amount of land breeze for that scan to pass through when compared to a scan pointed perpendicular to the shoreline (~90 ° to north), as is the case with the model output. The major discrepancy with respect to horizontal position of the frontal zone at this particular instant in time occurs in the most southerly portions of the CAPPI images. In the lidar imagery the front appears to only slightly curve with the shoreline curvature, while in the model output, the front curves very sharply towards the shoreline. This appears to be partly due to the westward recession of the shoreline, and partly due to the interaction of the land breeze with the prevailing flow. Undulations along the frontal zone are common as the land breeze interacts with the convective cells shown to exist in the outer flow, and collision with

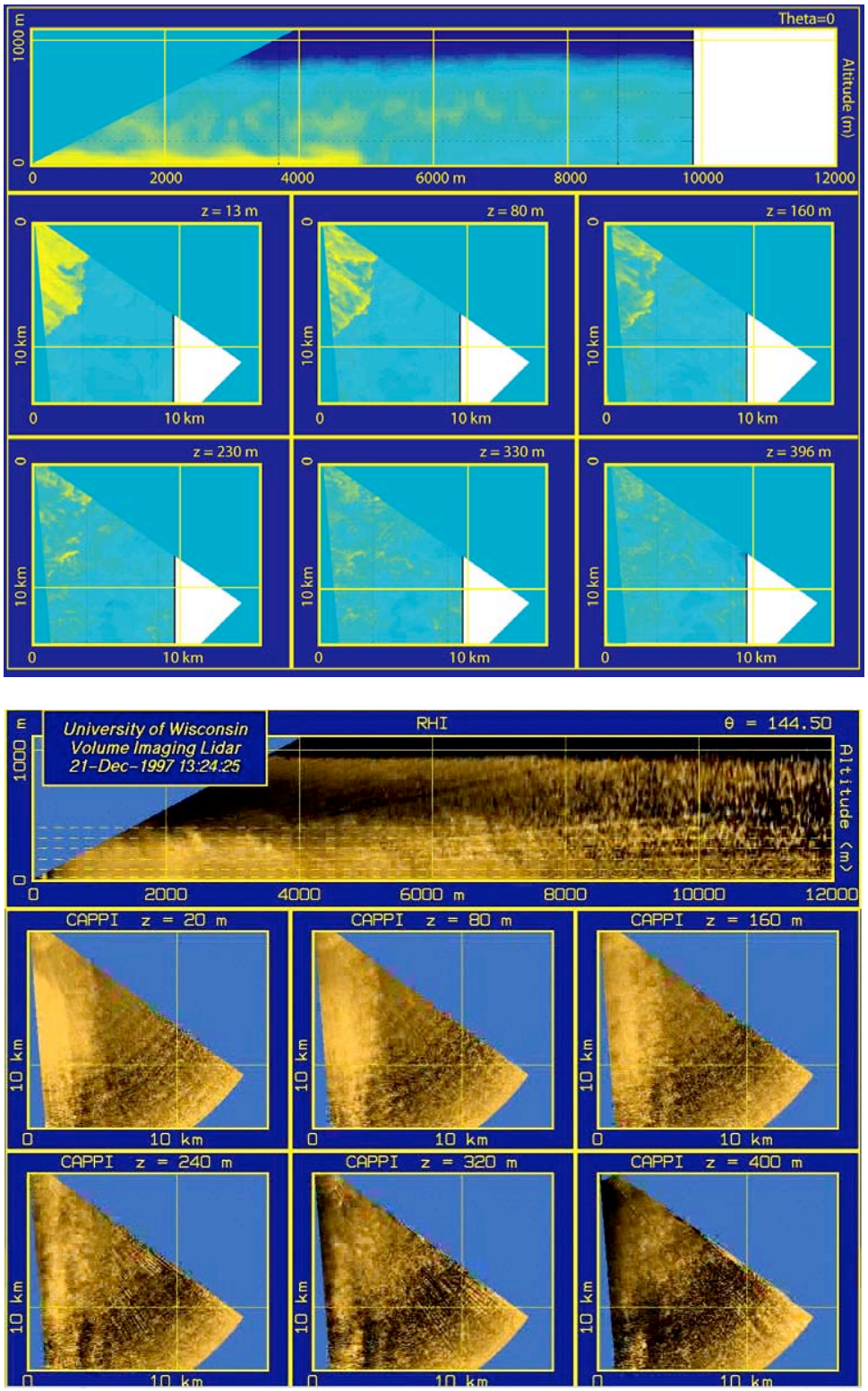

Figure 5.4: 6th grid virtual scattering output from simulation 'B' (top) and backscatter measured with the VIL (bottom).

particularly strong cells leads to greater indentation of the frontal zone towards the shoreline.

Also apparent in the virtual scattering image is how the utilization of this tool allows visualization of boundary layer features that would not otherwise be discernable by looking at one specific meteorological parameter. The scattering output clearly shows a layer of higher backscatter in the middle of the boundary layer, similar to that seen in the lidar data. Also noticeable here is the presence of a billowing type motion over the top of the land breeze, and a clear wave-like structure in the top of the land breeze itself. This is likely in part due to the larger size of the high resolution 6th grid, which allows more mature turbulent structures to interact with the land breeze, as well the implementation of the tracer in the scattering variable. This billowing motion is the cause of the entrainment of warmer air into the land breeze, as well as the introduction of cooler air into the convective flow that is overrunning the land breeze circulation.

Unlike the early example shown in figure 5.4, the majority of the lidar imagery taken on the date shows the land breeze extending only 1-2 km offshore. In contrast, the model keeps the frontal position at around 4 km offshore. This is where the small errors at the large scale become very important! At first, in reviewing the comparison of the simulation with the NDBC data, this does not seem to make sense. In that comparison, the simulated land breeze appears to be slightly weaker than the observed land breeze. This would lead one to believe that the simulated land breeze front would be closer to the shoreline than the observed front, since the weaker land breeze would have a more difficult time combating the prevailing flow. This, however, is a very good example of how comparison with point measurements can be misleading, and can lead to false

assumptions about the nature and strength of the flow. As illustrated in the next paragraph, a look at the entire domain reveals why the front is indeed further offshore in the simulation. This is also a clear example of how very small differences in dynamic structures can have significant impact in terms of wind speeds and directions, leading to, in this case, a miss positioning of the land breeze front.

In order to get a better feel for the statistics of the entire flow, a comparison was done of the wind field utilizing wind speeds and directions gathered through the implementation of cross-correlation techniques on the lidar dataset. The results from this comparison are shown in figure 5.5. The top image in figure 5.5 shows the lidar derived wind field for an area 1-2 km south of the lidar site, and extending offshore. The data indicates a latitudinal average, over a 40-minute period. Both the wind speed and direction plots show very clearly the land breeze, and the frontal zone, with winds shifting from around 285 degrees to around 130 degrees around 1.5 km offshore. Additionally, the wind speed increases dramatically outside of the land breeze, with wind speeds around 3-3.5 ms^{-1} in the offshore wind, as compared to only 0.5-1.25 ms^{-1} in the land breeze. The data in the vicinity of the land breeze front is not included here, due to difficulties with the cross-correlation technique at this extremely inhomogeneous intersection of two different flows.

A similar plot created from a 40-minute average using the model wind output paints a similar, though not identical picture. Again, the land breeze is clearly visible, extending around 4 km offshore. Wind speed inside the land breeze is again weak, ranging from .75-1.5 ms^{-1}, and the offshore flow is around 2-3 ms^{-1}. With this data, we get a much better feel as to why the land breeze in the simulations extends further offshore.

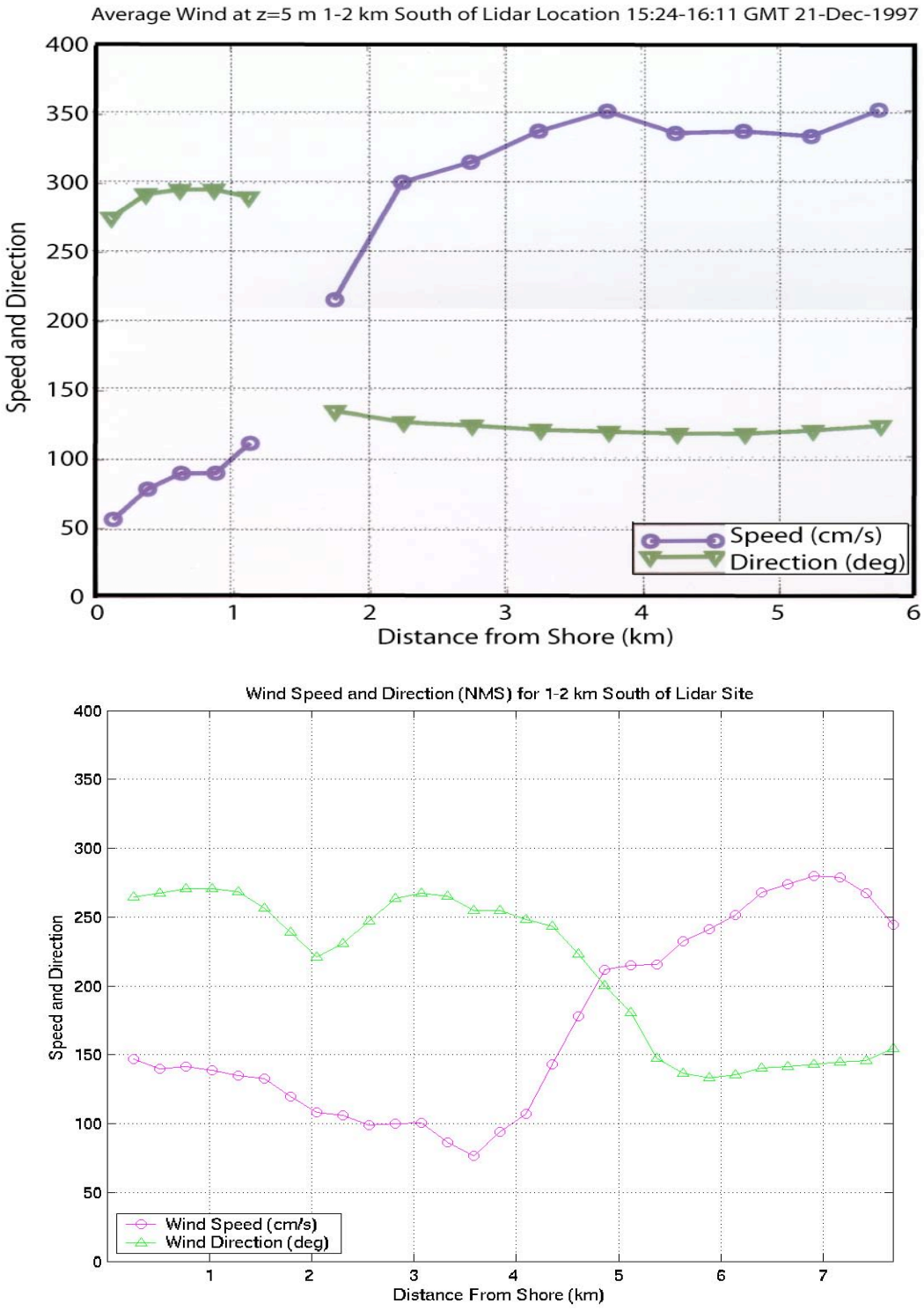

Figure 5.5: Wind speed and direction for an area 1-2 km south of the lidar site, and extending offshore. The top image shows winds derived from cross-correlation techniques implemented upon the lidar data, and the bottom image shows a similar image from model surface wind data.

First, the synoptically forced flow outside of the land breeze is weaker than in the lidar observations by approximately 1 ms^{-1}. Although this does not seem like a lot, it is quite significant when opposing a 1-2 ms^{-1} flow. Also, the direction of the land breeze appears to be more westerly in the model data, implying that it is more directly perpendicular to the shoreline, allowing the land breeze to reach further offshore. A third reason for the difference in frontal positions between the lidar data and the simulation is found in the speed of the land breeze itself. Although it is only slightly higher in the simulation (by 0.5 ms^{-1} or so), this slight difference is quite significant when dealing with flows that are only between 1-3.5 ms^{-1} to begin with, resulting in a further extension of the land breeze offshore. Here, it becomes obvious how comparison with the multi-dimensional dataset taken by the VIL is extremely helpful in diagnosing issues with a simulation at these scales, and how this analysis method aids in the detection of small discrepancies between model and observed variables. As illustrated, dynamical differences that lead to discrepancies in wind speed of less than 1 ms^{-1}, or in wind direction of a few degrees can be of vital importance to the quality of the small scale forecast.

Another useful method for comparison between the lidar data and the model output is the calculation of variances in gradients of specific variables across the front. Figure 5.11 illustrates this type of comparison using the virtual backscatter from the NMS and the backscatter from the lidar data. This is done with the idea that there are sharp gradients in specific meteorological parameters across the front.

The variances are calculated through comparison of the actual gradient between two specific points with the mean gradient between any two adjacent points. After the mean

difference between two adjacent points is calculated, the variance is calculated using the following formula:

$$\text{var} = \left(\overline{\Delta} - \Delta_{actual}\right)^2 \tag{5.1}$$

where $\overline{\Delta}$ is the mean gradient between two adjacent points for the entire domain, and Δ_{actual} is the actual gradient between two specific points. These variances are then averaged meridionally over lengths of approximately 2.3 km. This is done to derive a better representation of the frontal structure. The entire domain cannot be done at once, however, since horizontal variations in frontal position will then lead to the variances being comparable over large horizontal areas, rather than showing a distinctive peak at the front.

Utilization of this technique on the backscatter produced by the model and the lidar data allows for comparison between the two datasets. Figure 5.6 shows this comparison, and reinforces the previous conclusion that the model has the front too far offshore. This can be seen by the large peak in the variance calculations at 2-4 km offshore, depending on where in the domain the calculation is done. The lidar data has the peak closer to shore, typically between 1 and 2 km. Also in this figure, it becomes evident how the nature of these charts varies with the horizontal structure of the land breeze front. A very straight north south oriented front over the area of the calculations, as in the top 2.3 km section of the lidar imagery and the second section of the model virtual scattering output will produce a very distinctive peak in the variance at the frontal location. A frontal orientation that includes more of an east/west tilt will produce a wider area of increased variance due to the front being at several locations over the averaged area. The third

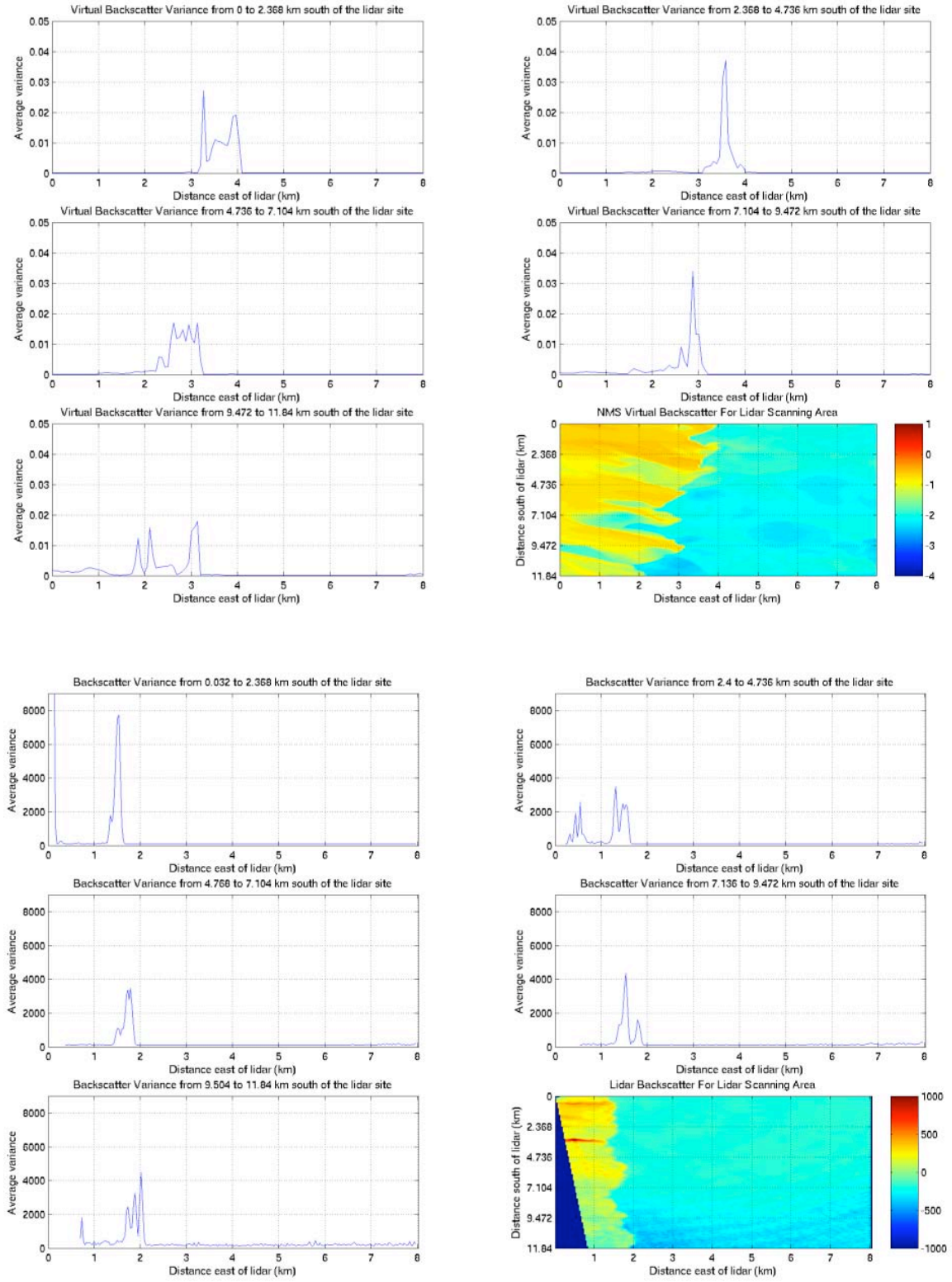

Figure 5.6: Variance calculations taken from the NMS virtual scattering parameter (top) and the lidar data (bottom) in order to determine the position of the land breeze front.

averaged area in the NMS output, in which the front slants from northeast to southwest, and the increased variances are noticeable between approximately 2.5 and 3.25 km offshore, best illustrates this case.

Similarly, figure 5.7 shows variance figures taken from a vertical cross-section. From these plots we can compare land breeze depth, boundary layer depth, and land breeze head depth, as calculated from the scattering parameter. The top half of this figure shows the NMS derived variances, split up into the variances calculated on the left half of the image and those from the right half. The left half plot shows very clearly the edge of land breeze at around 80 meters above lake level, as well as the head of the land breeze as a secondary peak in the variance at around 173 meters above lake level. Both sides show the variance at the top of the boundary layer, as a small peak starting at around 650 meters. The bottom portion of figure 5.7 shows a similar figure for the lidar retrieved backscatter field. Here we see the effect of the top of the land breeze at around 40-50 meters, with the head of the land breeze showing up as the larger peak at around 140 meters. Also more evident in the lidar data is the effect of large eddies in the convective boundary layer, with noticeable variances showing up throughout the domain. Again, the top of the boundary layer shows up in the variance data, with a very large peak starting at around 700 meters. Interesting in this case is that the top of the boundary layer causes much larger variances than the top of the land breeze. This is a result of small clouds along the top of the boundary layer causing extremely high backscatter. This effect is not fully taken into account in the simulated backscatter. Comparison of the NMS and VIL produced variance plots shows general agreement between the boundary layer depths, with the VIL having a slightly shallower land breeze. This again makes sense, since it

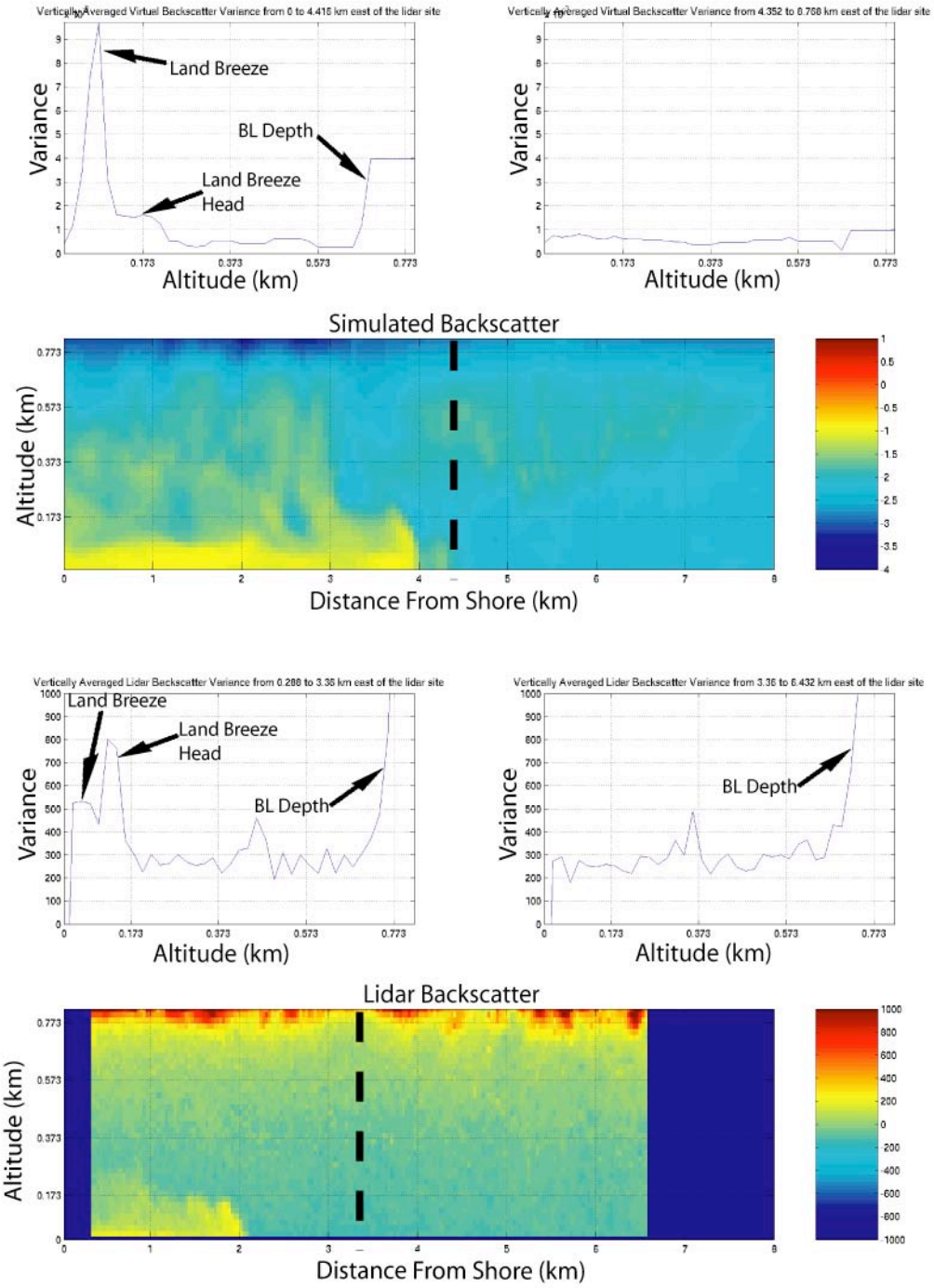

Figure 5.7: Variance calculations taken from vertical cross-sections of the NMS(top) and lidar derived backscatter fields.

also is smaller horizontally.

This sort of calculation can also be done for other variables produced by the NMS. An example of this is shown in figure 5.8, in which wind direction variances are calculated for the same NMS time step and area as the virtual scattering plots shown in figure 5.6. Comparison of the two variables shows that although the two plots are generally similar, they are not exactly the same. This is particularly true in the fourth comparison area, where the virtual backscatter gradient shows a variance peak at around 3 km offshore, while the wind direction gradient has more of a bimodal variance distribution. This discrepancy between the two shows that a combination of different variables may be needed in order to most accurately determine the frontal position. The wind direction calculations also show evidence of some of the convective structures offshore, with wind gradient variances showing up at around 5 and 7 km in the last averaging area as well as around 6 km offshore in the second averaging area.

One question that needs to be addressed is whether the downscaling technique actually improves the accuracy of the prediction resulting from the simulation. If interpolation of the large scale, as commonly done in statistical downscaling, would lead to a similar forecast, then the computational expense of the high resolution is not justified. In one of the comparisons done in order to investigate this issue, time series of wind speed and direction were created from two simulation runs for Sheboygan Point and compared to the observations recorded at the NDBC site (figures 5.9, 5.10). The first of these simulations was run at a typical mesoscale simulation resolution (12 km), while the second simulation shown is simulation 'B'. Data was plotted at 10-minute intervals from both simulations, for the NDBC site. Linear interpolation was used for the low-

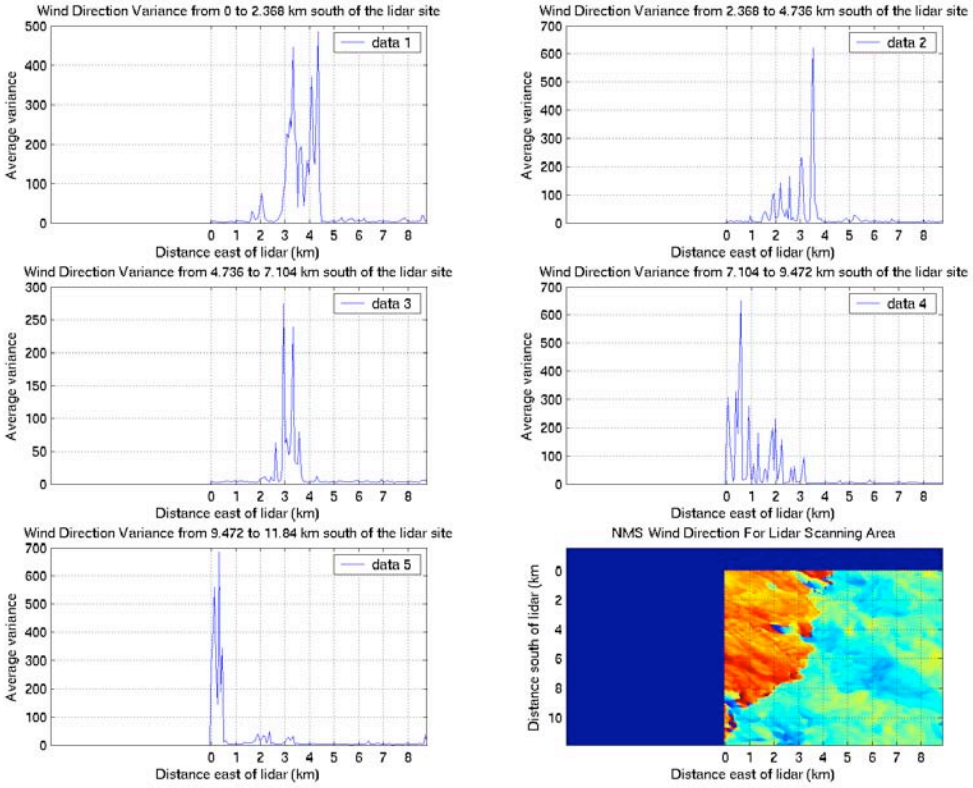

Figure 5.8: Variance calculations from the NMS calculated wind direction.

resolution simulation, since the resolution was not sufficient to pinpoint the specific location of the recording site. The wind speed plot (figure 5.9) shows the same general trend for all three datasets, with the wind speed gradually increasing with time. The high-resolution simulation, however, shows the rapid fluctuation of the wind speed that shows up in the NDBC data, as well as the sharp increase associated with the passage of the land breeze front around 14:45 GMT. Similarly, in the wind direction plot (figure 5.10), the high-resolution simulation reproduces the conditions observed at the NDBC site with significantly improved accuracy. Interpolation of the coarse resolution does not capture the land breeze due to the fact that the land breeze is not resolved at all at this

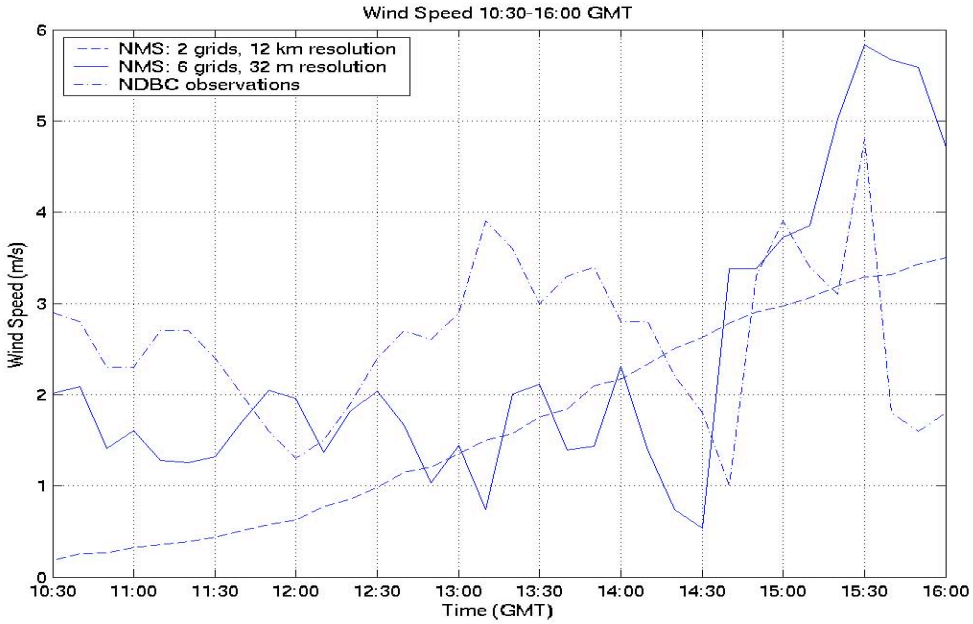

Figure 5.9: Wind speed as a function of time (at 10 minute resolution for all lines) for the period from 10:30-16:00 GMT. The solid line is the output from the high-resolution simulation, the dashed line from the low-resolution (12 km) simulation, and the dash-dot line the recorded data at the NDBC site.

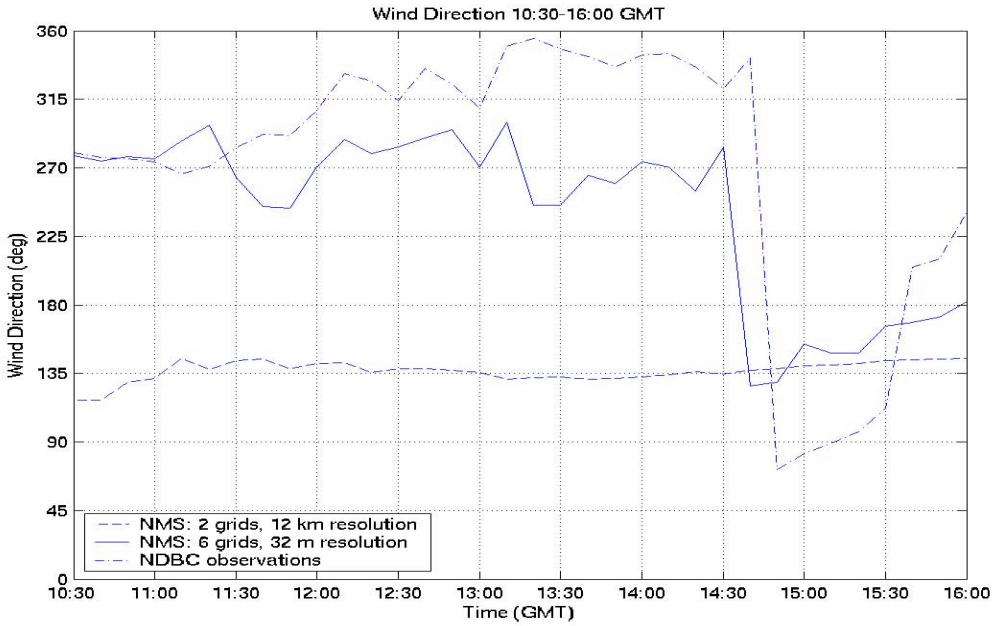

Figure 5.10: Wind direction as a function of time (at 10 minute resolution for all lines) for the period from 10:30-16:00 GMT. The solid line is the output from the high-resolution simulation, the dashed line from the low-resolution (12 km) simulation, and the dash-dot line the recorded data at the NDBC site.

resolution. Therefore, the land breeze is completely missed at the coarse resolution, together with undulations in the flow that are recorded at the NDBC site and in the high-resolution simulation. Although this result may be somewhat expected, it is a very important factor in determining the value of increasing resolution to this extreme, and addressing the question posed earlier about the benefit of increased resolution in simulations featuring land surface modulation of the predictable large-scale flow. The answer appears to be that there is significant benefit, since these comparisons reveal that there is substantial improvement in the wind speed and direction predicted for Sheboygan Point when the high-resolution simulation is used.

Naturally, the ability to justify the resolution of a simulation is dependant upon what information is needed from that simulation. In this particular study, if the explicit structure of the land breeze is not of importance, there is very little need for the inclusion of the sixth domain. As can be see in figure 5.11, both the fifth and sixth domains have the land breeze present, with similar dimensions. The land breeze shown in the fifth grid, however, has a flat top, and a significantly shallower boundary layer over the land breeze. This is due to the inability of the simulation to include turbulent structures along the top of the land breeze at the resolution of the fifth domain. After the addition of the sixth domain, however, these structures clearly show up, and the simulation more closely resembles the lidar data, as shown earlier in this chapter. Although the land breeze is still present in the fifth domain alone, there is no indication of undulation along the top of the flow. If the simulation is used for forecasting purposes, the knowledge that is gained from the inclusion of the sixth grid is simply about the nature of the circulation, rather than of the existence or general position of the circulation. The decision as to whether or

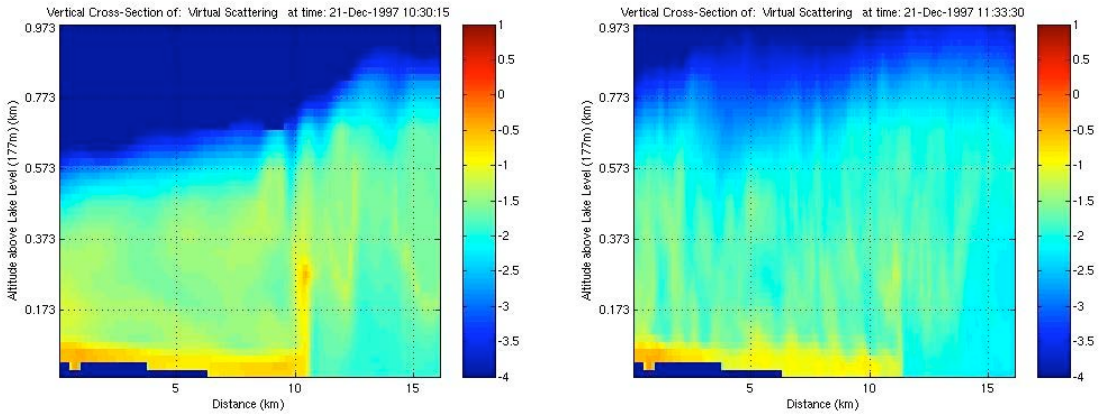

Figure 5.11: Virtual scattering output showing the structural differences in the flow between simulations created without the sixth domain (left) and including the sixth domain (right).

not these details are needed would have to be handled on a case-by-case basis. This also reveals that there is information gained in the higher resolution simulation. The question that must be addressed per case, however, is whether the information gained is needed for that situation.

5.3.2 Other Simulations

In order to compare the output from other simulations to the lidar data, some inferences have to be made about the relationship between atmospheric parameters. For example, it is reasonable to assume that a land breeze coming off of the colder land surface will have colder temperatures than the surrounding air. Therefore, looking at the temperature field from the simulation would allow us to make an estimate as to the location and extent of the land breeze. Figure 5.12 shows this information from one of the simulation's 5th grid. The land breeze can be seen extending offshore around 4-5 km. Figure 5.13 is a lidar-produced RHI volume scan for comparison of the horizontal extent with the low level CAPPI. This comparison shows reasonable agreement in the position

and extent of the land breeze when derived from the temperature data and from the lidar data.

Unfortunately, since there is no thermal observational data for the flow outside of the land breeze, there is no way to compare the exact statistics of that flow to model parameters. The validation of this region must be completed using the lidar data available. The ability to create wind vector fields from the lidar scattering data (Pirronen and Eloranta, 1995) greatly aids in analysis of the relative intensities and directions of both the land breeze and the prevailing flow. Figure 5.14 shows vector output from both the lidar data and the NMS output. Although absolute wind measurements are not available from these analyses, comparison of the two images and the relative strengths and directions of the vectors within them gives us a good means for comparison. Both of these vector fields show the land breeze being weaker in intensity than the prevailing flow, and flowing offshore from the west-northwest. One of the problems with this type of comparison is that the lidar vector field is averaged over 30 minutes, while the NMS vector field is from one individual time step. Averaging of the model data would aid in creating a more suitable comparison tool.

Notable when comparing the top and bottom halves of figure 5.15 is that the land breeze takes on a different shape in this particular simulation than in the lidar data. The top half of figure 5.15 is a virtual RHI volume scan created using the zonal velocity from 5th grid of this simulation, running at 160 m resolution. The head of the model-produced land breeze is more rounded and steeper at the front, while the lidar-observed head has a less steep nose, with a more pronounced ramp structure. The model-produced land breeze is much flatter at the upper boundary with the prevailing flow, while the lidar

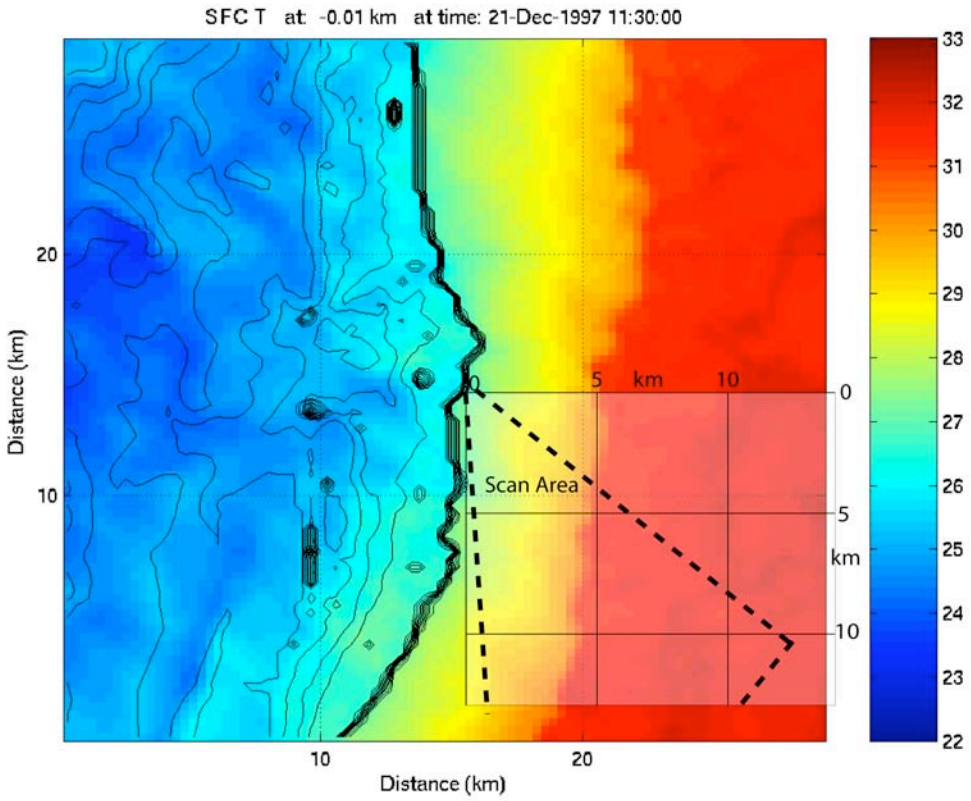

Figure 5.12: Surface air temperature data (°F) from the 5th grid of simulation 'A'. The white box indicates the approximate area of the CAPPI boxes on the image below.

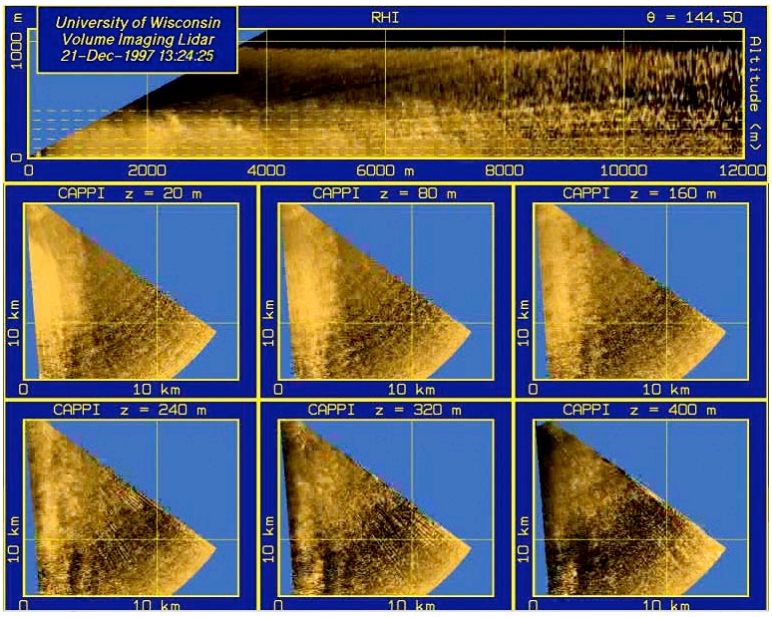

Figure 5.13: Lidar RHI volume scan of the land breeze during an early portion of the observation period (13:24:25).

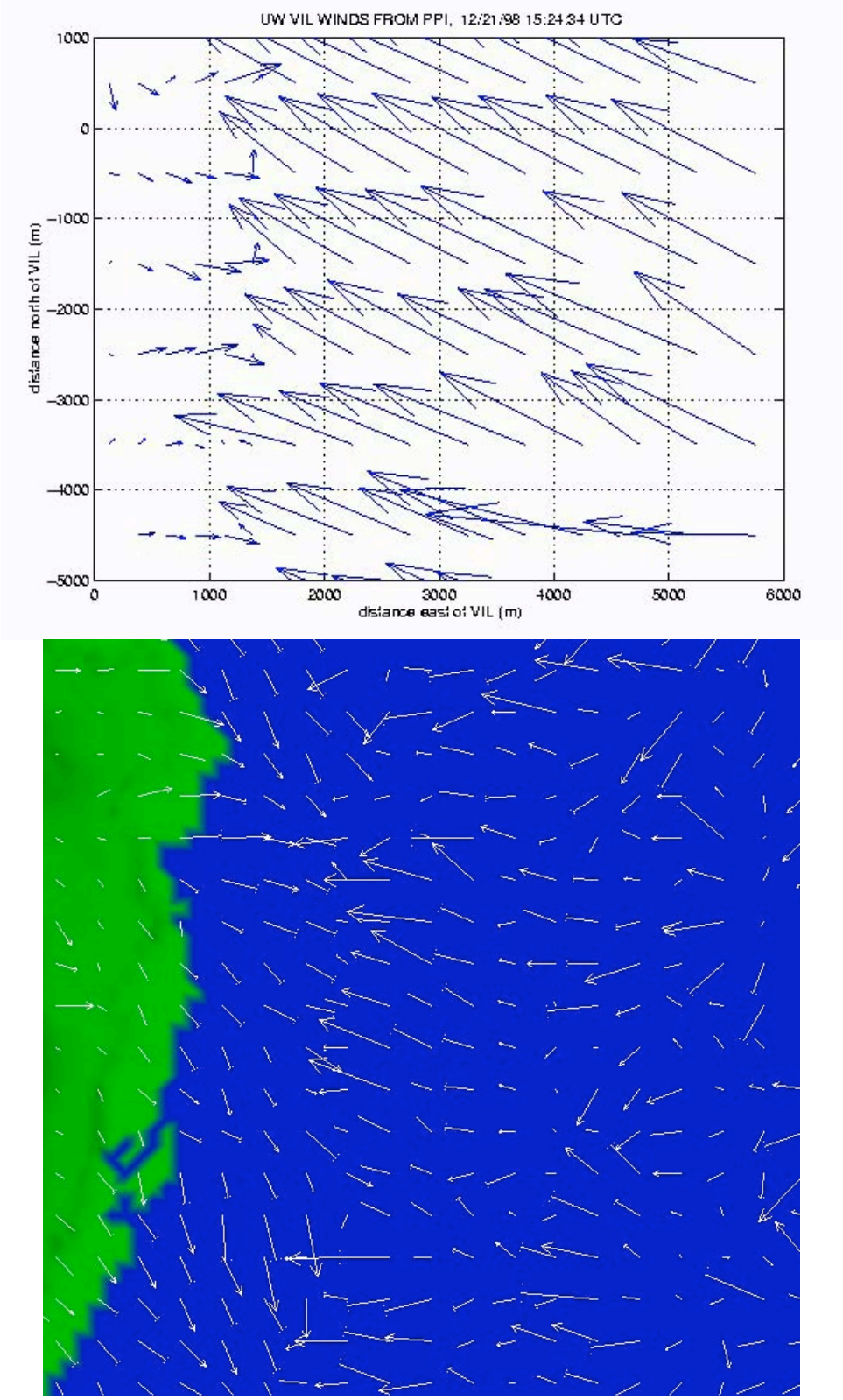

Figure 5.14: Wind vector fields from the Lidar data (top) and NMS (bottom).

observed flow has wavelike structures at the top and more closely resembles a billowing structure. This is likely due to the fact that the horizontal resolution used for the 5th grid is not sufficient to resolve the Kelvin-Helmholtz type structures forming in the wake of the head of the land breeze and creating the billowing top. At higher resolutions, these structures do show up in the model data, as was shown with the comparisons between the lidar data and simulation 'B'. Making this comparison is rather difficult because scattering is not directly proportional to wind direction, and therefore somewhat risky.

A more direct comparison can be done between the vertical velocities output by the model and the cellular structures seen in the onshore flow by the lidar. The structure of this flow is important because it potentially affects the shape and structure of the land breeze. This is especially true at the intersection between the land breeze and the onshore flow, with increased upward or downward velocities present depending on which portion of a convective cell happens to be intersecting the frontal zone. Figure 5.16 shows this comparison, with the model showing cellular structures with diameters ranging from a kilometer or so to around 5 kilometers. The lidar imagery shows cells of a similar scale, with diameters of 1-2 kilometers. The model cells are likely somewhat larger because of the limited domain size. Because of the small domain, cells that do form are likely just projected, higher resolution versions of motions taking place on the fourth grid, since they do not have sufficient room to grow and develop further within the domain.

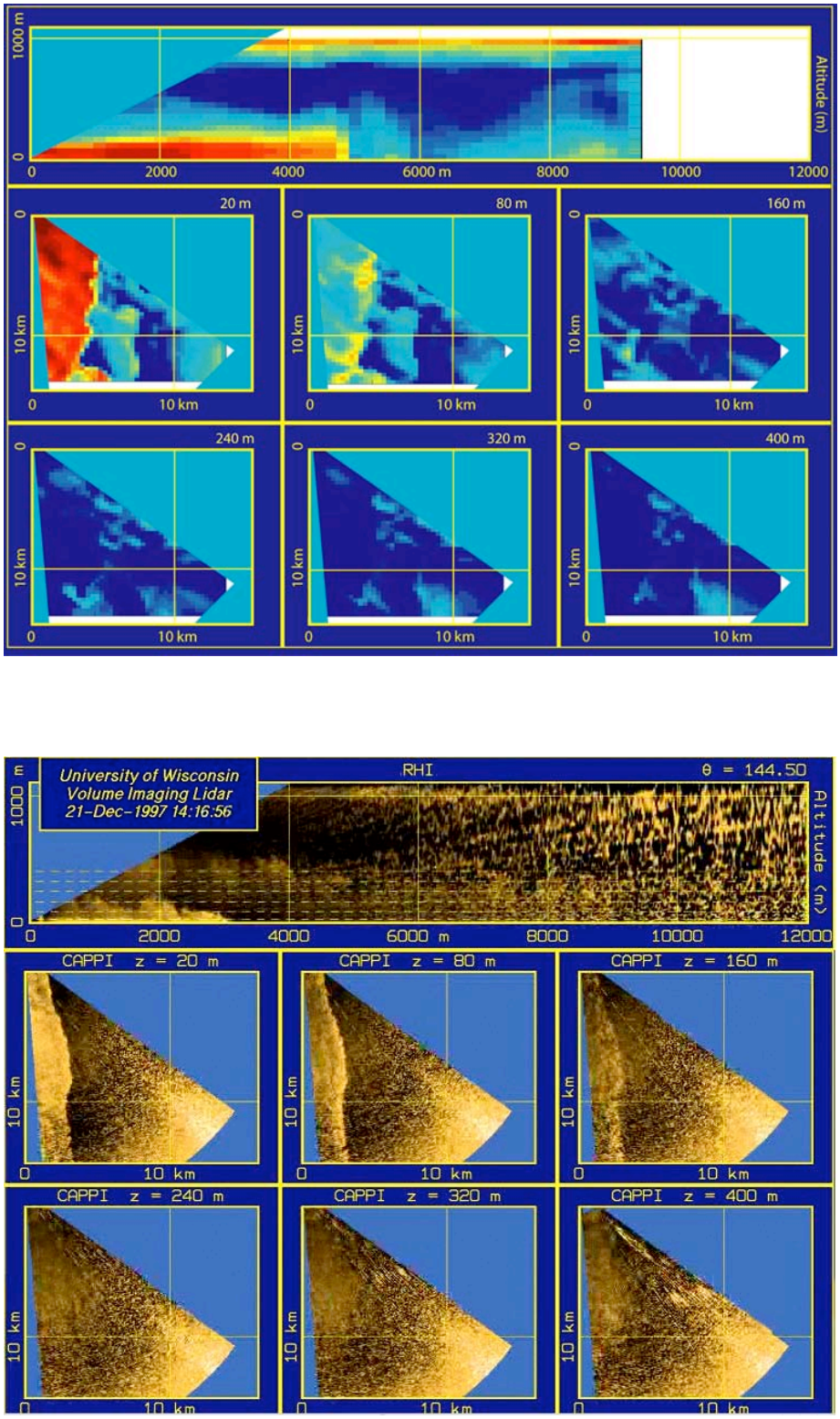

Figure 5.15: Model produced RHI volume replica, based on zonal velocity data from grid 5 of simulation 'A' (top) and an RHI volume scan from somewhat later in the observing period, showing the shallow nature of the land breeze (bottom).

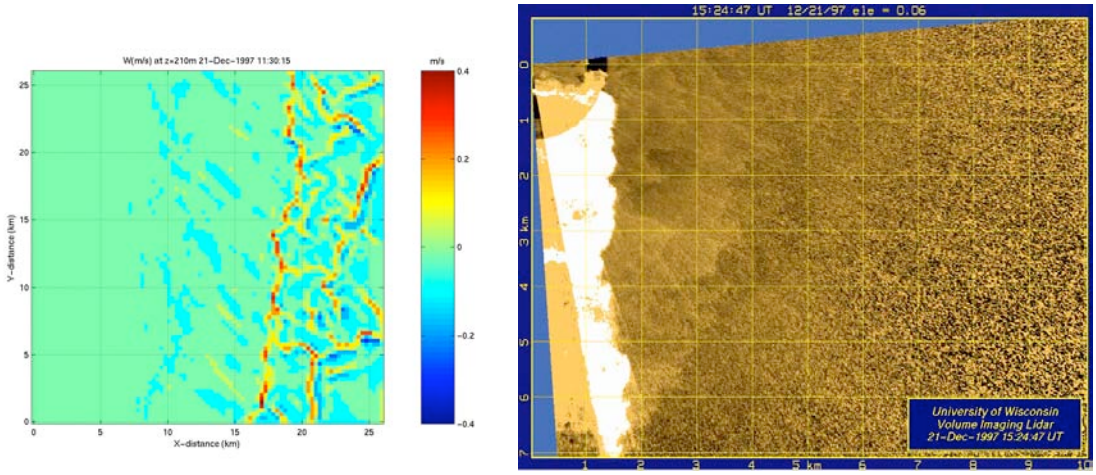

Figure 5.16: Model vertical velocity output (left) revealing cellular structure in the onshore flow, similar to that seen in the filtered PPI image at right.

Chapter 6

Conclusions

6.1 Discussion and Conclusions

The land breeze circulation simulated is a clear example of a small-scale event, affecting only the local scale, which is forced primarily from the local thermal forcing and is modulated by the large-scale synoptic situation. The position and depth of the land breeze appear to be controlled almost exclusively by the strength of the prevailing synoptic flow and the strength of the land breeze itself, a function of the land/lake temperature difference. This study reveals that the UW-NMS generally simulates the land breeze with respectable accuracy. Comparison of the simulation scattering and wind output with similar quantities derived from the VIL data reveals that the depth of the circulation is very comparable to that observed on the 21st of December. Additionally, the simulated depth of the boundary layer and land breeze head are also similar to those observed. Along with accurate simulation of several of the structural features of the land breeze itself, the NMS also simulates, with surprising precision, the timing of the primary decay of the system. This is found through comparison of the NDBC site wind direction and that measured in the simulation at the location of the NDBC site. The model does not pick up the secondary wave structures shown in observations. This was expected,

however, since these features are a result of up scale development, and are not forced from the large-scale flow.

Despite all of these similarities, the true accuracy and usefulness of the simulation can still be questioned. The simulation, at all resolving scales, had the land breeze situated too far offshore when compared to the volume imaging lidar data. It was discovered that very small errors at the synoptic scale likely lead to more significant deviations at the fine scale, resulting in the land breeze frontal position discrepancy. Given this information, we can repose the question presented originally in the introduction: Have we truly gained any information through the implementation of this dynamical downscaling technique?

An attempt was made at addressing the above question, along with others posed earlier on the issues of predictability and forecast improvement. It was shown that in this particular case, a high-resolution domain (~160 m) was needed in order to replicate many of the land breeze features. A run with identical set up to the one used for the high resolution simulation, featuring 12 km resolution did not reveal land breeze characteristics in wind speed or direction. Additionally, it was illustrated that although the 160-meter resolution revealed the land breeze, the 32-meter resolution domain more accurately portrayed the structure of the circulation as observed with the volume imaging lidar. These facts confirm that the added resolution does produce information unobtainable at coarser resolutions.

The fact that the front was displaced severely by relatively miniscule large-scale errors still leaves a challenging issue to be addressed. A potential solution to this would be to formulate an ensemble of simulations and utilize the probability density functions

of their output to come up with a predicted atmospheric state. At the resolutions utilized in this study, however, the computing power required to run an ensemble forecast would be tremendous. A better solution, utilizing current computing resources would be to run the large scale in ensemble mode in order to get as firm a grasp on the large-scale atmospheric state as possible, and then to run a deterministic, high resolution simulation which would be initialized from the ensemble mean statistics. This would reduce the computing power needed but increase the accuracy of the large-scale forecast. Additionally, an ensemble approach used at higher resolution would aid in the determination of the predictability of other microscale flows. A wide distribution of ensemble solutions would indicate that the structure or event in question is not highly predictable. A narrow distribution would indicate that implementation of the dynamic downscaling technique will likely lead to an accurate representation of the event in question.

In this study, despite the difference in horizontal extent of the land breeze, the rest of the observations and comparisons done in this study make a powerful case for the implementation of downscale simulations in the replication and prediction of local flow features. Because the land breeze, along with other small-scale phenomena such as wind storms caused by funneling of the large scale flow through topographical features or city buildings will only occur under certain synoptic conditions, inclusion of the synoptically forced flow and more importantly of its evolution is vital to accurately representing these types of structures. Therefore, single domain simulations at the high resolution will not effectively capture the evolution and decay of these flows, as they do not replicate this evolution of larger scales. Additionally, as shown in chapter 5, mesoscale simulations

not utilizing the high resolutions achieved using the nesting technique are incapable of providing sufficient detail to make high-resolution predictions about the effects of the synoptic flow at the local scale. Therefore, a simulation incorporating both ends of the spectrum replicates the flow with a significant improvement in accuracy when compared to either of the other two options.

One of the biggest challenges with utilization and justification of downscaled simulations is the validation of the flows created in these simulations. This study revealed the usefulness of volume imaging lidar data in validation of particular simulations at these high resolutions.

Imagery created utilizing the lidar data shows very clearly the structure of the land breeze, the prevailing onshore flow, as well as the front between the two airmasses. Without this imagery, it would be extremely difficult to determine the exact position of the land breeze front, as well as the depth of the land breeze over the lake. Point measurements would be able to aid in the gathering of statistics of the flow, but would not be able to illustrate the extent and general characteristics of the circulation. Similarly, in this case, the three-dimensional scanning capabilities of the lidar are very important, since even a two dimensional observation platform, such as a lidar that can only scan horizontally or vertically, or a research aircraft would not be able to resolve the undulating nature at the frontal zone between the land breeze and the synoptically forced flow. Rather, it may appear that the entire frontal zone was shifting its offshore position, rather than individual parts of the front. Similarly, the vertical structure would be difficult to guess, given only horizontal observations. It is these types of characteristics

that can easily be lost in statistical analysis if the researcher does not know that they are looking for that particular phenomenon.

As shown in chapter 5, the wind data derived using cross-correlation techniques on the lidar returns was invaluable in determining the cause of discrepancies between the simulation output and the lidar data. The NDBC site data was compared with the simulation, but that comparison led to false and conflicting assumptions about the true position of the frontal zone compared to that observed in the simulation, as the comparison between those two sources of information could have easily led to the assumption that the simulated land breeze front was closer to the shoreline than that observed, when in fact, it was actually further away. A review of the entire wind field resulted in a more fitting explanation, indicating the NDBC site was not necessarily representative of the entire domain.

Ideally, the lidar should be used in conjunction with traditional observation platforms, such as aircraft measurements or land based observation stations. This is to ensure a proper understanding of the statistics of the flow, as well as attaining a good conceptual grasp on the actual appearance, shape and nature of the circulation. Since relatively small amounts of meteorological information can actually be extracted directly from data taken by the VIL or similar systems, there must be alternative means in place for the gathering these statistics. In this study, these means were not available, and this limited the amount of comparison that was possible between the simulations and observations from the Lake-ICE experiment.

To summarize, the main conclusions are:

- Dynamic downscaling provides useful information when applied properly in specific situations. Typically, these are situations in which the features replicated are the result of the interaction between predictable large-scale (meso-α and larger) flows and well represented local forcing.
- In order to accurately reproduce the statistics and timing of the microscale phenomena a combination of the large scale and small scale evolution must be utilized.
- VIL observations provide a useful and effective tool in the validation of simulations of localized phenomena.

6.2 Recommendations For Future Work

Technological advances will continue to allow for larger simulations as well as an increase in the amount of data able to be gathered from lidar systems. Very clearly, more work needs to be completed in both fields, and preferably by one group understanding important aspects of both atmospheric simulation and lidar, in order to more efficiently link numerical simulation of small-scale phenomena and lidar validation.

This study showed that there is merit in attempting to simulate small-scale atmospheric phenomena utilizing the downscaling technique. Further study must be completed to determine how this technique compares with more traditional LES studies.

Work should be completed to check the nature of turbulent structures in the nested domains. Although the goal of these simulations is not to replicate the turbulence statistics, these structures can be vital to accurate recreation of the studied phenomenon. In this study the size of the high-resolution domains is simply increased in order to give a

buffer zone on either side of the area of interest to allow turbulent structures to mature at the resolution of that domain. The first problem with this approach is, of course, that this becomes very expensive computationally. The second issue is that the amount of buffer zone needed depends on what is being simulated. Because the next larger domain is resolving structures at a resolution that is at the most five times (in these simulations) greater than the high-resolution domain, the inflow is not completely laminar in nature. This means that although the turbulence is not mature for the resolution of the inner domain, it is present. Because of this fact, mature turbulence would form more rapidly than it would if the inflow were completely laminar. In his studies of convective boundary layers, Mayor (2001) showed that mature turbulent structures formed at comparable wind speeds and resolution at around 8 km into the domain from a laminar inflow condition. Another potential solution to improving the turbulence inside the nested domains could be nesting an LES code inside of a mesoscale simulation. This would allow evolution of the large scale, while improving the ability to accurately represent boundary layer structure.

The miscalculated frontal position of this work showed that slight differences in the synoptically forced flow can lead to discrepancies at the microscale. As discussed previously, a possible solution to this potential issue would be the use of ensemble forecasts at the small scale. Further development of ensemble techniques would aid in the improvements of high-resolution forecasts. Additionally, the continued development of full ensemble simulation systems would be of great benefit to this work as well as the entire atmospheric simulation community.

In order to assure that this is a viable technique in terms of accurately simulating small scale phenomena that are forced from larger scales, simulations of different events would need to be performed to test the simulation's performance in several different cases.

In terms of lidar technology, an eye-safe, fast-scanning system would be extremely helpful in the validation of these types of simulation studies, since boundary layer structure over a land surface, including in urban environments, could be obtained. This aspect is critically absent in the Lake-ICE dataset, leaving little knowledge as to the turbulent structure upwind from the lidar site. The fast scanning speed would help in gathering more accurate measurements of the aerosol structure and motion, and would allow for an increased temporal resolution.

Finally, several improvements can be made in the techniques utilized for inter-comparison between the model results and the lidar data. The virtual scattering parameter is a very crude technique used to gain some understanding of relative aerosol concentration over the area of interest. Inclusion of more complicated matters such as aerosol sources over the land surface, or the utilization of a dataset describing the nature of aerosol concentrations in Wisconsin, as opposed to those found in Washington D.C. would likely increase the accuracy of the virtual scattering. Additionally, perhaps more model-simulated parameters could be obtained from the lidar data, aiding further in the validation of the simulation output.

Appendix

A Adjustments to the UW-NMS

The University of Wisconsin Non-Hydrostatic Modeling System (UW-NMS) was utilized for the simulations in this work. Throughout the process of running these simulations, some shortcomings were found in the code, and corrections were made in order to better simulate the atmospheric flow at the scales covered.

1 Momentum Balance Adjustment

Preliminary simulations at high resolution contained streak-like features, initializing from an anomaly on the high resolution, sixth grid upwind boundary and then advecting through the domain with the mean flow. Figure A.1 shows an example of this phenomenon. The perturbations in the flow fields influenced the advection of atmospheric properties such as temperature and relative humidity. This resulted in unrealistic structures developing inside the high-resolution domain. After some investigation, it was determined that momentum fluxes between nested grids were not being handled correctly. An explanation of why this was occurring follows.

The UW-NMS utilizes variably stepped topography, meaning that grid boxes, if at the surface of the earth, can have a smaller vertical scale than the grid box next to it. The center of that grid is adjusted accordingly, and is placed half way between the elevation of the surface and the top of the grid box. Unlike terrain following coordinate systems, stepped topography can resolve very steep slopes. The problem with traditional, non-variable, stepped topography however, is that very gradual slopes are not resolved, and

gradual changes in elevation are misrepresented as flat. Using the variably stepped approach allows both steep and gradual changes in elevation to be resolved by the model.

Using the variably stepped topography does cause a problem, however. That is that when nesting, the area of the vertical face between one large grid box and the next, which contains a nested, higher resolution grid, may not be equal (figure A.2). This is due to the fact that the elevation of the topography for a grid box is defined in the center of the cell. Therefore, although the areas of the coarse interpolation of the fine mesh and the coarse grid cell next to it may line up, the sum of the areas of the nested fine mesh boxes along the boundary and that of the coarse grid cell next to it do not have to line up at all. Since the momentum being transferred between one grid box and the next is the product of the density, velocity and the area through which the transfer occurs, changing this area can have a great effect on scaling of the velocity across that boundary. A sharp decrease in the vertical area would result in an increase in horizontal velocity to keep a momentum balance between the two grid boxes. This is the cause of the streaks shown in figure A.1 and outlined above.

In order to solve this problem, a post calculation redistribution of momentum is required, with adjustments made to the wind speeds in order to maintain continuity between the grid cells, and to eliminate these streaky features. The amount of momentum flux from each grid is calculated for individual coarse grid boxes. Then, the corresponding sum of fine grid box momentums is calculated and compared to the value from the coarse grid. Since original interpolation is done from the coarser to the finer domain, the coarse domain is taken to be truth. Also, since this is solely a boundary problem at the earth surface, this correction is only done at domain boundaries for the lowest three grid points.

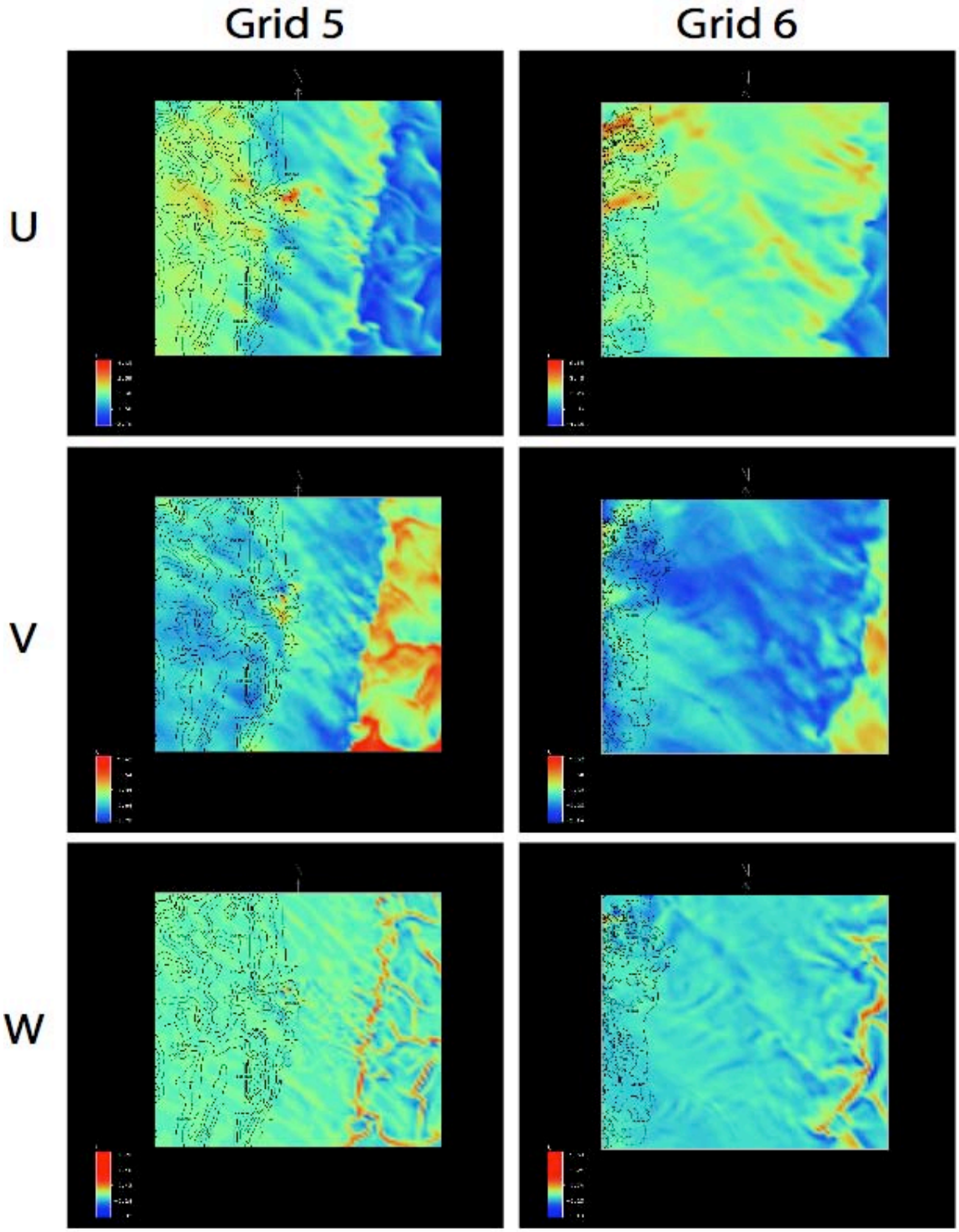

Figure A.1: Output from preliminary simulations showing the perturbations in the wind fields caused by improper handling of the momentum balance at nested grid boundaries. Note the perturbations at the left boundary in the 6th grid (right column), and in the middle of the fifth domain (left column), at the location of the sixth grid.

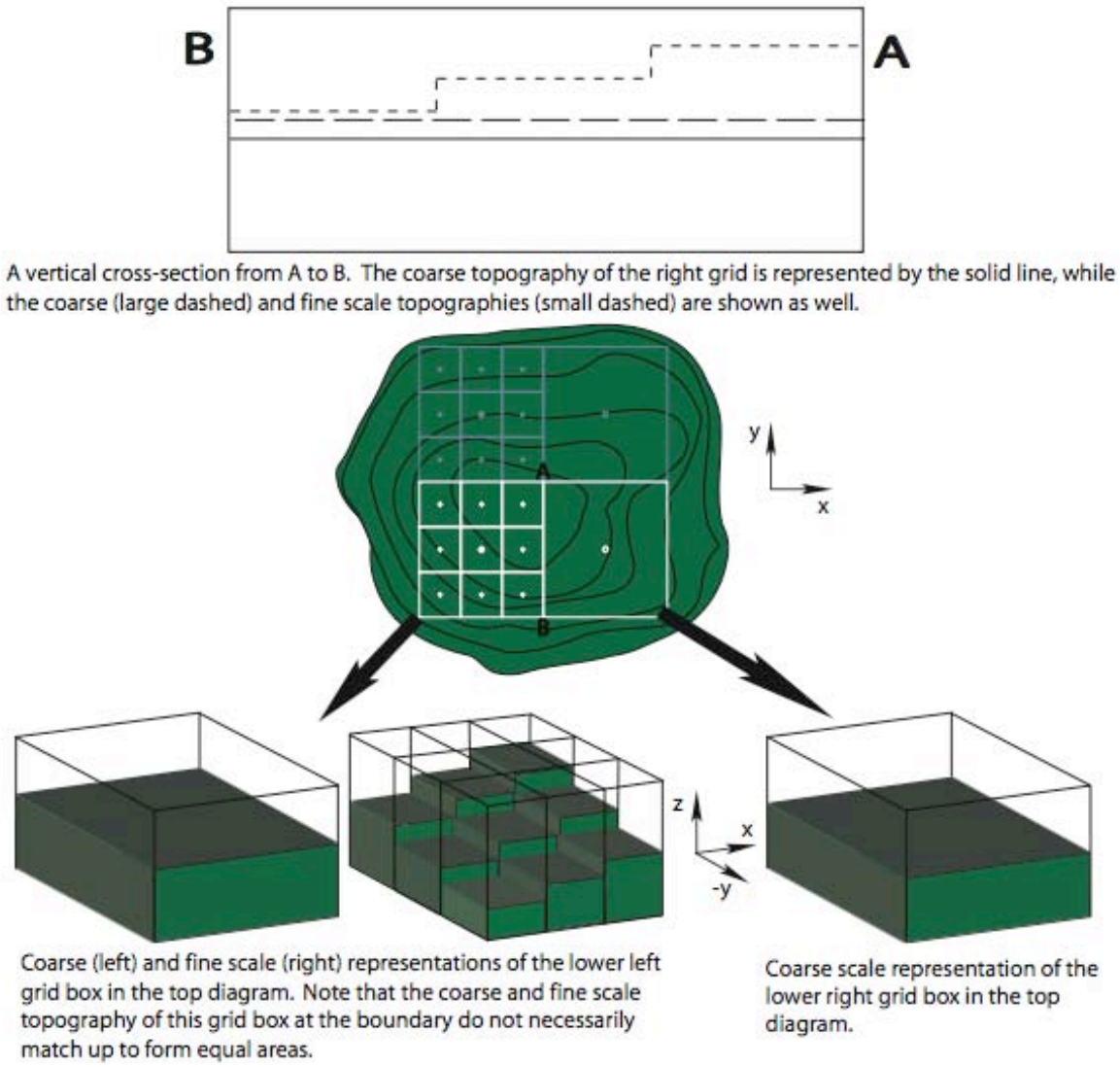

Figure A.2: A rendering of the boundary between two fictitious grid boxes. Note that the boundary between the boxes can be represented in three different ways, depending on which grid box and which resolution is used. These different representations result in different vertical areas at that boundary.

If the momentum leaving one grid is not being transferred fully into the next grid, an adjustment is made to the velocities in order to balance out the transfer. For example, if there is more momentum flowing out of the large grid box than flowing into the small one, the average of the small grid box velocities is increased in order to increase the momentum flux into those cells. This adjustment is somewhat tricky for several reasons.

First, the fact that the topography is variably stepped once again comes into play, as each of the fine grid boxes must be given a weighting factor for the redistribution, since some may be one half meter thick while others are 19 meters thick. Attempting to adjust the velocity of the grid boxes equally would result in large amounts of fluid being forced through not very much area. Since this is not desirable, the weighting factors were introduced. Additionally, there are numerical stability issues to consider when adjusting velocity parameters. To make sure not to disturb the flow too much, a strong effort is made to not reverse the flow at any time. Also, in the case where there are both positive and negative fine scale velocities in the same coarse grid box, an attempt is made to decrease the magnitude of velocities before increasing any. Once all velocities that can be decreased are set to zero, if there is still a discrepancy, increases are made in order to avoid changing the direction of the flow. A chart of the redistribution process for one of the boundaries is shown in figure A.3.

Figures A.4 and A.5 show the results of this redistribution. Very clearly, the anomalies that had formed along the boundary are now removed. This makes for a much more continuous transition from the larger domain to the high resolution one.

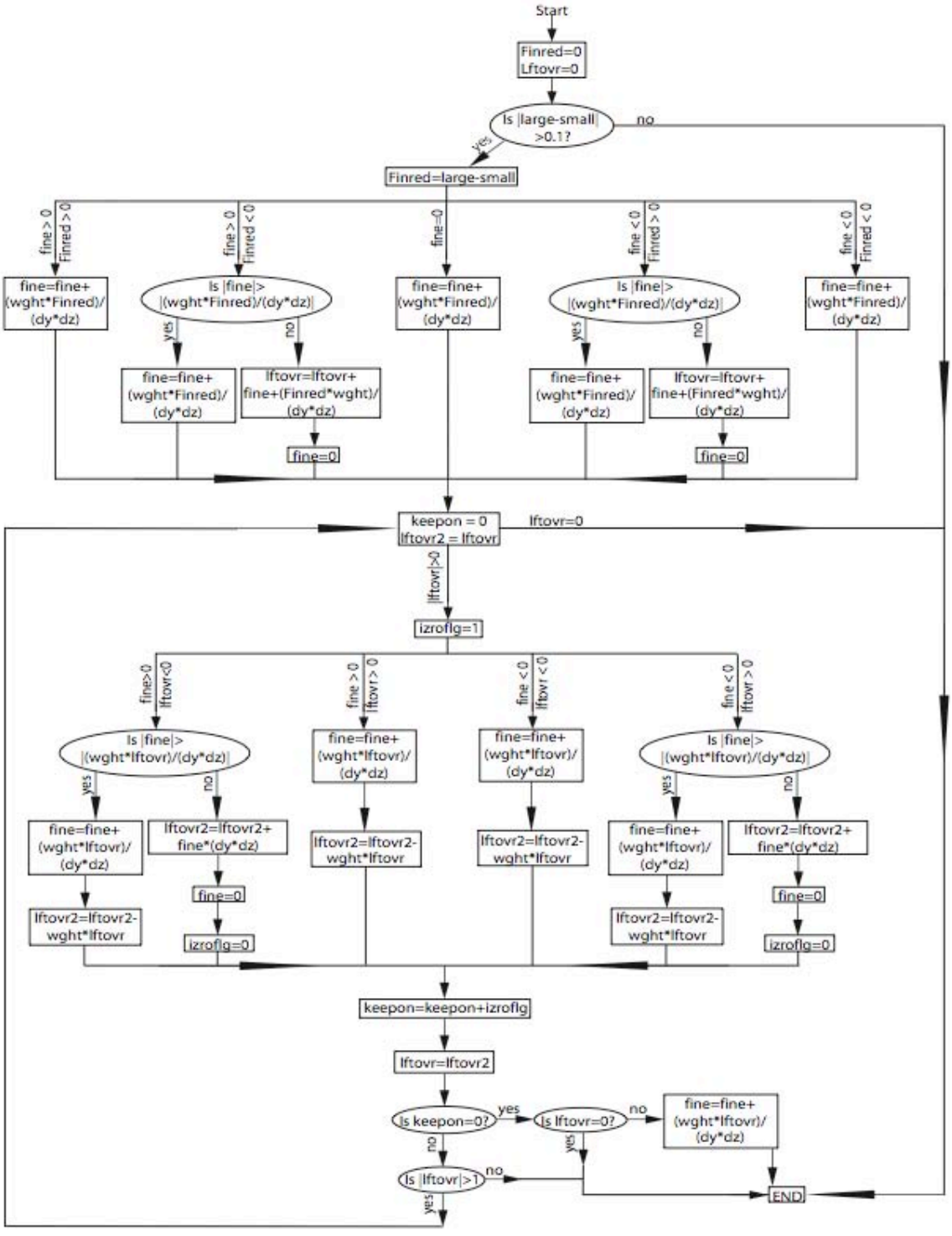

Figure A.3: A flow chart of the redistribution process along one of the boundaries. This is repeated for every grid point along the boundary, and then repeated along all four domain boundaries.

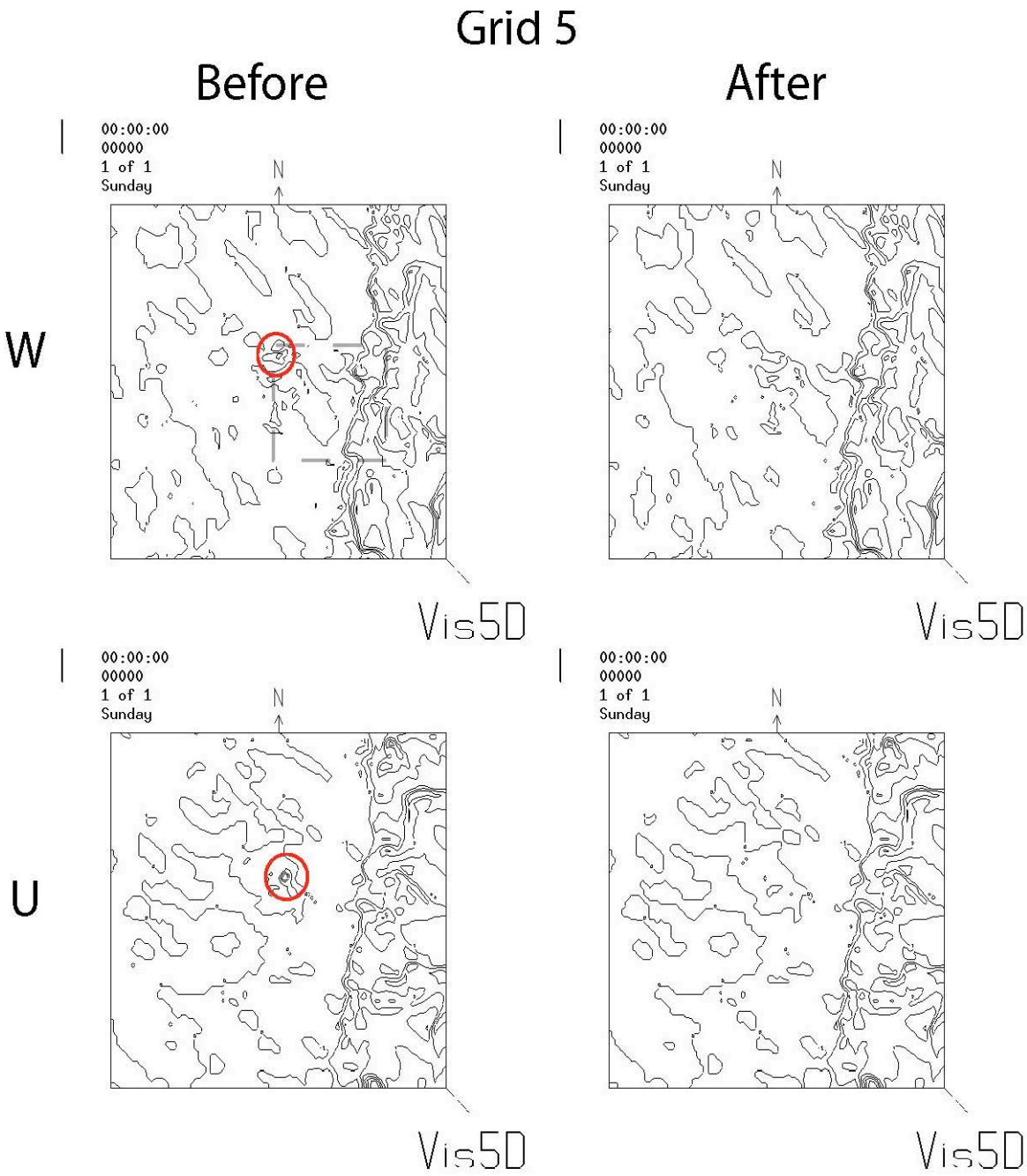

Figure A.4: Contour plots of the vertical and U component velocities for the fifth grid. The outline of the sixth grid is shown in the upper left plot, and trouble areas are circled in red. Note that in the right column of simulation results after the adjustment is implemented the anomalies are no longer present, while the flow maintains the same general structure.

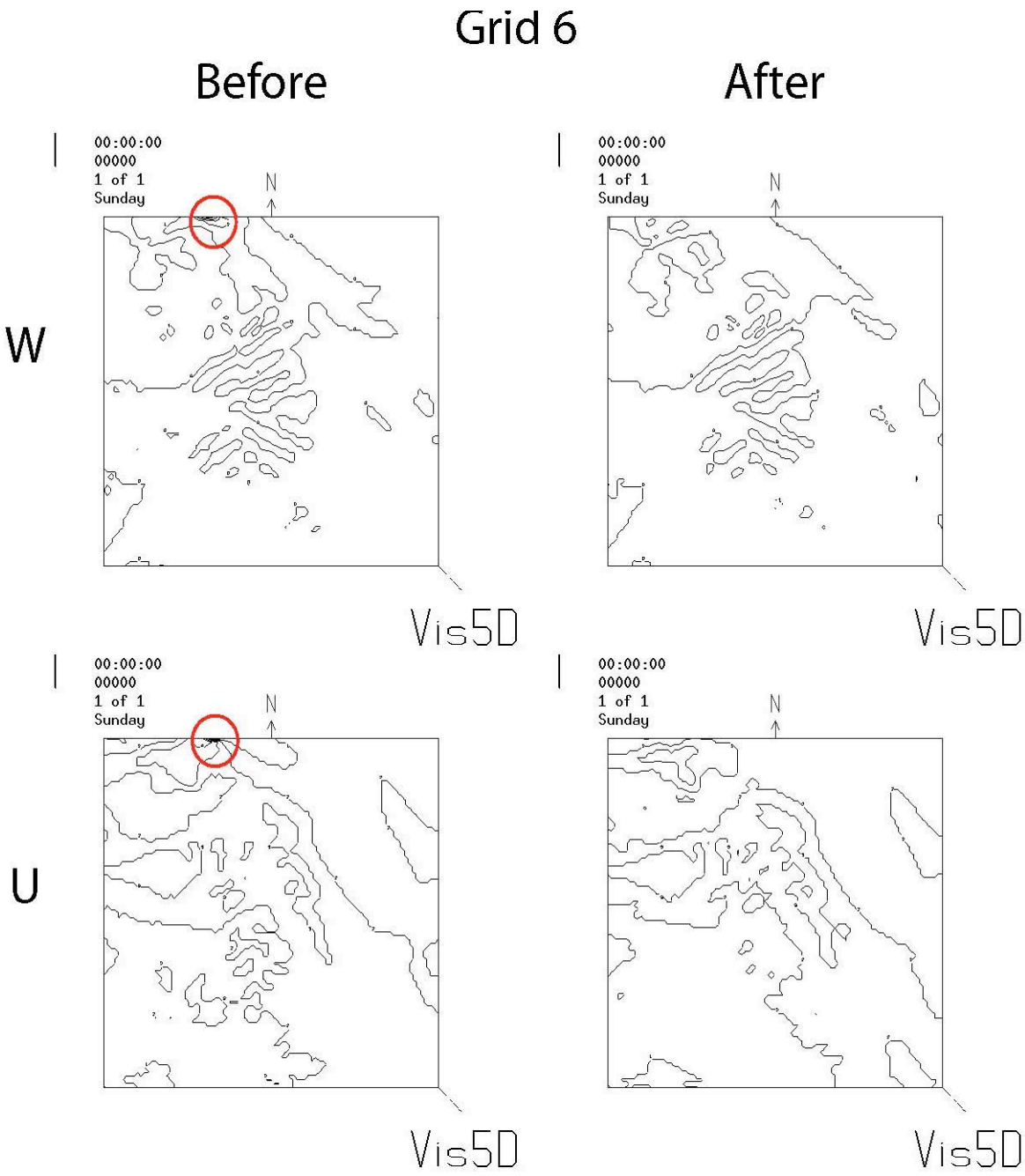

Figure A.5: Same as Figure A.4 except for the inner domain. Again, trouble areas have been circled in red. Also, again the flow maintains similar features before and after the removal of the anomaly.

References

Agee, E., M.L. Hart, 1990: Boundary Layer and Mesoscale Structure over Lake Michigan during a Wintertime Cold Air Outbreak. *Journal of the Atmospheric Sciences,* **47,** 2293-2316.

-----, A. Gluhovsky, 1999: LES Model Sensitivities to Domains, Grids, and Large-Eddy Timescales. *Journal of the Atmospheric Sciences*, **56,** 599-604.

-----, A. Gluhovsky, 1999: Further Aspects of Large Eddy Simulation Model Statistics and Inconsistencies with Field Data. *Journal of the Atmospheric Sciences*, **56,** 2948-2950.

Alpert, P., J. Neumann, 1983: A Simulation of Lake Michigan's Winter Land Breeze on 7 November 1978. *Monthly Weather Review*, **111,** 1873-1881.

Ballentine, R.J., 1982: Numerical Simulation of Land-Breeze-Induced Snowbands Along the Western Shore of Lake Michigan. *Monthly Weather Review*., **110,** 1544-1553.

-----, 1980: A Numerical Investigation of New England Coastal Frontogenesis. *Monthly Weather Review,* **108,** 1479-1497.

Clappier, A., A, Martilli, et al., 2000: Effect of Sea Breeze on Air Pollution in the Greater Athens Area. Part I: Numerical Simulations and Field Observations. *Journal of Applied Meteorology*, **39,** 546-562.

Clark, T.L., R.D. Farley, 1984: Severe Downslope Windstorm Calculations in Two and Three Spatial Dimensions Using Anelastic Interactive Grid Nesting: A Possible Mechanism for Gustiness. *Journal of the Atmospheric Sciences*, **41,** 329-350.

Covert, D.S., R.J. Charlson, N.C. Ahlquist, 1972: A Study of the Relationship of Chemical Composition and Humidity to Light Scattered by Aerosols. *Journal of Applied Meteorology*, **11,** 968-976.

Day, D.E., W.C. Malm, 2001: Aerosol Light Scattering Measurements as a Function of Relative Humidity: A Comparison Between Measurements Made at Three Different Sites. *Atmospheric Environment,* **35,** 5169-5176.

Darby, L.S., R.M. Banta, R.A. Pielke, 2002: Comparisons Between Mesoscale Model Terrain Sensitivity Studies and Doppler Lidar Measurements in the Sea Breeze at Monterey Bay. *Monthly Weather Review,* **130,** 2813-2838.

Duclaux, O., et al., 2002: 3D-air Quality Model Evaluation Using the Lidar Technique. *Atmospheric Environment,* **36,** 5081-5095.

Eloranta, E.W., R. E. Kuehn, S. D. Mayor and P. Ponsardin, 1999: Near-shore, Boundary Layer Structure Over Lake Michigan in Winter, American Meteorological Society 13th Symposium on Boundary Layers and Turbulence, Dallas, TX, Jan. 1-15.

Elsner, J.B., J.R. Mecilkalski, A.A. Tsonis, 1989: A Shore-Parallel Cloud Band over Lake Michigan. *Monthly Weather Review,* **117,** 2822-2823.

Estoque, M.A., 1962: The Sea Breeze as a Function of the Prevailing Synoptic Situation. *Journal of the Atmospheric Sciences*, **19,** 244–250.

Fast, J.D., L.S. Darby, 2004: An Evaluation of Mesoscale Model Predictions of Down-Valley and Canyon Flows and Their Consequences Using Doppler Lidar Measurements During VTMX 2000. *Journal of Applied Meteorology,* **43,** 420-436.

Fitzgerald, J.W., W.A. Hoppel, 1982: The Size and Scattering Coefficient of Urban Aerosol Particles at Washington, DC as a Function of Relative Humidity. *Journal of the Atmospheric Sciences,* **39,** 1838-1852.

Grund, C.J., E.W. Eloranta, 1991: The University of Wisconsin High Spectral Resolution Lidar. *Optical Engineering*, **30**, 6-12.

Haurwitz, B., 1941: *Dynamic Meteorology*. McGraw-Hill, 139-140.

-----, 1947: Comments on the Sea-Breeze Circulation. *Journal of Meteorology*, **4,** 1-8.

Hjelmfelt, M.R., 1990: Numerical Study of the Influence of Environmental Conditions on Lake-Effect Snowstorms over Lake Michigan. *Monthly Weather Review,* **118,** 138-149.

-----, 1992: Orographic Effects in Simulated Lake-Effect Snowstorms over Lake Michigan. *Monthly Weather Review,* **120,** 373-377.

Jeffreys, H., 1922: On the Dynamics of Wind. *Quarterly Journal of the Royal Meteorological Society,* **48,** 29-46.

Keen, C.S., W.A. Lyons, J.A. Schuh, 1979: Air Pollution Transport Studies in a Coastal Zone Using Kinematic Diagnostic Analysis. *Journal of Applied Meteorology,* **18,** 606-615.

Kolev, I., O. Parvanov, B. Kaprielov, E. Donev, D. Ivanov, 1998: Lidar Observations of Sea-Breeze and Land-Breeze Aerosol Structure on the Black Sea. *Journal of Applied Meteorology,* **37,** 982-995.

Kovalev, V. A., W. E. Eichinger. Elastic Lidar: Theory, Practice, and Analysis Methods. Hoboken: Wiley and Sons, 2004.

Kristovich, et al., 2000: The Lake-Induced Convection Experiment and the Snowband Dynamics Project. *Bulletin of the American Meteorological Society*, **81,** 519-542.

Mayor, S.D., 2001: Volume Imaging Lidar Observations and Large-Eddy Simulations of Convective Internal Boundary Layers, PhD Thesis, The University of Wisconsin – Madison.

Mayor, S. D., G.J. Tripoli, E.W. Eloranta, 2003: Evaluating Large-Eddy Simulations Using Volume Imaging Lidar Data. *Monthly Weather Review,* **131,** 1428-1452.

Mitsumoto, S., H. Ueda, H. Ozoe, 1983: A Laboratory Experiment on the Dynamics of the Land and Sea Breeze. *Journal of the Atmospheric Sciences*, **40,** 1228-1240.

Moeng, C., Sullivan, P.P., 1994: A Comparison of Shear- and Buoyancy-Driven Planetary Boundary Layer Flows. *Journal of the Atmospheric Sciences*, **51,** 999-1022.

Nakane, H., Y. Sasano, 1986: Structure of a Sea Breeze Front Revealed by Scanning Lidar Observations. *Journal of the Meteorological Society of Japan*, **64,** 787-792.

Neumann, J., Y. Mahrer, 1971: A Theoretical Study of the Land and Sea Breeze Circulation. *Journal of the Atmospheric Sciences*, **28,** 532-542.

Ohara, T., I. Uno, S. Wakamatsu, 1989: Observed Structure of a Land Breeze Head in the Tokyo Metropolitan Area. *Journal of Applied Meteorology*, **28,** 693-704.

Passarelli, R.E., R.R. Braham, 1981: The Role of the Winter Land Breeze in the Formation of Great Lake Snow Storms. *Bulletin of the American Meteorological Society,* **62,** 482-491.

Petterssen, S., Calabrese, P. A., 1959: On Some Weather Influences Due to Warming of the Air By the Great Lakes. *Journal of the Atmospheric Sciences*, **16**, 646–652.

Phillips, N.A., J. Shukla, 1973: On the Strategy of Combining Coarse and Fine Meshes in Numerical Weather Prediction. *Journal of Applied Meteorology*, **12,** 763-770.

Piironen, A. and E. W. Eloranta, 1995: An Accuracy Analysis of the Wind Profiles Calculated from Volume Imaging Lidar Data. *Journal of Geophysical Research*, **100**, 25559-25567.

Sasano, Y., H. Hirohara, T. Yamasaki, H. Shimizu, N. Takeuchi, T. Kawamura, 1982: Horizontal Wind Vector Determination from the Displacement of Aerosol Distribution Patterns Observed by a Scanning Lidar. *Journal of Applied Meteorology,* **21,** 1516-1523.

Schmidt, F.H., 1947: An Elementary Theory of the Land- and Sea-Breeze Circulation. *Journal of Meteorology,* **4,** 9-15.

Schoenberger, L.M., 1986: Mesoscale Features of the Michigan Land Breeze Using PAM II Temperature Data. *Weather and Forecasting,* **1,** 127-135.

Schols, J., E.W. Eloranta, 1992: The Calculation of Area-Averaged Vertical Profiles of the Horizontal Wind Velocity Using Volume Imaging Lidar Data. *Journal of Geophysical Research,* **97,** 18395-18408.

Sha, W., T. Kawamura, H. Ueda, 1991: A Numerical Study on Sea/Land Breezes as a Gravity Current: Kelvin-Helmholtz Billows and Inland Penetration of the Sea-Breeze Front. *Journal of the Atmospheric Sciences*, **48,** 1649-1665.

Shafran, P.C., N.L. Seaman, G.A. Ganyo, 2000: Evaluation of Numerical Predictions of Boundary Layer Structure During the Lake Michigan Ozone Study. *Journal of Applied Meteorology,* **39,** 412-426.

Tripoli, G.J., 1992: A Nonhydrostatic Mesoscale Model Designed to Simulate Scale Interaction. *Monthly Weather Review*, **120,** 1342-1359.

Winstead, N.S., P.D. Mourad, 2000: Shallow Great Lake-Scale Atmospheric Thermal Circulation Imaged by Synthetic Aperture Radar. *Monthly Weather Review,* **128,** 3654-3663.

Wyngaard, J.C., L.J. Peltier, S. Khanna, 1998: LES in the Surface Layer: Surface Fluxes, Scaling, and SGS Modeling. *Journal of the Atmospheric Sciences*, **55,** 1733-1754.

Zhong, S., E.S. Takle, 1993: The Effects of Large-Scale Winds on the Sea-Land-Breeze Circulations in an Area of Complex Coastal Heating. *Journal of Applied Meteorology,* **32,** 1181-1195.